H_2 Solar: Photoelectrochemical cells for water splitting

Afonso Oliveira
Mestrado em Engenharia Física
Departamento de Física e Astronomia
2021

Orientador
Dr. Arlete Apolinário, Universidade do Porto

Coorientador
Dr. Célia Sousa, Universidade do Porto

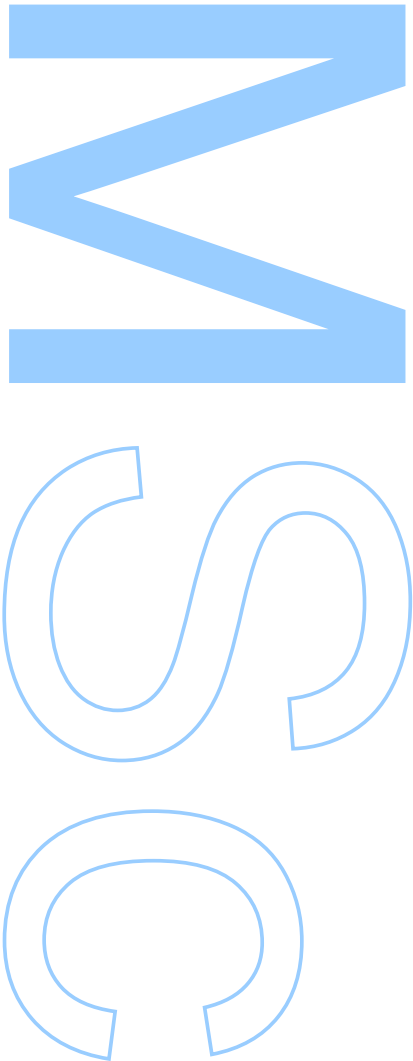
U.PORTO

FACULDADE DE CIÊNCIAS
UNIVERSIDADE DO PORTO

Todas as correções determinadas pelo júri, e só essas, foram efetuadas.

O Presidente do Júri,

Porto, _____/_____/_____



UNIVERSIDADE DO PORTO

MASTERS THESIS

H_2 Solar: Photoelectrochemical cells for water splitting

Author:
Afonso OLIVEIRA

Supervisor:
Arlete APOLINÁRIO

A thesis submitted in fulfilment of the requirements
for the degree of MSc. Engineering Physics

at the

Faculdade de Ciências da Universidade do Porto
Departamento de Física e Astronomia

December 26, 2021

" If I have seen further it is by standing on the shoulders of Giants. "

Isaac Newton

Acknowledgements

Queria expressar a minha gratidão a toda a gente que me apoiou ao longo do meu percurso académico que culminou com a elaboração desta tese.

Quero agradecer às minhas orientadoras, Arlete Apolinário e Célia Sousa por todo auxílio prestado perante as dificuldades que se foram apresentado ao longo do percurso. Agradeço também o apoio e a visão crítica que tiveram sobre este trabalho, tendo sido uma peça fundamental para a dissertação assim como para o meu crescimento pessoal e profissional.

A toda a equipa do IFIMUP pela assistência na prática laboratorial, discussões sobre os fenómenos físicos observados e auxílio na minha aprendizagem das técnicas avançadas de medição que foram extensivamente usadas ao longo de toda esta dissertação. Quero dar um especial agradecimento à Paula Quitério por toda a sua disponibilidade, pela sua ajuda incansável até ao último minuto e pelas palavras de motivação nos momentos mais necessários.

Aos amigos que fiz no meu percurso universitário, aos que acabaram o curso comigo, aos que optaram por um caminho diferente e aos que se mantêm na luta sem desistir. Aos meus amigos de infância, adolescência, aos amigos que a Ruca me deu a oportunidade de conhecer e a todos os que conheci nas mais diversas situações ao longo desta caminhada.

À Juliana Amorim por toda a ajuda e apoio que me deu ao longo deste caminho.

Àqueles que defenderam também as suas dissertações este ano e sofreram essa ânsia comigo.

Aos meus pais, irmã e a toda a minha família que sempre me apoiaram em todos os momentos, mesmo naqueles em que não estavam fisicamente presentes.

Um obrigado a todos porque sem todo o apoio que me deram, não era possível estar aqui a escrever-vos nos agradecimentos desta dissertação.

Obrigado!!!

UNIVERSIDADE DO PORTO

Abstract

Faculdade de Ciências da Universidade do Porto
Departamento de Física e Astronomia

MSc. Engineering Physics

H_2 Solar: Photoelectrochemical cells for water splitting

by Afonso OLIVEIRA

The energy consumption of the global society has been sharply rising over the years. To sustain energetic needs and simultaneously combat the harmful use of pollutants, it is necessary resorting to efficient and green energy sources. The use of photoelectrochemical (PEC) cells is a viable alternative to convert solar energy into green hydrogen.

Hematite is one of the most promising semiconductor for PEC applications due to the abundance, low-cost, non-toxicity and suitable bandgap (1.9-2.1 eV), allowing a theoretical solar-to-hydrogen efficiency of 16%. However it presents some limiting drawbacks such as low electron mobility, short hole diffusion and incompatible flat band potential for spontaneous water splitting.

Aiming low-cost fabrication methods to obtain efficient and stable photoanodes, this work consists in the optimization and innovation of hematite based nanomaterials, by combining two semiconductors oxides, hematite ($\alpha - Fe_2O_3$) and titanium dioxide (TiO_2).

Through the fabrication of 2D planar thin films based on heterojunctions of double-layered hematite and TiO_2 n-type semiconductors, it was studied and optimized features like the double-layers configuration, their thicknesses and annealing conditions. Films of Fe/Ti (and Ti/Fe) were deposited by Ion Beam Deposition, with thicknesses of Fe equal to 60, 150 nm and 5 or 50 nm of Ti, in order to explore the most appropriated configuration and thickness range to improve the photoanodes photoresponse.

It was obtained a maximum photocurrent density output of $\approx 0.7\ mA/cm^2$ for photoanodes with a thinner TiO_2 layer deposited on the hematite surface. The improvement of these photoanodes performance were achieved by decreasing the e-h recombination

rates due to the smaller photoanode thickness and by increasing the photoanode absorption due to the presence of a TiO_2 layer. The photoanode bulk properties were also enhanced by promoting the diffusion of Sn (doping) from the substrate into the hematite lattice, by using a two-step annealing approach at high temperatures (800 ºC).

Additionally, to keep increasing the efficiency of these photoanodes, the Fe/Ti thin films were nanostructured using electrochemical anodization. The obtained nanoporous anodic oxides allows primarily the decrease of the structure size, increasing the active surface area, and shorten the path for photogenerated holes and electrons to reach the electrolyte interface, and electric-opposite contact, respectively lowering their recombination. In this work, it was obtained a photoresponse improvement in order of 200% when comparing with the planar photoanode configuration.

The influence of co-catalysts on the photoanode performance were also tested by electrodepositing FeCo on the surface of the photoanode. The co-catalyst FeCo oxide showed a significant improvement in the photocurrent of more than 60% as well as a decreasing of the onset voltages potentiating thus the water splitting reactions.

The photoanodes were characterized through scanning electron microscopy, energy dispersive X-ray spectroscopy, X-ray diffraction, UV-Vis and photocurrent density vs voltage curves, allowing to understand the impact of the morphological, structural, optical and photoelectrochemical properties in the photoanodes performance.

UNIVERSIDADE DO PORTO

Resumo

Faculdade de Ciências da Universidade do Porto
Departamento de Física e Astronomia

Mestrado Integrado em Engenharia Física

H_2 Solar: Photoelectrochemical cells for water splitting

por Afonso OLIVEIRA

O consumo de energia da sociedade global tem vindo a aumentar acentuadamente ao longo dos anos. Para sustentar as necessidades energéticas e simultaneamente, combater o uso nocivo de poluentes, é necessário recorrer a fontes de energia eficientes e ecológicas. O uso de células fotoeletroquímicas (PEC) é uma alternativa viável para conversão de energia solar em hidrogénio verde.

A hematite é um dos semicondutores mais promissores para aplicações PEC devido à sua abundância, baixo custo, não toxicidade, band-gap adequado (1.9-2.1 eV) e a uma eficiência solar-hidrogénio teórica de 16%, no entanto, apresenta algumas limitações, tais como uma baixa mobilidade eletrónica, baixa difusão lacunar e bordas de potencial das bandas de valencia e condução incompatíveis para a divisão espontânea da molécula de água.

Visando métodos de fabricação de baixo custo para obtenção de fotoânodos eficientes e estáveis, este trabalho consiste na otimização e inovação de nanomateriais à base de hematite, combinando dois óxidos semicondutores, hematite ($\alpha - Fe_2O_3$) e dióxido de titânio (TiO_2).

Através da fabricação de filmes finos planares 2D baseados em heterojunções de hematite e TiO_2, foi estudado e otimizada a configuração de camadas duplas, as suas espessuras e otimização das condições de recozimento térmico. Filmes de Fe/Ti (e Ti/Fe) foram depositados por deposição de feixe de ions (IBD), com espessuras de Fe iguais a 60, 150 nm e espessura de Ti na ordem dos 5 ou 50 nm, a fim de explorar a melhor configuração e a espessura mais apropriadas para melhorar a fotorreresposta de fotoânodos.

Foi obtidas densidade de fotocorrente na ordem dos 0.7 mA/cm^2 para fotoânodos com uma camada mais fina de TiO_2 depositado na superfície da hematite. A melhoria do

desempenho desses fotoânodos foi alcançada diminuindo as taxas de recombinação dos pares eletrão-lacuna devido à menor espessura do fotoânodo e aumentando a absorção do fotoânodo devido à presença de uma camada de TiO_2. As propriedades bulk do fotoânodo também foram reforçadas pela promoção da difusão de Sn (doping) do substrato para a rede de hematite, através de uma abordagem de recozimento em duas etapas, atingindo uma temperatura máxima de 800 ºC.

Além disso, para continuar aumentando a eficiência desses fotoânodos, os filmes finos de Fe/Ti foram nanoestruturados através de anodização eletroquímica. Os óxidos anódicos nanoporosos obtidos permitem principalmente a diminuição do tamanho das estrutura, aumentando a área de superfície ativa, e encurtando o caminho para lacunas fotogeradas alcançarem a interface com o eletrólito, baixando sua recombinação. Neste trabalho, obteve-se uma melhoria de fotorreresposta na ordem de 200% quando comparada com a configuração de fotoânodo planar.

A influência dos co-catalisadores no desempenho do fotoânodo também foi testada por eletrodeposição de FeCo na superfície do fotoânodo. O co-catalisador óxido de FeCo mostrou uma melhoria significativa na fotocorrente de mais de 60%, bem como uma diminuição no potencial de Onset que marca o inicio das reações de divisão da molécula da água.

Os fotoânodos foram caracterizados por microscopia eletrônica de varrimento, espectroscopia de raios X dispersiva de energia, difração de raios X, UV-Vis e curvas de densidade de fotocorrente vs tensão, permitindo compreender o impacto da morfologia, propriedades estruturais, ópticas e fotoeletroquímicas no desempenho dos fotoânodos.

Contents

Acknowledgements v

Abstract vii

Resumo ix

Contents xi

List of Figures xv

1 Introduction 1
- 1.1 Sustainable Sources of Energy . . . 1
- 1.2 Harvesting Solar Energy . . . 2
- 1.3 Photoelectrochemical (PEC) cells for water splitting . . . 3
- 1.4 Semiconductors for PEC cells . . . 7
  - 1.4.1 Hematite . . . 9
    - 1.4.1.1 Hematite physical properties . . . 10
  - 1.4.2 Titanium dioxide (TiO_2) . . . 12
    - 1.4.2.1 Titanium Dioxide physical properties . . . 13
- 1.5 Strategies for photoanodes improvements . . . 14
  - 1.5.1 Nanostructures . . . 15
  - 1.5.2 Doping . . . 16
  - 1.5.3 Catalyst . . . 17
  - 1.5.4 Heterojunction . . . 17
  - 1.5.5 TiO_2 passive layer . . . 19
  - 1.5.6 Thermal annealing . . . 20
  - 1.5.7 Anodization . . . 21
    - 1.5.7.1 Thin films anodization . . . 24
  - 1.5.8 Alternative approaches . . . 24

2 Experimental Techniques 27
- 2.1 Materials, reagents and sample preparation . . . 27
  - 2.1.1 Material and reagents . . . 27
  - 2.1.2 Samples preparation . . . 28
- 2.2 Synthesis methods . . . 29
  - 2.2.1 Thin films deposition . . . 29

2.2.1.1 Ion Beam Deposition (IBD) . . . 29
2.2.1.2 Spin coating deposition . . . 30
2.2.2 Electrochemical anodization . . . 31
2.2.3 Annealing conditions . . . 32
2.3 Characterization Techniques . . . 32
2.3.1 Morphological Characterization . . . 32
2.3.1.1 Scanning electron microscopy . . . 32
2.3.1.2 Energy Dispersive X-ray Spectroscopy . . . 35
2.3.1.3 Stylus profilometry . . . 35
2.3.2 Structural Characterization . . . 36
2.3.2.1 X-ray diffraction . . . 36
2.3.3 Photoelectrochemical characterization . . . 38
2.3.3.1 Photocurrent density vs Voltage curves . . . 38
2.3.4 Optical absorption . . . 39

3 The role of thermal annealing on multilayered hematite and titanium dioxide thin films 41
3.1 Thin films deposition . . . 41
3.2 Influence of annealing conditions . . . 44
3.2.1 One step annealing . . . 44
3.2.1.1 Morphological characterization . . . 45
3.2.1.2 Structural analysis . . . 47
3.2.1.3 Optical characterization . . . 50
3.2.1.4 Photoelectrochemical performance . . . 52
3.2.2 Two step annealing . . . 53
3.2.2.1 Morphological Characterization . . . 53
3.2.2.2 Structural Characterization . . . 54
3.2.2.3 Optical Characterization . . . 56
3.2.2.4 Photoelectrochemical performance . . . 58
3.3 Conclusions . . . 60

4 The influence of Ti layers thickness in hematite photoanodes 63
4.1 Morphological characterization . . . 63
4.2 Structural characterization . . . 65
4.3 Optical characterization . . . 68
4.4 Photoelectrochemical Performance . . . 69
4.5 Conclusions . . . 70

5 The influence of hematite thickness in hematite-titanium dioxide thin films double-layers photoanodes 73
5.1 Fe thickness optimization . . . 73
5.1.1 Optical characterization . . . 77
5.1.2 Structural Characterization . . . 79
5.1.3 Morphological characterization . . . 82
5.2 Alternative Ti deposition . . . 83
5.2.1 Morphological and structural characterization . . . 84
5.2.2 Photoelectrochemical performance . . . 86

5.3 Improvement of the photoanodes photoresponse by FeCo oxide based co-catalyst . . . 88
5.4 Conclusions . . . 90

6 Nanostructured anodic hematite-titanium dioxide photoanodes **93**
6.1 Anodization advantages . . . 93
6.2 Anodization experiments . . . 94
6.3 Conclusions . . . 102

7 General Conclusions and future perspectives **103**
7.1 Main Conclusions . . . 103
7.2 Future perspectives . . . 104

A Sample list **107**

Bibliography **109**

List of Figures

1.1 Average photovoltaic power potential on Europe (Adapted from [6]) 3
1.2 Dark equilibration of hematite (n-type semiconductor) with an electrolyte containing a redox couple potential E. (a) Before equilibration; (b) departure from equilibration. (Adapted from [10]) 5
1.3 Basic principles of water splitting on a photoelectrochemical cell resorting in an n-type semiconductor photoanode to harvest the solar light, producing hydrogen at the cathode and oxygen on the anode. 6
1.4 Main requirements for a sustainable PEC cells. 7
1.5 The lower edge of the conduction band (red colour) and upper edge of the valence band (green colour) are presented along with the band gap in electron volts. The energy scale is indicated in electron volts using either the normal hydrogen electrode (NHE) or the vacuum level as a reference. On the right side the standard potentials of several redox couples are presented against the standard hydrogen electrode potential (Adapted from [2]). . . . 8
1.6 Hematite crystal structure (Adapted from [21]) 11
1.7 Absorption spectrum collected of hematite thin film deposited on F-doped tin oxide substrate (FTO) (Adapted from [12]) 12
1.8 Representation of the structural phases of TiO_2, anatase, rutile and brookite (Adapted from [40]). 14
1.9 Absorption spectra of Anatase and Rutile (Titanium dioxide phases). (Adapted from [41]). 14
1.10 SEM images of different morphological hematite nanostructures grown on the FTO coated glass substrate (Adapted from [10]). 15
1.11 Nanonet–hematite nanostructures and their performance for water splitting. (a) A schematic representation of the design. (b) The comparison of the photoelectrochemical performance between the nanostructure and planar hematite. (c) The external quantum efficiency comparison (measured at 1.53 V vs. RHE) (Adapted from [26]). 16
1.12 Maximum theoretical performance for hematite photoanodes [under AM1.5G 100 mW/cm^2 simulated sunlight]. Catalysis address the onset potentials and nanostructuration the saturation current. (Adapted from [28]). 18
1.13 Schematic of the band structure of the hematite–electrolyte interface, the intermediate surface states (i-SS), the recombination surface states (r-SS), and the oxygen evolution and the charge transfer reactions during the water splitting reaction under alkaline conditions. The i-SS local density of states (LDOS) for the Fe2O3 and Fe2O3/TiO2 samples before and after the post annealing are illustrated at the top (Adapted from [50]). 19

1.14 Schematic illustration of the different diffusion patterns of photoinduced charge carriers between (a) a plain hematite film photoanode and (b) a hematite nanowire array photoanode. Holes trapped in films can hardly diffuse to film surface due to their limited diffusion length (marked with X). Holes generated in a nanowire manage to move to the surface by diffusing horizontally across a small length (Adapted from [12]). 22
1.15 Transient curves of a typical anodization process and the respective derivate (Adapted from [58]) 23
1.16 UV−Vis absorption measurements of ultra thin hematite films coated on regular arrays of 3D conductive nanospikes (a) with different pitches, (b) Cross-sectional photon absorption profile of device on planar (left) and nanospike substrate (right). (Adapted from [44]). 25

2.1 Schematic illustration of Ion Beam Deposition system (Adapted from [64]) . 29
2.2 Ion Beam Deposition system used to deposit thin films (CEMUUP-MNTEC). 31
2.3 Schematic diagram of the core components of an Scanning Electron Microscope. (Adapted from [67]) 33
2.4 Different kinds of radiation generated by the electron beam interaction with sample on scanning electron microscopy (Adapted from [70]) 34
2.5 Schematic interactions of secondary, backscattered and Auger electrons with the sample atoms. (Adapted from [71]). 34
2.6 Profilometer system used to obtain the thickness of thin films (CEMUUP-MNTEC). 36
2.7 Representation of Bragg's law. (Adapted from [74]) 37
2.8 Rigaku XRD system used in the obtainment of thin films XRD spectra. . . . 37
2.9 Cappucino cell with three electrode configuration for j-V curve measurements (Adapted from [66]) 39

3.1 Scheme of the substrates (white) centered in the sample holder, and fixed with kapton tape (orange) at the bottom and top. 42
3.2 Thin film of Fe 150 nm/Ti 50 nm after deposition on FTO substrate 42
3.3 SEM images of (a) FTO substrate; (b, d) deposited thin films of Fe with a thickness of 150 nm (c) Ti with a thickness of 350 nm. 43
3.4 SEM images of (a) FTO substrate; and deposited thin films of (b) Fe 150 nm/Ti 5 nm; (c) Ti 5 nm/Fe 150 nm; (d, f) Ti 50 nm/Fe 150 nm; (e) Fe 150 nm/Ti 50 nm. 44
3.5 Transformation stages to produce double layer thin films of hematite and titanium dioxide. 45
3.6 Samples pre (top) and post annealed (bottom) of 550ºC during 2 hours. Samples composed by Ti(5 nm)/Fe(150 nm), marked as 1 (left); Fe(150 nm)/Ti(5 nm), marked as 7 (center); Fe(150 nm) marked as 11 (right). 46
3.7 SEM image of a (a) Fe150nm thin film before annealing; (b, c) Fe150nm thin film after annealing; (d) Fe150nm/Ti5nm thin film before annealing; (e, f) Fe150nm/Ti5nm thin film after annealing; (g) Ti5nm/Fe150nm thin film before annealing; (h, i) Ti5nm/Fe150nm thin film after annealing. The annealings were all performed at 550ºC (Conditions associated with annealing A, Table 3.1) 46
3.8 SEM image of a thin film of Ti5nm/Fe150nm produced by (a) Secondary electrons (b) Back-scattered electrons. 47

3.9 XRD spectra of thin films composed by $\alpha - Fe_2O_3$ and TiO_2, annealed at the temperatures of 550ºC and 600ºC. The peaks marked represent hematite and * symbol indicates FTO peak contributions. 48
3.10 XRD spectra of hematite and titanium dioxide thin films, evidencing the influence of TiO_2 layer on peak intensity and their positioning. Comparison between the different compositions at a) 600 ºC ; b) 550 ºC; Comparison at different annealing temperatures at c) Fe150/Ti5 compositions; d) Ti5/Fe150 compositions. 49
3.11 UV-Vis absorption spectrum of thin films of hematite and titanium dioxide. 51
3.12 j-V characteristic curve for the different photoanodes compositions in study, prepared with a one step annealing at 550 ºC and 600 ºC (a) Front illumination (b) Back illumination 52
3.13 Thin films transformations after an extra annealing step of 800 ºC during 20 minutes, (a, d) FTO/Fe150 after 550 ºC and 800 ºC, respectively; (b,e) FTO/Fe150/Ti5 after 550 ºC and 800 ºC, respectively; (c,f) FTO/Ti5/Fe150 after 550 ºC and 800 ºC, respectively. 54
3.14 XRD spectra of thin films composed by $\alpha - Fe_2O_3$ and TiO_2, annealed at the 550 ºC plus 800 ºC. The peaks marked represent hematite and * symbol indicates FTO peak contributions. 55
3.15 XRD spectra at the major peaks of hematite a) with all the configurations annealed at 800 ºC; and influence of the high annealing step on (b) Fe configurations (c) Fe/Ti configurations (d) Ti/Fe configurations. 56
3.16 UV-Vis absorption spectrum of thin films of hematite and titanium dioxide annealed at high temperatures. 57
3.17 j-V characteristic curves for thin films of hematite and titanium dioxide with one-step annealing at 550 ºC or with an extra-step at 800 ºC. (a) Front-illumination (b) Back-illumination 59

4.1 SEM image of the surface morphology of thin films annealed at 550 ºC with compositions of a) Ti5/Fe150; b) Fe150/Ti5; c) Ti50/Fe150; d) Fe150/Ti50. . 64
4.2 SEM image of the surface morphology of thin films annealed with an extra step at 800 ºC with compositions of a) Ti5/Fe150; b) Fe150/Ti5; c) Ti50/Fe150; d) Fe150/Ti50. 65
4.3 XRD spectra of thin films composed by hematite and TiO_2, annealed at low and high temperature. The peaks marked represent hematite, * symbol indicates FTO peak contributions and # represent the titanium dioxide phase. 66
4.4 XRD spectra at the major peaks of hematite and rutile, comparing the influence of Ti thickness variation in thin films on Fe/Ti configurations (a) annealed at 550 ºC (b) annealed at 800 ºC; and on Ti/Fe configurations (c) annealed at 800 ºC (d) annealed at 550 ºC. 67
4.5 UV-Vis characterization, depending on the variation of Ti thickness (a) at 550 ºC annealing temperature; (b) at 800 ºC annealing temperature; (c) Ti layers with 5 and 50nm (d) on Fe/Ti configurations. 68
4.6 j-V characteristic curves for photoanodes based on hematite and titanium dioxide (a) annealed at 550 ºC; (b) annealed with an extra step at 800 ºC. . . 70

5.1 j-V curves on the study of annealing influence of Fe 60 nm thin film photoanodes. (a) Front illumination (b) Back illumination. 75

5.2 Contour map of annealing temperature influence on photocurrent outputs of Fe photoanodes with variable thickness. 75
5.3 j-V curves on the study of annealing influence of Fe60/Ti5 thin film photoanodes. (a) Front illumination (b) Back illumination. 76
5.4 Contour map of annealing temperature influence on photocurrent outputs of Fe and Ti photoanodes. 77
5.5 UV-Vis characterization, with different annealing conditions for compositions of (a) Fe60; (b) Fe60/Ti5. 78
5.6 UV-Vis characterization, depending on the variation of annealing conditions for (a) different Fe thin film thickness, (b) with addition of a 5 nm Ti layer ; UV-Vis characterization of Fe thin films with and without 5nm of Ti at (c) low temperature annealings, (d) high temperature annealings. 79
5.7 XRD spectra of thin films composed by hematite and TiO_2 , annealed at low and high temperature. The peaks marked represent hematite, * symbol indicates FTO peak contributions. 80
5.8 XRD spectra at the major peaks of hematite, comparing the influence of Fe thickness (a) at 550 ºC annealing (c) at 800 ºC annealing; and on Ti/Fe configurations (b) annealed at 550 ºC (d) annealed at 800 ºC. 81
5.9 XRD spectra at the major peaks of hematite, comparing the influence of 5nm Ti layer addition (a) at 550 ºC annealing (b) at 800 ºC annealings. 81
5.10 SEM image of thin films surface morphology with variation on Fe thickness. (a) Fe150 annealed at 550 ºC (b) Fe60 annealed at 550 ºC (c) Fe150 annealed at 800 ºC (d) Fe60 annealed at 800 ºC. 82
5.11 SEM image of thin films surface morphology with variation on Fe thickness. (a) Fe150/Ti5 annealed at 550 ºC (b) Fe60/Ti5 annealed at 550 ºC (c) Fe150/Ti5 annealed at 800 ºC (d) Fe60/Ti5 annealed at 800 ºC. 83
5.12 XRD spectra of thin films composed by hematite and TiO_2, annealed at low and high temperature. The peaks marked represent hematite, * symbol indicates FTO peak contributions. S.C. represents a layer of Ti deposited through spin coating, with a approximated thickness of 6 nm. 84
5.13 XRD spectra at the major peaks of hematite, comparing the influence of Ti layer addition deposited through IBD and spin coating. (a) Fe60 with Ti contributions on the top, annealed at 550+800 ºC (b) Fe150 with Ti contributions on the top, annealed at 550+800 ºC (C) Fe60 with Ti contributions, annealed at 550+800 ºC (d) Fe thickness variation with Ti spin coated on the top and annealed at 550+800 ºC. 85
5.14 SEM image of thin films surface morphology with variation on Fe thickness with spin coating deposition of Ti. (a, c) Fe60/S.C. annealed at 550+800 ºC (b, d) Fe150/S.C. annealed at 550+800 ºC. 86
5.15 j-V curves of Fe photoanodes enhanced with a Ti layer deposited through spin coating deposition (a) Front illumination, (b) Back illumination. 87
5.16 j-V curves comparison between Fe photoanodes enhanced with a Ti layer deposited through spin coating deposition or by IBD, on Fe150 photoanodes (a) Front illumination, (b) Back illumination. Comparison on Fe60 thin films with the Ti layer addition (c) Front illumination (d) Back illumination. 88
5.17 j-V curves before and after the electrodeposition of FeCo catalyst on Fe 150 nm thin film annealed at 550 ºC. 90

6.1 Electrochemical anodization curves of thin films of (a) Iron (b) Titanium at different potentials, thicknesses and time duration 94
6.2 Electrochemical anodization curves of Fe and Ti thin films double-layers for (a) Fe150 and Fe150/Ti5 (b)Fe150/Ti50 and Ti50/Fe150. 95
6.3 j-V curves comparison between anodized and non anodized Fe photoanodes (a) Front illumination (b) Back illumination; and with the addition of a 5nm Ti layer (c) Front illumination (d) Back illumination. All the films were annealed at 550 ºC for 2h. 96
6.4 Anodized thin films (Top) of (a) Fe150 (b) Fe150/Ti5, compared with the non anodized ones (Bottom) (c) Fe150 (d) Fe150/Ti5. All the films were annealed at 550 ºC. 97
6.5 SEM images after anodization, presenting (a) recurrent bubble zone formation on Fe150 thin films and (b) residual board zones on Fe150/Ti5 thin films. Both films were annealed at 550 ºC 98
6.6 j-V curves comparison between anodized and non anodized Fe150/Ti50 thin films(a) Front illumination (b) Back illumination; and Ti50/Fe150 thin film (c) Front illumination (d) Back illumination. 99
6.7 j-V curves comparison between anodized Fe150/Ti50 and Ti50/Fe150 thin films(a) Front illumination (b) Back illumination. 100
6.8 Non anodized thin films (Left) of Ti50/Fe150 (a) annealed at 550 ºC (c) annealed at 550+800 ºC and the respective anodization (right)with annealings at (c) 550 ºC (d) 550+800 ºC. 100
6.9 Non anodized thin films (Left) of Fe150/Ti50 (a) annealed at 550 ºC (c) annealed at 550+800 ºC and the respective anodization (right) with annealings at (c) 550 ºC (d) 550+800 ºC. 101
6.10 Surface morphological characteristics of anodized Fe150/Ti50 thin films (a,b) annealed at 550 ºC (c,d) annealed at 550+800 ºC. 101

Dedico esta dissertação à minha irmã Eva

Agora é a tua vez !!!

Chapter 1

Introduction

In this chapter, it is presented the urge to develop an environmentally friendly source of energy, followed by the working principles and the requirements of a photoelectrochemical cell. The properties of the materials studied in this dissertation are also presented in this chapter as the methods for the materials photoresponse optimization.

1.1 Sustainable Sources of Energy

Over the decades, the society energetic needs have grown drastically [1, 2], mainly due to the increase of global population combined with the drastic high energetic consumption of the modern lifestyle. Adding to this major concern, it is associated the use of pollutant sources of energy that are the principal greenhouse gases emitter [3], causing several negative and drastic effects on the planet, approaching the world to a non-return point.

To overcome this world critical point, long term solution is required, or even a combination of several ones, supported by energy sources that are renewable, environmentally friendly, with a considerable ratio of cost-efficiency, ideally, capable of producing energy to answer all the current and future world's society needs.

Although the unpleasant effects of fossil fuels, another factor that contributes to their urgent replacement solution, is the limited reservoirs lifetime, making the search for new and optimized energy sources an unavoidable problem for the mankind. Taking into account the recent rates of consumption, it is predicted that the oil, gas and coal have their reservoirs depletion around 25, 27 and 97 years [4] , respectively, reinforcing the energy problematic and the need for new and optimized sources.

Among the various sources of renewable energy, solar energy stands out has one of the most promising ones, since is a clean, sustainable, abundant energy source. The total value of the energy supplied by the sun to the earth, per year, is around $3 * 10^{24}$ Joules, quantity that outperforms the annual consumption by a factor of 10000 times [2].

Solar energy can be strategically harvested and converted in electric power or used to generate fuels, such as green hydrogen [2]. H_2 can be used directly after its production or stored for latter applications.

Despite the stunning values of the possible solar energy for harvest, the consumed energy that comes from the sun, at the moment, is around 1%, mainly by the use of photovoltaic technology [1]. However, there is a need to have an energy source that allows the final product to be stored for later use, which makes photoelectrochemical (PEC) cells a very attractive technology. This cells combine in one single device the ability to harvesting solar energy with an electrolysis system, converting water into hydrogen and oxygen by light-induced electrochemical processes [1].

1.2 Harvesting Solar Energy

Solar energy takes a lead place on the most abundant renewable energy resources. Taking into account the income energy values of the previous section, that with a covering of only 0.1% of the earth's surface with solar cells, with an efficiency of 10%, it would be enough to suppress all the present world's energetic needs [2]. However, some drawbacks are difficulty to store for transport and nightime use [5].

The solar irradiation on earth depends on factors like latitude, tilt of the measuring surface, height of the sun, climate or geographic variation. On the European picture, Portugal and Spain, are the countries with most potential to benefit from this type of energy, as shown in Figure 1.1. Therefore this opens a window opportunity for intensive investment and research on the harvest of energy from the sun.

Among all the methods to transform the energy coming from the sun into new forms, the photoelectrochemical cells provide a green way to produce hydrogen (fuel) from sustainable resources (water and sunlight), offering a solution to the energy problematic, with no negative impact on the environment, unlike other processes to produce energy [7]. Another important feature that stands out from the other methods is the possibility to resort on low-cost and abundant materials as well as posses a compact and integrated design, when compared PV/electrolysis systems.

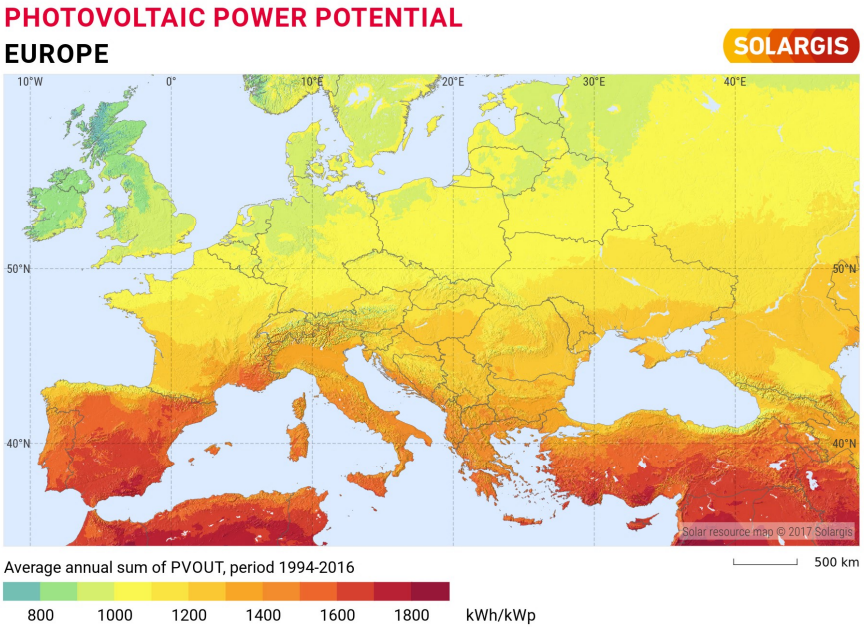


FIGURE 1.1: Average photovoltaic power potential on Europe (Adapted from [6])

After produced and collected, the green hydrogen can be used for multiple applications, powering a wide range of devices. One of the most promising goals to use H_2 as fuel is to be the main source of supply for the transportation, or with benefits of could be domestically produced with no harmful gas emissions.

1.3 Photoelectrochemical (PEC) cells for water splitting

Photoelectrochemical (PEC) cells are devices capable of efficiently split water into storable hydrogen, generating clean and sustainable energy source. These cells, have become a very interesting process to achieve the energetic goals established by the United Nations and European Commission [1].

The final product, 'green' hydrogen, can be stored for applications post-production, which is a major advantage once the use of fuels had a participation higher than 70% (data from 2011) on the energy consumption [5], and green H_2 presents itself as a solution without environmental harm.

This process stands out from the other methods of hydrogen production, once it can rely on abundant and low-cost materials with expected efficiencies above the theoretical threshold of viable application [1, 8], producing highly pure hydrogen from renewable and non-prejudicial sources, rather than fossil fuels such as natural gas or coal (the major hydrogen sources still used).

The main concerns about this technology are related with the stability and the energetic properties of the cell [1]. The efficiency of the process should have at least 10% of energy conversion efficiency [1], this threshold marks the minimum efficiency level required to make PEC cells a competitive commercial solution. Another major issue is the separation of the reaction products, hydrogen and oxygen, that bring safety concerns about the use of these devices [1].

Photoelectrochemical process;

The photoelectrochemical process consists essentially in the dissociation of water, via charge carriers, in its basic components, hydrogen (H_2) and oxygen (O_2).

A PEC cell, represented in Figure 1.3, is composed by two electrodes, where one of them must be photoactivated under illumination (semiconductor material), both immersed in an aqueous electrolytic solution with the appropriated reduction-oxidation pairs [1, 7]. When the semiconductor photoelectrode absorbs photons with enough energy to eject the electron from the valence band into the conduction band, electron-hole pairs are photogenerated [2, 7, 9] expressed by the following overall process equation:

$$2h\nu + semiconductor \rightarrow 2e^- + 2h^+ \tag{1.1}$$

where $h\nu$ is the photon energy (h = Planck constant ; ν = frequency).

The photogenerated electrons and holes are spatially separated due to an electric field on the space charge layer (SCL), caused by the electric flow between the semiconductor and the electrolyte in order to achieve the electronic equilibrium [2, 10] (Figure 1.2). After charge separation, the electrons are directed to an external circuit, towards the counter electrode, where they will reduce the water and produce hydrogen (Equation 1.2). While the holes move through the semiconductor to the interface with the electrolyte, oxidizing the water and producing oxygen (Figure 1.2, Equation 1.3) [2, 9]:

Electron at cathode reaction:

$$4H_20 + 4e^- \rightarrow 2H_2 + 4OH^- \qquad E_{H_20|H_2} = -0.828V \tag{1.2}$$

Holes at anode reaction:

$$4OH^- + 4h^+ \rightarrow 2H_2O + O_2 \qquad E_{0_2|OH^-} = -0.401V \tag{1.3}$$

Resulting in a overall reaction for the photoelectrochemical water splitting of:

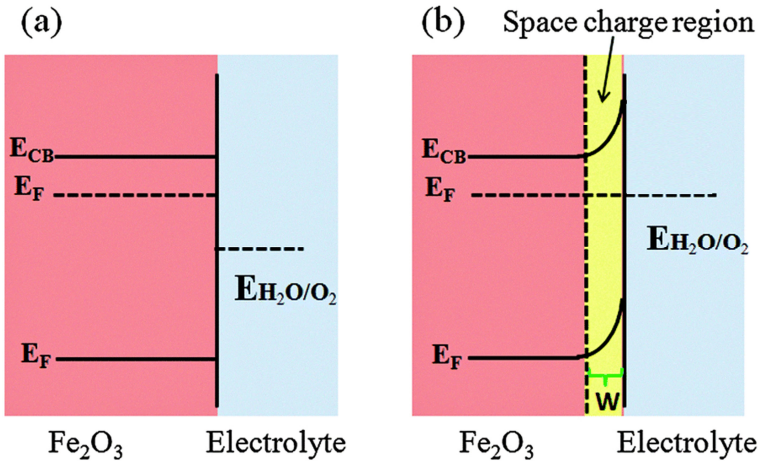


FIGURE 1.2: Dark equilibration of hematite (n-type semiconductor) with an electrolyte containing a redox couple potential E. (a) Before equilibration; (b) departure from equilibration. (Adapted from [10])

$$H_20 + h\nu \rightarrow H_2 + 0.5O_2 \tag{1.4}$$

with $\delta G = 237kJ/mol$ [11], where G stands for the Gibbs free energy.

The previous equations are written regarding a basic media. Considering acidic media, the equations are obtained by subtracting or adding the dissociation reaction of water into protons and hydroxyl ions [2].

At the cathode:

$$2H^+ + 2e^- \rightarrow H_2 \qquad E_{H^+|H_2} = 0.0V \tag{1.5}$$

At the anode:

$$H_2O + 2h^+ \rightarrow 2H^+ + 0.5O_2 \qquad E_{H_20|H_2} = 1.23V \tag{1.6}$$

If the charge carriers, especially the minority charge carriers, are unable to interact with the water molecules, their recombination and perish will occur, limiting the hydrogen production [12]. It is also extremely important to have in attention that the semiconductor photoelectrode should have a adequate bandgap width and the potentials edges of the conduction and valence bands should fit as much as possible with the water reduction and oxidation potentials. The bottom level of the conduction band should be more negative than the reduction potential of H^+/H_2 (0 V vs NHE - Normal Hydrogen Electrode)

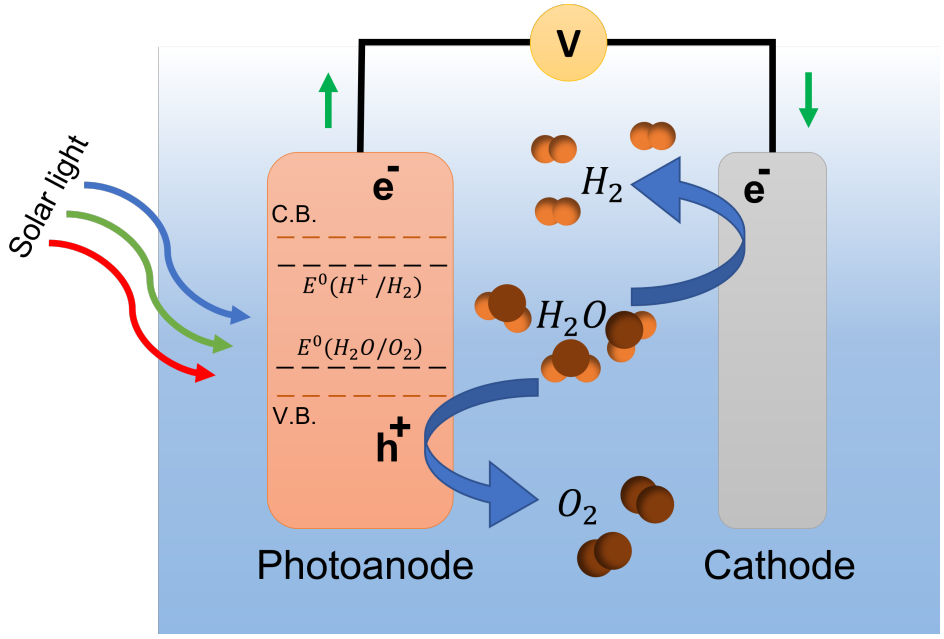


FIGURE 1.3: Basic principles of water splitting on a photoelectrochemical cell resorting in an n-type semiconductor photoanode to harvest the solar light, producing hydrogen at the cathode and oxygen on the anode.

and the top level of the valence band should be more positive than the oxidation potential of O_2/H_2O (1.23 V vs NHE) [9].

Photoelectrochemical cells versus Photovoltaic-Electrolysis

Photovoltaic (PV) systems also rely on the principle of the incident photons to create electron-hole pairs that produce an electrical potential difference at the semiconductors interface [2]. Combining the PV system with an electrolyzer, it is possible to produce green and sustainable hydrogen, with a few differences from the PEC cells.

Unlike PEC cells that have an integrated system, photovoltaic-electrolysis (PV-E) have the light absorption component (PV) physically separated from the water splitting component (Electrolyzer) [13, 14]. That feature allows the separated optimization of components [13], which can accelerate the technological development, having however the need to have separated support structures and encapsulation for each part of the system [13].

On the efficiency comparison, PV-E systems on long stable processes take the lead with a maximum efficiency of 30 % for $>$ 48 h [13, 15] against the 10 % for $>$ 40 h [13, 14] of PEC cells. However, the PV-E technology is much more mature and studied than PEC devices which are in the early stage of development [13], with future investments from the Portuguese government on a large scale central at Sines [16], producing green hydrogen for internal consumption and exportation, leading to great expectations on cost

and energy savings over coupled photovoltaic [17].

1.4 Semiconductors for PEC cells

In 1972, Fujishima and Honda reported successful photochemical water splitting, using titanium dioxide (TiO_2) as photoelectrode [18]. Since that water photolysis, TiO_2 has been one of the most studied semiconductors [2]. Several other semiconductor materials have been deeply studied in an attempt to enhance the efficiencies of the process, highlighting materials such as Fe_2O_3, WO_3, $BiVO_4$, SnO_2 and Cu_2O [1].

For water photoseparation to occur in a sustainable way, it is necessary to meet several properties of the semiconductor, e.g. bandgap energy, flat band potential (Figure 1.5), stability to corrosion in aqueous media and under lighting (photocorrosion) [1, 7, 19] and sufficient (sun) light absorption in the region of visible [1, 7]. The optimization of these parameters is crucial since they influence the PEC performance. For the PEC cells to be sustainable and to be a future alternative for the production of green energy, it is necessary a device implementation with low-cost, and scalable materials and methods, abundant and non-toxic materials (Figure 1.4), competing with other alternatives on the market.

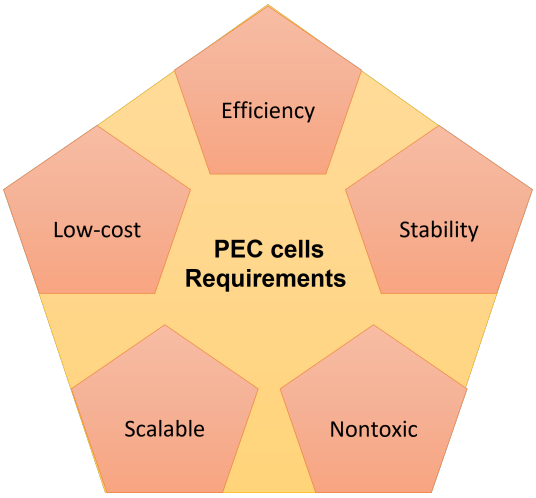


FIGURE 1.4: Main requirements for a sustainable PEC cells.

It is also important to note that according to theoretical calculations, for commercial applications, it is necessary that the solar to hydrogen (STH) efficiency achieved should be at least 10%, enabling the use of technology to the detriment of others [12].

A great part of literature, broadly agrees that the optimal semiconductor to be used in this type of applications should have a band gap energy close to 2 eV [7, 20]. This value

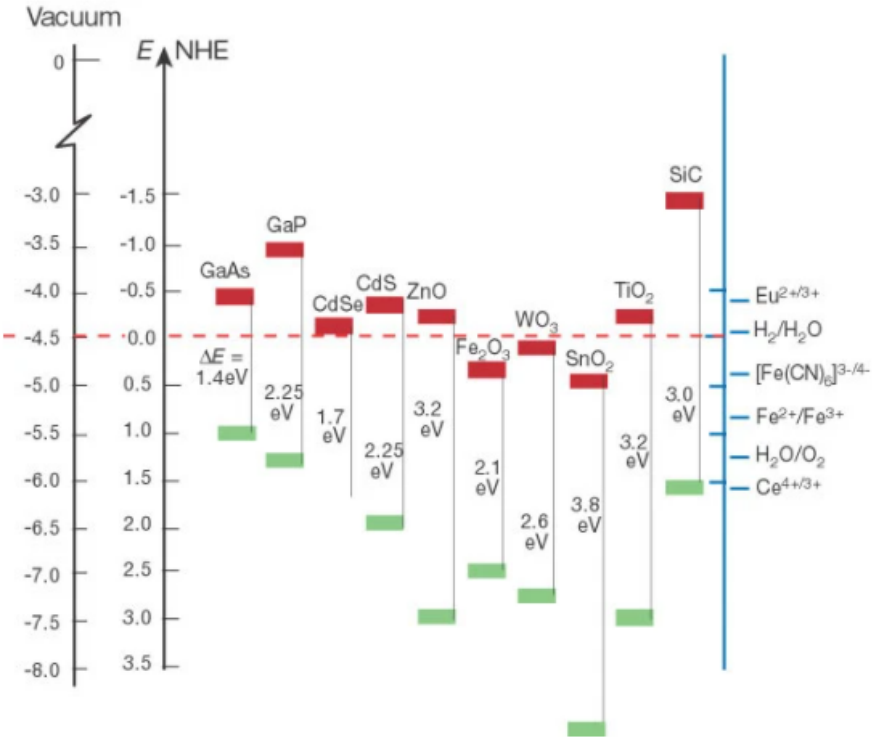


FIGURE 1.5: The lower edge of the conduction band (red colour) and upper edge of the valence band (green colour) are presented along with the band gap in electron volts. The energy scale is indicated in electron volts using either the normal hydrogen electrode (NHE) or the vacuum level as a reference. On the right side the standard potentials of several redox couples are presented against the standard hydrogen electrode potential (Adapted from [2]).

is due to the required water splitting potential (1.23 eV) plus all the predicted dissipation of energy like ohmic drop losses or overpotencials [20].

A promising stability photoelectrode for electrolysis of water is given by oxide semiconductors (n and p type) [1], which is a great part of the cases is allied to an low-cost and abundance of the material.

In order not to compromise the low-cost of materials, it is necessary that the methods of preparing the photoelectrodes are equally efficient, simple and can be feasible without the need for a large amount of resources.

Due to the properties requirements to achieve a sustainable PEC cell to compete against other sources of energy, this thesis will focus on the production and characterization of hematite and TiO_2 based photoanodes, where properties as abundance, low-cost, stability and non-toxicity are some of those materials advantages. In the following sections, the advantages and disadvantages of those materials will be deepened, as well as the strategies to overcome the drawbacks.

1.4.1 Hematite

Iron, one of the most available metals on the earth crust [21, 22] can lead to several oxides of different stoichiometry and crystalline phases, each one yielding unique properties [23].

When exposed to atmospheric air, this element easily oxidizes into ferrous (2+) and ferric (3+) states [21]. Due to the properties of abundance and low price, iron and their oxides are extensively studied and used, with applications that goes from the quotidian life to high technology laboratories.

Among the several iron oxide forms, hematite ($\alpha - Fe_2O_3$) is the most common form of crystalline iron oxide (Figure 1.6) [21] and it is also the most thermodynamically stable phase under ambient conditions [21, 23, 24], behaving as a n-type semiconductor material with high chemical stability. $\alpha - Fe_2O_3$ is widely investigated as a potential candidate for diverse applications, such as solar energy conversion, electrochromism, photocatalysis, interference filters and photo-oxidation of water [23].

The use of hematite in photoanodes for PEC cells is very attractive once this material is abundant, low-cost, non-toxicity. Moreover, it has an excellent long-term stability against photocorrosion and a suitable band gap ($1.9 - 2.2$ eV) [7, 8, 10, 19, 23–25], allowing to reach the theoretical solar-to-hydrogen (STH) conversion efficiency around 16 % [7, 8, 10, 26] (or photocurrent generation of 12.6 mA/cm^2 at 1.23V vs. RHE under 1-sun irradiation) [7, 27, 28], which is significantly larger than the required efficiency needed for a competitive PEC cell (10% of efficiency). However the energetic conversion efficiencies are very reduced. This small performance can be assigned to low electron mobility ($0.01 cm^2V^{-1}s^{-1}$ to $0.1 cm^2V^{-1}s^{-1}$) [7, 8, 19, 29] resulting in short lifetime for the photogenerated electron-hole pairs, short hole diffusion length (2 - 4nm) [7, 8, 19, 22, 24, 29–31] when compared with light penetration depths (approx. 120 nanometers at $\lambda = 550nm$) [8, 31].

It has also poor conductivity ($10^{-14}\Omega^{-1}cm^{-1}$) [8, 12] and the incompatible flat band potential for spontaneous water splitting also reduces the efficiency once it's needed to resort to an external voltage bias [19, 26, 32].

Despite all the disadvantages, the hematite possesses a high stability under most of the aqueous environments, being by far the only photoanode assessed over 1000 h of operation under simulated illumination of one sun, without significant losses on the performance [29].

The valence band maximum is composed mainly by Fe-3d t_{2g} and O-2p while the conduction band minimum is composed by Fe-3d e_g [25], where the photogenerated holes come from direct $0^{2-}2p \rightarrow Fe^{3+}3d$ transitions ($\lambda < 400$ nm) and from indirect $Fe^{3+}3d \rightarrow 3d$ transitions ($\lambda < 620nm$) [25]. When compared this two main transitions, the direct one have a higher impact on the absorption coefficient [25].

To overcome the hematite limitations (and of the other semiconductor oxide materials), several approaches can be taken into account. The nanostructuring of a semiconductor photoanode deeply affects the resultant photoconversion efficiencies [19, 24, 33] once it increases the active area, provide shorter paths for charge carriers reactions and interferes on the bandgap. Recombination rates of electron-hole pairs can be minimized, especially on low mobility materials, by decreasing the relevant architectural feature sizes (from 2D or 1D dimension reduction) to less than the minority carrier diffusion lengths[19].

It is also important to note, that in hematite, due to the short diffusion length of holes, only those who are generated near the electrolyte interface can have a positive contribution to the process, while the others, recombine with electrons before reaching the surface.

Another approach to reduce the recombination and enhance the material efficiencies is linked to the introduction of external elements on the lattice such as Ti^{4+}, Ca^{2+}, Cu^{2+}, Si^{4+}, Mo^{6+} [33, 34], leading to structural changes on the photoelectrodes.

Introducing heterojunction interfaces on the photoelectrodes also increases the charge separation due to a slight external bias.

1.4.1.1 Hematite physical properties

Crystalline structure;

Hematite ($\alpha - Fe_2O_3$) is the most abundant form of crystalline iron oxide, holding a high thermodynamic stability. The atoms of oxygen and iron are arranged in a corundum structure and crystallizes in a rhombohedral lattice system belonging to the space group R-C3 with lattice parameters of a = 5.0356 Å, c = 13.7489 Å [21], with the O^{2-} anions arranged in a hexagonal closed-packed lattice along the [001] c-axis direction [21] while the Fe^{3+} cations occupy two-thirds of the octahedra [12].

The lattice can be represented as an alternation of iron bilayers and oxygen layers parallel to the (001) basal plane. Fe^{III} atoms within each bilayer have parallel spins, while adjacent bilayers have opposite spins. Electrons can move by hopping through Fe^{II}/Fe^{III} valence change within the iron bilayers, while electron exchange between neighboring

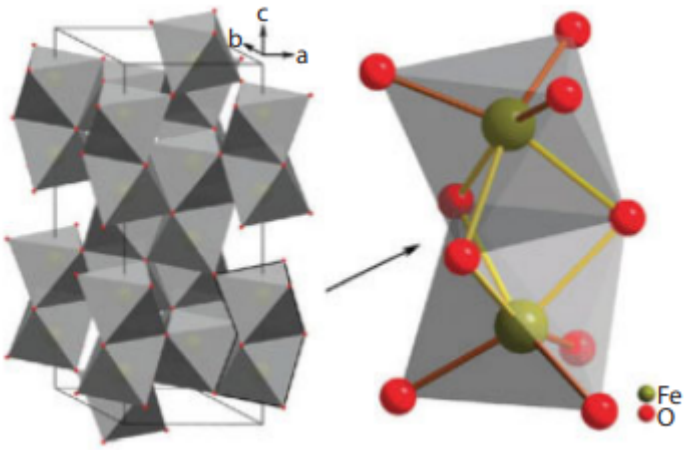


FIGURE 1.6: Hematite crystal structure (Adapted from [21])

bilayers is spin forbidden (Hund's rule) [30]. This behaviour is the classical explanation for the strongly anisotropic conductivity of hematite, which is up to 4 orders of magnitude higher within the (001) basal plane (e.g., in [110] direction) than orthogonal to them [7, 30].

Optical properties;

Hematite possesses a indirect bandgap with typical values between 1.9 - 2.2 eV, [12, 21] where the lower band gaps are related with higher crystallinity degrees and lower concentration of defects [12]. On this material, the photons absorption starts near infrared region where weak absorption bands are due to d-d transition states between electron energy levels of the Fe^{3+} ions, which are split by an intrinsic crystal field [21].

Hematite possesses a good absorption of photons from the yellow to the ultraviolet region of the visible spectrum (Figure 1.7) and the transmission of orange to infrared photons originates the characteristic reddish color of the material [21].

To absorb 95% of the incident photons (considering that all the photons have a wavelength of 550nm), hematite must have an approximated thickness of 350nm, however those photons can only penetrate to an approximated maximum depth of 120nm [12], leading to an inefficient absorption process. Due to this discrepancy, in order not to waste radiation energy, a proper morphological material engineering is required to maximize the light harvest efficiency [12].

Electronic Properties; At room temperature, $\alpha - Fe_2O_3$ carrier mobility is in order of $10^{-2} cm^2 V^{-1} s^{-1}$ [12, 21]. This low mobility is explained by the strong interactions between

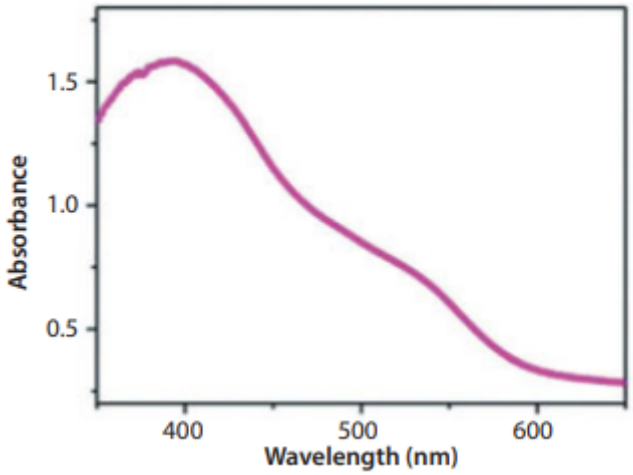


FIGURE 1.7: Absorption spectrum collected of hematite thin film deposited on F-doped tin oxide substrate (FTO) (Adapted from [12])

electrons and phonons that cause the trapping of free electrons or holes by local lattice distortion [12]. In addition, polycrystalline hematite also shows a poor electrical conductivity $10^{-14}\Omega^{-1}cm^{-1}$ [12, 21], which allied to the low charge mobility represents the mains disadvantages for hematite photoanodes. Those disadvantages are expressed by short lifetime of electron-hole pairs (3 - 10 ps) [8, 12, 21, 31] and short hole diffusion length (2 - 4nm) [8, 12]. Is important to refer that electric conductivity of hematite is anisotropic with a magnitude of four times higher on basal planes when comparing with the value arising along the [001] direction. This difference is due to the hopping mechanism related to Fe^{2+}/Fe^{3+} valence state alternation within the iron bilayers [12, 21].

1.4.2 Titanium dioxide (TiO_2)

Titanium dioxide (TiO_2), also know as titania is the only naturally occurring oxide of titanium at atmospheric pressure [35]. It is extensively studied due to the electric, magnetic, catalytic and electrochemical properties, providing useful applications on the catalysis, electrochromism and sensors [36].

TiO_2 main crystalline phases are anatase, rutile and brookite (Figure 1.8) [9, 36–39], where rutile is the most stable one [9, 35, 39, 40], and anatase and brookite represent metastable phases, capable to be converted to rutile by heating [35, 39].

Since the water photolysis experiments by Fujishima and Honda, devices based on TiO_2, gained a very attractive and promising for the production of H_2 [2, 9, 36]. Due to

the low recombination rates of photogenerated pairs, anatase is the preferential and most investigated phase for this type of applications [37].

The use of titanium dioxide in photoanodes for PEC cells is supported by its properties of abundance, non-toxicity, low-cost [40] and by a suitable bandgap to the red-ox potential for the $H_20 \bullet OH$ reaction, allowing photogeneration of oxygen through water splitting [19]. However, independently of TiO_2 crystallographic phases, the band gaps limits the activation to UV radiation [2], with approximated values of 3.0 eV for rutile and 3.2 eV for anatase phase [9, 19, 30, 35, 37, 39], which restrains the absorption fraction to light below 420 nm [30] which corresponds to 5% of the solar light [9, 19, 37]. Since anatase presents promising characteristics for PEC applications but it is a meta stable phase, it is important to compare with the thermostable phase, rutile.

1.4.2.1 Titanium Dioxide physical properties

Crystalline structure

Anatase and rutile crystallographic phases present a tetragonal structure [35, 36, 39, 40], with lattice parameters of a = 0.3785nm; c = 0.9514nm on space groups I4/amd and a = 0.4594 nm; c = 0.29589nm on P42/mnm space group, respectively [35, 40]. Their structures are built upon the connection of TiO_6 octahedra [9, 35, 40], where each Ti^{4+} ion is surrounded by an octahedron of six O^{2-} ions [9], occurring a two sharing edge oxygen pairs and eight sharing corner oxygen atoms on rutile, while anatase has a four sharing an edge and four sharing a corner [9, 35].

The distance between Ti atoms on anatase is larger than on rutile and the distance between Ti - O is shorter [9]. These differences on the crystalline structure of each phase cause variations on mass densities ($\rho_{anatase} = 3894 kg/m^3$ and $\rho_{rutile} = 4250 kg/m^3$ [35]) and on electronic band structures [9].

The phase transformations of TiO_2 highly depend on the synthesis parameters [35], here the transition temperatures vary in a wide range (400-1200ºC) [35, 39]. Anatase transformation to rutile involves the breaking and reforming of bonds [35], presenting a contraction of the c-axis and a overall volume contraction of approximately 8% [35].

Optical properties

Anatase appears to have a wider optical absorption gap and a smaller electron effective mass, resulting on a higher mobility for the charge carriers [36].

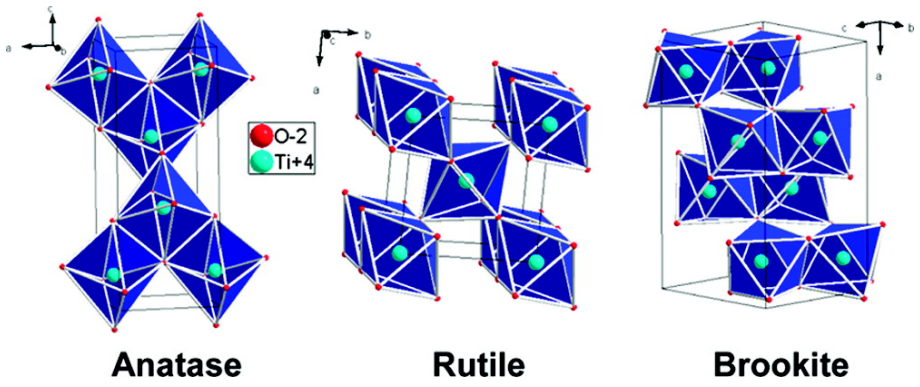


FIGURE 1.8: Representation of the structural phases of TiO_2, anatase, rutile and brookite (Adapted from [40]).

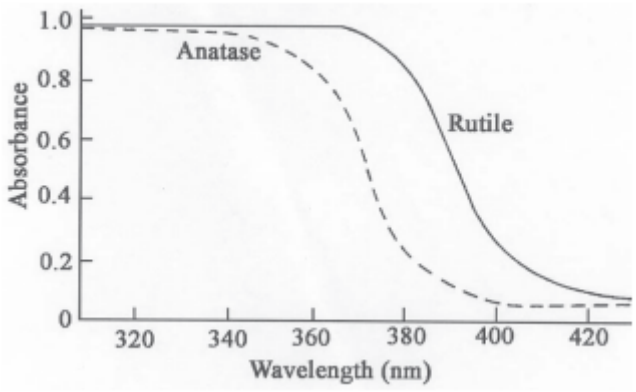


FIGURE 1.9: Absorption spectra of Anatase and Rutile (Titanium dioxide phases). (Adapted from [41]).

One major factor of impact on the performance of TiO_2 materials its optical activity (Figure 1.9). The increase on this parameters, and consequently, the increase on the performance, can be done by the on set shift from UV to visible region [9]. To achieve that goal, one possible solution is to dope the material with other elements that can narrow the electronic properties and, thus, alter the optical properties [9].

1.5 Strategies for photoanodes improvements

The combination of materials and their structuring opens the possibility to enhance the beneficial properties of the materials and attenuate some of its drawbacks, increasing their performances.

The drawbacks can be mitigated through nanostructure engineering, doping, catalysts, heterojunctions, passivation layers on the interface with electrolyte and/or FTO and thermal annealing [42].

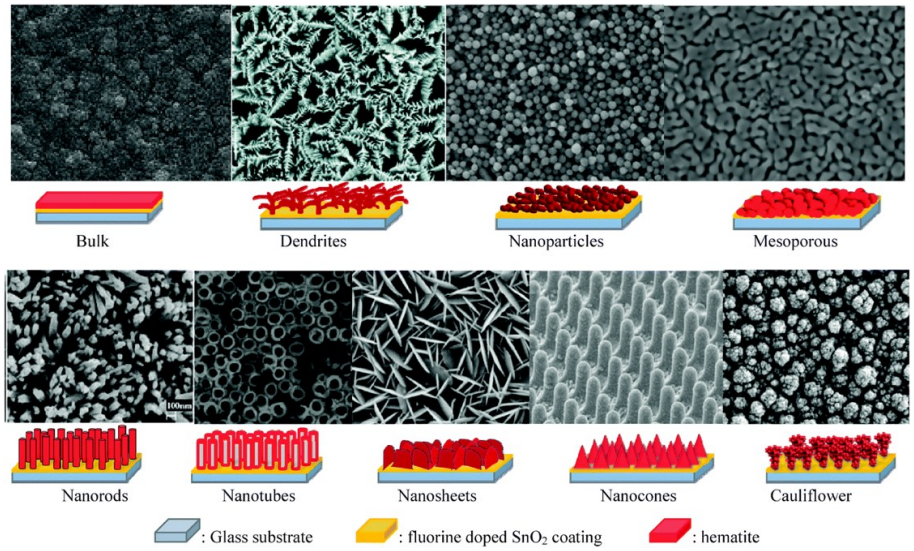


FIGURE 1.10: SEM images of different morphological hematite nanostructures grown on the FTO coated glass substrate (Adapted from [10]).

1.5.1 Nanostructures

The recent increase on nanoscience and nanotechnology researches allowed to study new physical and chemical properties that emerge when the size of the material reach extremely small scales [9], occurring the confinement of electrons to two, one or even zero dimensions. The geometry and size of materials affects their properties, once it occurs the quantum confinement of electrons, arising distinguishable properties from the bulk [2, 9].

Despite all the optimization of the physical properties offered by the nanostructuring, the change in architecture improves by itself the efficiency, once the surface area is higher, offering more available sites for chemical reactions and reduces the distance needed to the holes reach the reduction sites, decreasing the recombination rates. The nanostructure sizes should also be taken in account, once it highly influences the performance of devices [9].

One of hematite's major problem is its high recombination in the bulk of semiconductor. Nanostructures grow with dimensions comparable with the width of SCL can reduce the recombination processes [43], leading to more charge carriers to participate in the chemical processes. As in hematite, the performance of TiO_2 based devices is highly influenced by the sizes of the nanostructures [9].

Due to the nanostructuration benefits, several structures such as nanowires, nanodentrites, nanotubes and more were produced to improve the PEC cells performance [44] (Figure 1.10 and 1.11).

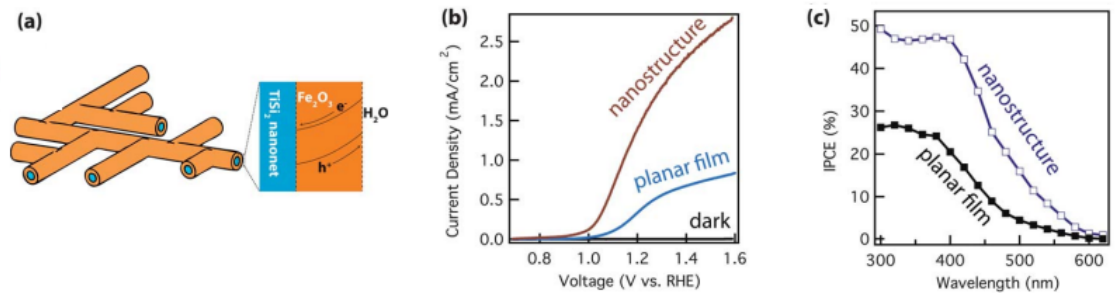


FIGURE 1.11: Nanonet–hematite nanostructures and their performance for water splitting. (a) A schematic representation of the design. (b) The comparison of the photoelectrochemical performance between the nanostructure and planar hematite. (c) The external quantum efficiency comparison (measured at 1.53 V vs. RHE) (Adapted from [26]).

1.5.2 Doping

Doping intrinsic semiconductor materials by the intentional introduction of chemical impurities is capable of modulate the electrical, optical and structural properties, forming an extrinsic semiconductor [12].

The reformulation on the structure of the material allows the device to overcome their limitations, improving the output efficiencies. On the particular case of hematite PEC cells performance, the main interest is to lower the recombination rates of the photogenerated electron hole pairs and adjust the potentials of conduction and valence band to the potentials of water splitting.

Despite the benefits of doping, beyond a minimal concentration the introduced metal ions could serve as recombination centers for the photogenerated electron-hole pairs [19].

Doping hematite has been extensively investigated to enhance the material's properties [45]. Depending on the dopant element, it is possible to increase the donor density, which improves the electrical conduction [7, 46], the mobility or lifetime of minority chargers [46], increasing the quantity that can reaches the electrolyte interface and participate on the chemical reactions [46].

The dopant element can also act like a structural agent, producing more optimized nanostructures that allows a better performance on the absorption of light or shorter paths for charge carriers [46]. At the surface, dopants can behave as catalysts enhancing the reactions [46] or even passivating the surface and/or grain boundaries, reducing spots of recombination [46].

In 2013, Jae Young Kim et al, achieved a breaking performance of 4.32 mA/cm^2 at 1.23V vs. RHE, using hematite as main constituent of the photoanode, corresponding to

34% of the maximum theoretical limit expected [7]. Platinum was used for dopant, which improved the charge transfer and it was used a two-step annealing at 550°C and 800°C of $\beta - FeOOH$ [7]. Other reported cases of doping performed with Ti [45], Si [45] and others, reveled enhanced efficiencies.

1.5.3 Catalyst

The critical step in the PEC water splitting reaction is the oxygen evolution reaction (OER) on the anode side, with slow kinetics attributed mainly to the small hole diffusion length that leads to high-efficiency losses [47]. Such limitations can be overcome by application of catalysts overlayers at the semiconductor photoelectrodes surface to enhance the kinetics of oxygen evolution reaction [33]. Cocatalysts on photoanodes can improve the photocurrent and negatively shift the onset potential by decreasing the activation energy [10] (Figure 1.12), enhancing the PEC cell performance.

Some requirements for a good catalyst performance include high catalytic activity, high surface area, which allows to minimize the quantity of catalyst that is required, a high electrical conductivity at high electrode potentials to minimize the ohmic drop in the material, use of low-cost and widely available materials, and present a high corrosion stability [47]. Several materials have been widely used as cocatalyst to improve the photoanodes efficiencies, such as metals (Co, Fe, Ru, Ir, etc.), metal oxides (IrO_2 and RuO_2), or materials such as cobalt phosphate, nickel borate, iron oxyhydroxide and nickel hydroxide derivatives [33].

1.5.4 Heterojunction

The combination of two or more semiconductors into a photoelectrode, on a called heterojunction, can positively influence the photoanode structural properties [7] as well as a more effective matching of the solar spectra [48], enhancing the overall process [7] .

For the PEC cell enhancement the heterojunction semiconductors should have compatible CB and VB positions [10, 49], aligning their Fermi levels and producing an electric field that promotes the separations of electron-hole pairs [49].

On the interface between the outer photoanode material and the electrolyte, are formed two distinct surface states due to the asymmetry of the electronic potentials, one below the conduction band and the other above the valence band [50]. The recombination surface

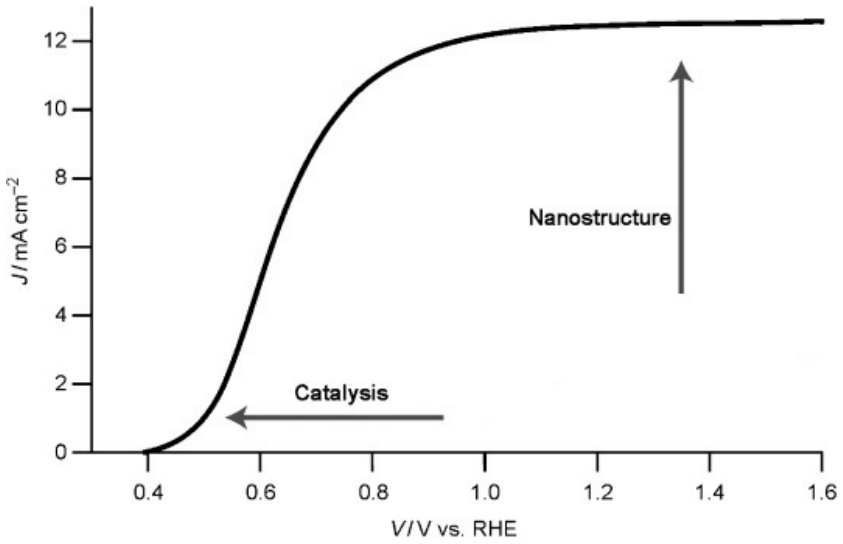


FIGURE 1.12: Maximum theoretical performance for hematite photoanodes [under AM1.5G 100 mW/cm^2 simulated sunlight]. Catalysis address the onset potentials and nanostructuration the saturation current. (Adapted from [28]).

below CB, designated as state (r-SS), on Figure 1.13, is responsible for the recombination phenomenons, while surface state (i-SS) acts on the hole transfer on the interface [50, 51].

Ideally, the photogenerated holes must be transfer via i-SS or directly from the VB, their transfer can also happen through r-SS but causes the recombination of the photogenerated pairs [50, 51]. Surface stats are reported to be related to parasitic losses, charge carrier recombination and trapping [50, 51], but it is possible to adjust their properties through the addition of a different material at the surface [50].

Heterojunctions lead to new properties of the photoanode, in general, strongly determined by the outer element [25]. Commonly, this formation favors the absorption of visible light [10], improve the charge separation [10] and increase the life time of charge carriers [10].

On the interface of the heterojunction, the electron flow between the two semiconductors form an internal electric film, facilitating the charge separation and thereby suppress the electron–hole recombination [10].

Hematite heterojunctions such as Si/Fe_2O_3, TiO_2/Fe_2O_3, WO_3/Fe_2O_3, $MgFe_2O_4/Fe_2O_3$ and $Fe_2O_3/BiVO_4$ are some combinations that have been shown enhanced performances on hydrogen harvesting [10]. In the particular case of Fe_2O_3/TiO_2, the performances were enhanced due to the absorption efficiency by capturing a wider solar spectrum [10]

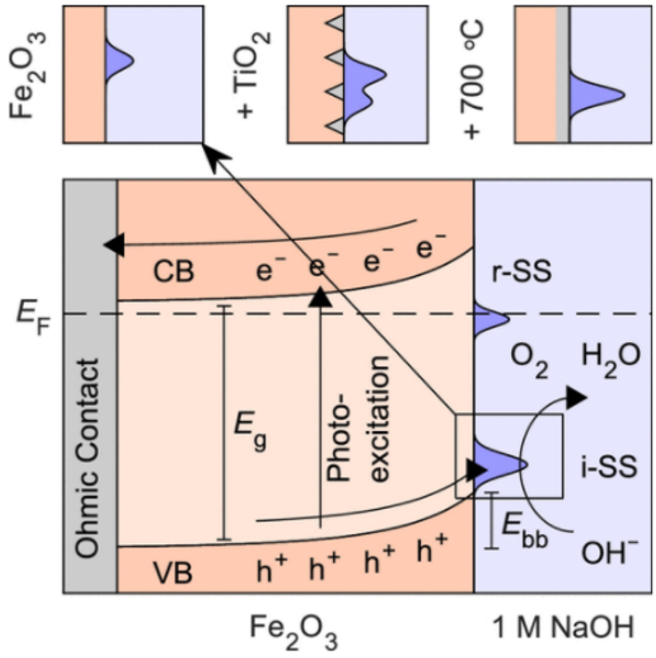


FIGURE 1.13: Schematic of the band structure of the hematite–electrolyte interface, the intermediate surface states (i-SS), the recombination surface states (r-SS), and the oxygen evolution and the charge transfer reactions during the water splitting reaction under alkaline conditions. The i-SS local density of states (LDOS) for the Fe2O3 and Fe2O3/TiO2 samples before and after the post annealing are illustrated at the top (Adapted from [50]).

1.5.5 TiO_2 passive layer

The use of a passivation layer changing the semiconductor surface has recently attracted increasing attention to enhance the photoelectrodes performance, since it improves the charge-separation, the oxygen evolution reaction (OER) kinetics and the hole transportation across the semiconductorelectrolyte interface [33, 52]

Several methods can be used for the application of these types of overlayers, based on chemical solution based methods [52, 53], atomic layer deposition (ALD) [54], among others, however, the use of techniques based on physical vapor deposition (PVD) and controlled vacuum processing allows the optimized preparation of highly homogeneous and crystalline thin films.

Ahmed et al. [52] reported the use of a TiO_2 overlayer at the surface of hematite photoanodes, resulting in the passivation of the surface states and suppressing the surface electron−hole recombination, with a general improvement of the generated photovoltage and the band bending, reaching a photocurrent density of 1.2 mA/cm^2 vs RHE [52].

On the other hand, Jeon et al. [53] also used an ultrathin TiO_2 overlayer of 3.5 nm, which showed to reduce the surface charge recombination, while preserving the integrity

of the hematite electrode, reaching a state-of-the-art photocurrent density of 6 mA/cm^2 (at 1.23 V vs RHE).

1.5.6 Thermal annealing

Thermal annealing consists on submit the material to high temperatures, in a controlled environment, supplying considerable amounts of thermal energy. The supply of thermal energy to the film, results in a reorganization of the structure, where the atoms and molecules tend to position on preferential sites, which leads to higher crystallinity [9, 29], lower crystallographic defects [29] and increases the grain size what therefore reduces the grain boundaries [29], which are potential recombination sites for the photogenerated charge carriers [55].

Depending on the temperatures practiced, the oxide phase will vary, making ideal annealing conditions vary from case to case. After the annealing, a rapid cooling process if preferable once it affects the charge separation efficiency, improving photocurrent values [8].

On hematite, the crystallization starts above 390 ºC and the ideal annealing temperature for complete conversion was reported to occur approximately at 1000 °C [8, 56].

TiO_2 phase transformation through annealing, depends significantly on the synthesis parameters [35]. On air atmosphere, pure bulk anatase starts to transform irreversibly to rutile at approximately 600 ºC [35], however the reported transition temperatures vary in the range 400–1200 °C [35, 39], depending on parameters like particle size and shape, surface area, heating rate or volume of sample [35].

For PEC applications, it is recurrently used fluorine-doped tin oxide (FTO) substrates and when it is exposed through high temperatures, occurs the diffusion of Sn^{4+} ions to the film [8, 22], which leads to a slight structural distortion of hematite unit cell due to the size difference between Sn^{4+} and Fe^{3+} cations [22], causing an increase on the absorption coefficient of hematite [22, 31]. The Sn^{4+} substitution will also increase the electron density and consequently a up shift on the Fermi level, which could improves charge separation [22], however this approach can lead to an uneven distribution of Sn^{4+}, presenting a gradient profile with high concentration near the interface hematite/FTO and relatively poor presence on the top [12].

Despite the improvements after the introducing of Sn dopant thought annealing, in FTO substrates it is necessary to take into account the maximum temperature supported

by each of the substrates (The limitations of the substrates used experimentally are referenced in the next chapter). Extremely high temperatures will degrade the electrical conductivity of FTO substrate [8, 22], deforms the sample and expresses a sharp drop in photocurrent when exposed to the sun.

In recent researches, it was demonstrated that a two-step annealing approach with a second step at 800ºC [7, 8, 31], enhanced the photocurrent densities. It was reported that in those conditions a 20 minute annealing at 800ºC produced the higher photocurrent [7, 8, 29], with a maximum exposure time of 30 minutes to preserve the FTO properties [31].

Trough the experiments of Kim et al. [7], on the annealing at different temperatures of hematite thin films, it was demonstrated by TEM images that an annealing at 800 ºC achieves a single crystalline character without any grain boundaries while at 550 ºC it was visible different crystallized areas, indicating polycrystallinity [7]. On the case of TiO_2 films, atomic force microscopy measurements performed by Bakri et al. [39], showed that higher temperatures of annealing leaded to an increase of roughness due to the increase in the grain size and phase change of the film [39].

1.5.7 Anodization

Anodization can also change a planar film to a more exotic design, increasing the surface area available for reactions [22] and enabling ultra fine features that offers a shorter path for the charge carriers to the electrolyte-electrode interface [22] (Figure 1.14). This technique also allows to address some of the intrinsic limitations of the materials like the visible light absorption, stability under the environment of operation, efficient charge carrier separation and their transport, bandgap and the positions of the conduction and valance band to the required reaction potentials [1], increasing the overall efficiency. Another strategy to enhance the harvesting of light is to design nanostructures that trap the incident light between nanostructures, increasing the amount of light that is harnessed [12].

Anodization process

The anodization process consists in, through the application of a difference of potential between the working electrode (sample) and a counter electrode, both immersed on a appropriated electrolyte, grow oxides and create nanostructures with different morphologies, depending on the anodization conditions. The main parameters that we should take

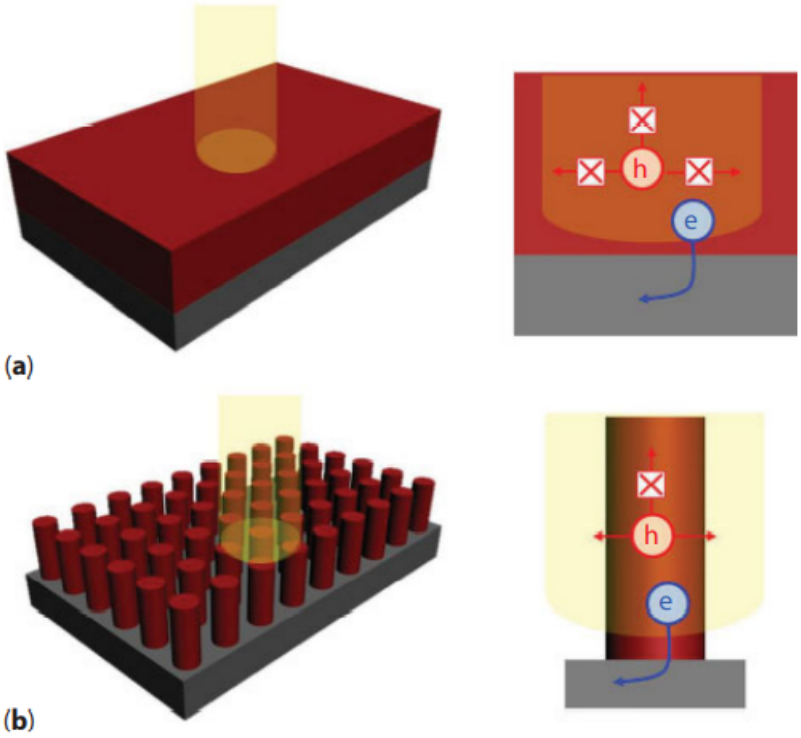


FIGURE 1.14: Schematic illustration of the different diffusion patterns of photoinduced charge carriers between (a) a plain hematite film photoanode and (b) a hematite nanowire array photoanode. Holes trapped in films can hardly diffuse to film surface due to their limited diffusion length (marked with X). Holes generated in a nanowire manage to move to the surface by diffusing horizontally across a small length (Adapted from [12]).

into account are the electrolyte type, time of anodization, potential applied, temperature and the rotations per minute of the solution homogenizer [32].

The anodization can be used to target some intrinsic limitations of the materials [2] such as the bandgap and the levels of conduction and valence bands, light absorption spectra, separation and transport of charge carriers, interfacial charge-transfer kinetics and the stability under the conditions of operation, by generating nanostructures such as nanopores or nanotubes [1, 57]. Although the properties change, this process increases dramatically the ratio of surface area/volume, due to the creation of small features, increasing the active area avaiable for reactions.

This method requires few elementary laboratory materials and can be done at a low-cost, which is very attractive for a large scale, combining with the low-cost of the materials used in this work.

During the anodization process of Fe and Ti, is possible to identify the formation and growth of nanotubes (NT) through the current density curves (Figure 1.15) [58].

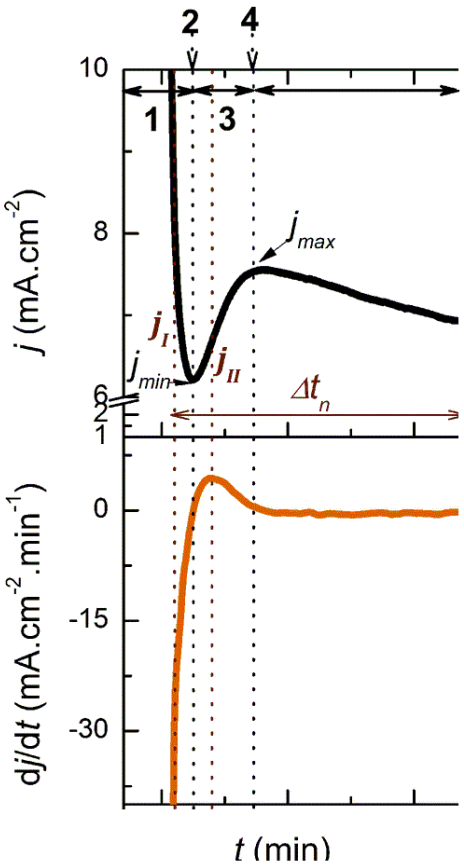


FIGURE 1.15: Transient curves of a typical anodization process and the respective derivate (Adapted from [58])

At the beginning of anodization, the electrical resistance across the counter electrode and the sample to anodize is relatively low, originating high current densities. Due to the oxidation of the anodized material (formation of an oxide layer), the resistance increases, causing a decrease on the current density (Stage 1), until reaching the maximum thickness of oxide layer, which is related with the minimum current, j_{min} (Stage 2). The increase in current density indicates the beginning of pore nucleation (Stage 3), i.e., starting of dissolution of the oxide layer assisted by field-enhanced dissolution and the presence of fluoride ions (F^-). Then the nanopores reorganize and grow in a self-organized process, that culminates at the lowest oxide thickness when it is achieved the j_{max} (Stage 4). Finally, the stabilization of the current density along anodization time indicates the continuous growth of the nanopores/tubes in vertical orientation [58, 59].

1.5.7.1 Thin films anodization

In hematite thin films, the holes available for the oxygen evolution reaction (OER) are the holes that are photogenerated very near the interface between the electrolyte and the electrode, once the diffusion length of the minority charge carriers are very low. Through anodization it's possible to create shorter travelling paths [7], preferentially smaller than the diffusion length (2-4 nm on hematite), which leads to an decrease on the recombination rates, increasing the efficiency [19].

Despite all the optimization of the physical properties offered by the nanostructuring, the change in architecture improves by itself the efficiency, once the surface area is higher, offering more available sites for chemical reactions and reduces the distance needed to the holes reach the reduction sites, decreasing the recombination rates. The nanostructure sizes should also be taken in account, once it highly influences the performance of devices [9].

1.5.8 Alternative approaches

Some alternative approaches for hydrogen production are reported in literature, where Qi et al fabricated photoanodes based on $n-Si/\alpha-Fe_2O_3$ core/shell nanowire arrays, achieving 5.28 mA/cm^2 at 1.23V vs. RHE , with a low photocurrent onset potential of 0.5 V vs RHE [11]. Other alternatives are the three-dimensional nanophotonic structures produced by Qiu et al, where the hematite absorption was highly improved due to the light trapping (Figure 1.16), provided by 3D structures, achieving a photocurrent density of 3.05 mA/cm^2 at 1.23V vs RHE [44]. Yongjing Lin et al. also synthesized highly conductive nanonet structures of $TiSi_2$, giving structural support and an efficient charge collector (Figure 1.11), resulting in 1.6 mA/cm^2 at 1.23V vs RHE [26].

As far as we know, the highest photocurrent density achieved for hematite based photoanodes reported in literature, was 6 mA/cm^2 at 1.23V vs RHE, for nanorod arrays modified by hydrogen treatment, loading a titanium dioxide (TiO2) overlayer and a cobalt phosphate (Co-Pi) co-catalyst, produced by Jeon et al. [53].

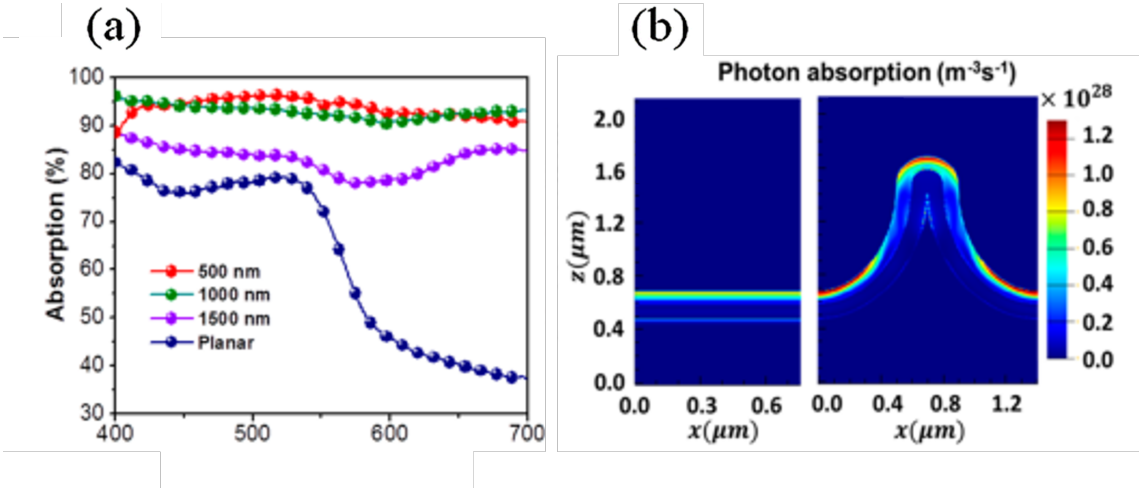


FIGURE 1.16: UV−Vis absorption measurements of ultra thin hematite films coated on regular arrays of 3D conductive nanospikes (a) with different pitches, (b) Cross-sectional photon absorption profile of device on planar (left) and nanospike substrate (right). (Adapted from [44]).

Chapter 2

Experimental Techniques

In this chapter, a brief summary of the experimental methods used to fabricate the semiconductor materials are presented, followed by an overview of the techniques used to characterize the resulting materials. First, two different approaches were used for top-down growth of multilayers of Ti and Fe followed by a thermal annealing to obtain the respective oxides and bottom-up fabrication of nanostructured Fe_2O_3 and TiO_2 by anodization techniques. In the second part the techniques used for their morphological, structural, optical and photoelectrochemical characterization are presented.

2.1 Materials, reagents and sample preparation

2.1.1 Material and reagents

The thin films were grown on glass substrates with fluorine doped tin oxide (FTO) coating on one of the sides. Two types of Transparent conductive oxides (TCO) were used, a 2.2 mm thick glass substrate with a $7\Omega/sq$, named TCO 22-7 [60] and a 1.1 mm thick glass substrate with a $10\Omega/sq$, designated by TCO 10-10 [61].

The chemical reagents used experimentally are listed bellow as well as their purity, chemical formula and supplier company.

Substrate and thin film Cleaning:

C_2H_6O, Ethanol (JMGS, 99%)

KOH, Potassium Hydroxide (Panreac, 85%)

CH_3COCH_3, Acetone (Labsolve, 99.7%)

H_2O_2 Hydrogen peroxide (Sigma Aldrich, 30%)

Anodization electrolyte:

NH_4F Ammonium Fluoride (Alfa Aesar, 98% min)

$C_2H_6O_2$ Ethylene glycol (Acros Organic, 99.81%)

PEC measurements electrolyte:

NaOH Sodium Hydroxide [Chem-Lab, 1 M (1 mol/L)].

2.1.2 Samples preparation

Before deposition, FTO substrates were cleaned based on a sequential cleaning method reported by Francisco et al. [27]. Firstly, the FTO pieces, with the standard format of 1.2 x 2.5 cm^2 were cleaned by a jet of acetone followed by a prolonged and careful rubbed with soapy water. After previous cleaning, FTO were sequentially placed in an ultrasonic bath of soapy water for 10 minutes, followed by 10 minutes in ethanol 96%. The procedure was repeat, following to 20 minutes in a solution of 2M KOH in ethanol 70 %, finishing with a ultrasonic bath step of 10 minutes in a bath of deionized water.

Soapy water is used to remove grease and dirt, while ethanol removes the detergent present on soapy water and the organic waste. Between cleaning steps, it is important to clean the substrates with a jet of deionized water, mainly after the use of KOH solution.

There are also some details that must be taken into account during the cleaning process. For example, during the KOH cleaning step, glass material should not be used due to possible corrosion caused by KOH since it is a strong base. Also it is not recommended their use on FTO for more than 20 minutes without deeper studies. The prolonged use on the substrate can cause undesirable effects, compromising the FTO performance.

After cleaning, the substrates were placed on top of laboratory paper in a vertical position, supported by a cleaned and dried glass material, covered by a dome of glass, also cleaned and dry, in order to avoid particle contamination from air during the drying process.

Considering the photoelectrochemical performance measurements, a small area of the FTO (1.2 X 0.75 cm^2) was covered with Kapton tape in order to keep it intact and serve as electrical contact during the measurements.

2.2 Synthesis methods

Two different approaches were used to obtain hematite photoanodes: thin films obtained by ion beam deposition and spin coating and nanostructures obtained by electrochemical anodization.

2.2.1 Thin films deposition

2.2.1.1 Ion Beam Deposition (IBD)

Ion beam deposition (IBD) is a physical process capable of depositing highly homogeneous thin films. The main advantages of this method are the possibility to operate with any material as target and substrate [62] and the possibility to deposit alternated layers of different materials without breaking the deposition environment.

To reduce the potential recombination spots of the photoelectrode, a carefully management of all the fabrication stages is necessary. The deposition should produce homogeneous and high crystalline films on a controlled atmosphere to reduce the possibility of adsorbing ions. This would reduce the defects due to distortion of the lattice.

IBD deposition process operates on an inert gas atmosphere, relying on an ion gun to produce the ion beam, which is accelerated through the chamber, focusing on the target, removing their atoms and depositing them on the substrate (Figure 2.1). Each produced ion, have the same energy [62] and the beam is formed by superposition of the ion trajectories passing through the individual holes of the multi-aperture grid system [63], creating an energetic uniform collimated beam, leading to more homogeneous films.

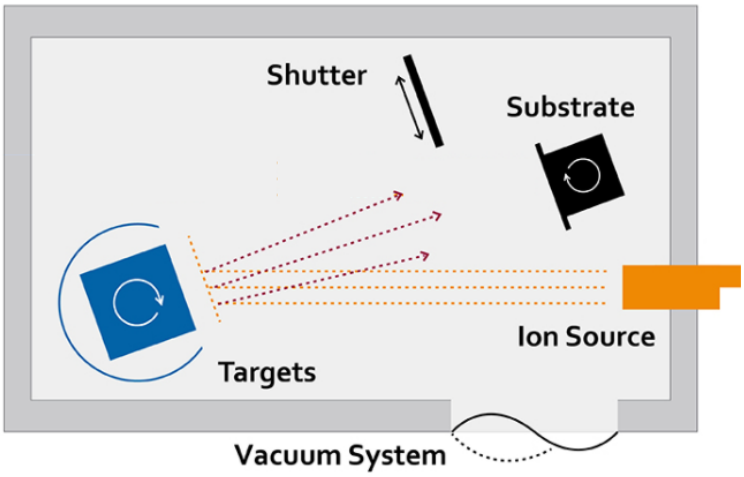


FIGURE 2.1: Schematic illustration of Ion Beam Deposition system (Adapted from [64])

Experimental operation

To deposit iron and titanium thin films, an IBD (Commonwealth Scientific Corporation) system on a ISO-7 clean room unit (CEMUUP-MNTEC) (Figure 2.2) was used.

The primary vacuum was achieved by a rotary mechanical pump, switching to a cryogenic pump in order to obtain high vacuum (in range of 10^{-8} Torr). Under operation the chamber was filled with Argon (inert gas) at a flow of approximately 7 sccm, maintaining the pressure work.

Prior to deposition, a target cleaning was performed by focusing the ion beam on the target with the shutter closed, eliminating possible contamination on the surface of the target.

To improve the uniformity of the deposited films, the substrate holder had a rotational axis capable of 30 rpm. The target holder had four target spots, allowing for an alternated deposition of different materials, without having to open the chamber and break the deposition conditions.

The parameters at which the IBD was operated are listed on Table 2.1, and for these conditions it is recommended that the working time does not exceed one hour. If longer time intervals are required, an one hour pause must be done to cool the system, not compromising the equipment components and the uniformity of the deposited film.

Conditions	Cathode	Discharge	Beam	Accelerator
Current (mA)	6.7	2.00	10.5	1.2
Voltage (V)	5.7	38.2	993	148.5

TABLE 2.1: Standard conditions of IBD operation during the deposition

2.2.1.2 Spin coating deposition

Spin coating is a simple and low-cost deposition procedure to deposit uniform thin films.

Firstly, the material to be deposited was dripped on the center of the substrate, that is fixed on the substrate holder thought vacuum pump, then the substrate holder starts to spin and the material is spreaded uniformly on the substrate due to centrifugal force. The desired thin film thickness depends on the viscosity of the material, the rotation velocity, the initial acceleration and on the time of operations

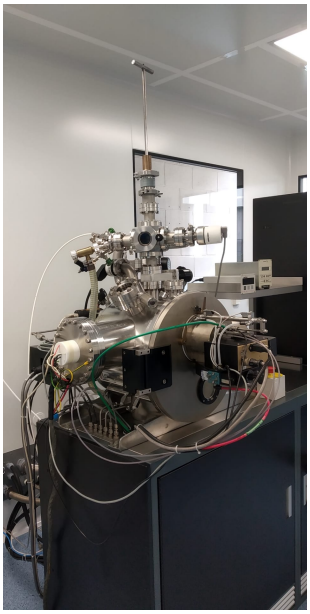


FIGURE 2.2: Ion Beam Deposition system used to deposit thin films (CEMUUP-MNTEC).

Experimental Operation

This technique was used to deposit thin layers of titanium with a thickness of 6 nm [65]. A 10 mM titanium diisopropoxide bis(acetylacetante) solution in 75% isopropanol was used to be dropped on the FTO substrate at 1500 rotations per minute, during 30 seconds. Due to the fluidity of the solution, a silicone mask was placed between the substrate and the vacuum apertures, preventing the solution to enter into the vacuum system and damage it.

After the deposition, the thin films were heated at 250 ºC for 30 minutes to eliminate organic solution components [65].

2.2.2 Electrochemical anodization

The metallic thin films obtained by IBD deposition were anodized in an electrochemical cell composed by a Pt mesh (counter electrode) at the top of the cell and the sample to be anodized is located at the bottom in electrical contact with a Cu plate, with an exposing area for anodization of 1 cm^2. The anodization process was performed at room temperature and stirred at 70 rpm.

The anodization potential was constant over the time and the current density curves were acquired and recorded thought a a source-meter controlled by a Labview program.

To study the effect of voltage and anodization time in thin films anodization, three different potentials of 30, 40 and 60 V were applied, with anodization times ranging from 30 seconds up to 5 minutes.

The anodization electrolyte was composed by 0,379 g of NH_4F; 97 mL of ethylene glycol and 3 mL of desionized H_2O.

2.2.3 Annealing conditions

Thermal annealing treatment allows the restructuring of the lattice, eliminating defects and promoting the crystallinity. On FTO substrates it is also promoted the diffusion of Sn^{4+} to the films deposited into the substrate [10, 12], enhancing the photocurrent outputs of the photoanodes.

However, FTO substrates have a temperature threshold from which they start to deform, affecting their crystalline structure and compromising significantly the efficiency of the photoanode [8]. Since hematite crystallization starts above 390ºC, to avoid the deformation of the substrates the maximum temperatures performed in this work was 600ºC for TCO 22-7 substrate [60], while TCO 10-10 [61] was submitted to 800ºC, as it only presents loss of efficiency at temperatures above that value [8].

2.3 Characterization Techniques

2.3.1 Morphological Characterization

2.3.1.1 Scanning electron microscopy

Scanning electron microscopy (SEM) is a highly versatile instrument that allows the morphological characterisation of the sample as well as their chemical composition [66–69].

The resolution of a microscope is described by the minimum distance between structures in which the image is represented by distinct objects [67, 68], which highly depends on the source wavelength. Considering that the electrons wavelength is related to their kinetic energy, and their energy can be increased depending on the accelerating voltage [67], SEM can produce high resolution images by controlling the electron momentum, where smaller wavelengths are obtained by higher energy electrons which suffer from higher acceleration potentials [67], resulting in high quality images.

SEM relies on apertures, magnetic and/or electrostatic lenses, and electromagnetic coils to control the electron beam diameter and their focus spot, allowing the characterization of a series of discrete locations on the sample [69], as can be seen on Figure 2.3.

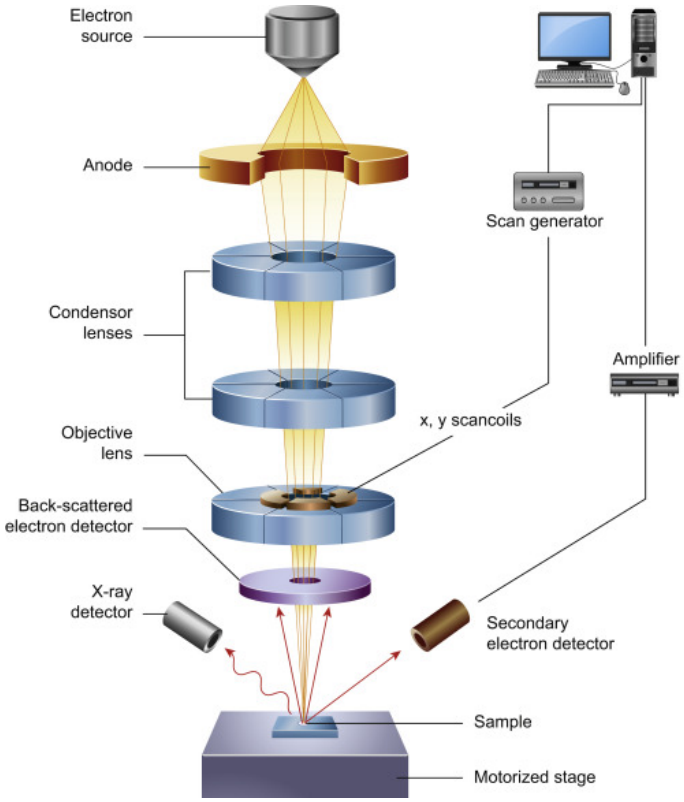


FIGURE 2.3: Schematic diagram of the core components of an Scanning Electron Microscope. (Adapted from [67])

The image formation results from the radiation acquired by detectors which in turn is a consequence of the interactions between the electron beam and the sample. This implies that the measurements should be done in vacuum (preferably at least 10^{-6} *Torr*) [67] in order to avoid interactions between electrons and undesired matter [67].

The electron beam-sample interactions can be distinguished in two categories, elastic or inelastic interactions [68]. On elastic scattering, the energy losses by collisions are negligible (same wavelength) but a change in the direction of the scattered electrons can occur [67, 68]. When an electron is elastically scattered through an angle of more than 90 degrees, it is called a back-scattered electron (BSE) [68], which gives information about the sample composition, topography and crystallography [69].

In contrast, electrons on inelastic scattering transfer energy to the atom of the sample through several types of interactions [67, 69], producing surface images of the sample. Secondary electrons (SE) result from the ejection of weakly bound outer-shell atomic or

valence electrons [69], when the ejection occurs on tightly bound inner shell atomic electrons, results in the emitted of characteristic X-rays [67, 69]. Deceleration of electrons due the influence of near atoms, emit Bremstrahlung x-rays, on a continuous range of energies [67] (Figure 2.4).

Other signal sources for the characterization of the samples, are the auger electrons that can release the excess energy when an outer shell electron decay to fill a vacancy leaved by an inner shell electron previously ionized by the electron beam [67]. Auger effect produces low energy electrons that are only emitted near the surface, with characteristic energies, providing chemical information about the sample [67] (Figure 2.5). The recombination of the excited electron–hole pairs due to the incidence of primary electrons, leads to light emission in a mechanism named Cathodoluminescence [67, 68].

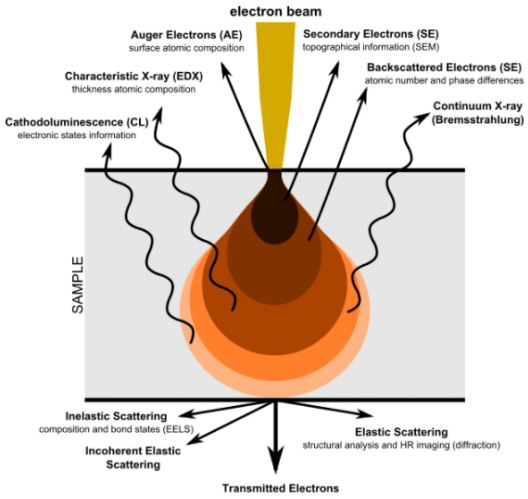


FIGURE 2.4: Different kinds of radiation generated by the electron beam interaction with sample on scanning electron microscopy (Adapted from [70])

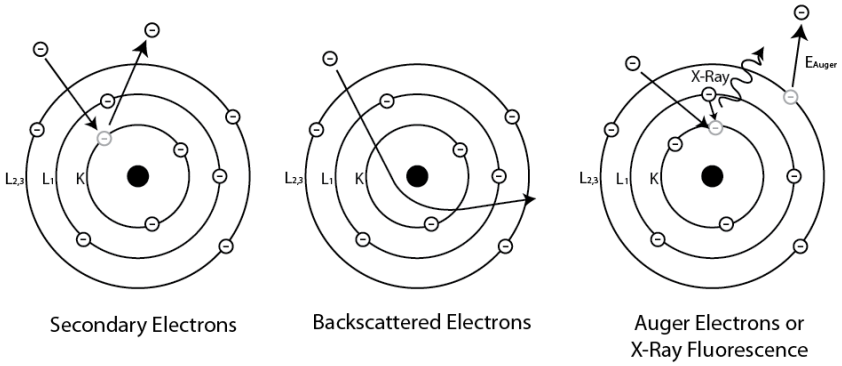


FIGURE 2.5: Schematic interactions of secondary, backscattered and Auger electrons with the sample atoms. (Adapted from [71]).

Due to the nature of the samples measured (semiconductors), a carbon felt was used

to establish an electric discharge path, reducing the possibility of charge accumulation on surface that would interact with the electron beam, compromising the measurements.

In this work, the chemical and morphological characterization through SEM was performed using a FEI Quanta 400 FEG Field Emission; at CEMUP, University of Porto.

2.3.1.2 Energy Dispersive X-ray Spectroscopy

Energy Dispersive X-ray Spectroscopy (EDS) is a technique capable of performing a chemical analysis of the samples [72], generally associated to SEM systems [66, 72].

The ionization of an inner shell electron of the sample by an electron beam, results in an emission of a Auger electron or characteristic x-ray radiation [66, 67, 69] (see previous section). Since all elements have their own unique x-ray emission spectrum [72], as it depends on characteristic atomic transitions of discrete energy levels, it is possible to differentiate and measure the concentration of each element on the sample [72].

2.3.1.3 Stylus profilometry

Stylus profilometry is a morphological characterization technique that relies on a physical probe that moves with constant velocity along the surface.

The stylus is loaded in direct contact with the surface and during the scanning, acquires morphological data such as the roughness and the step heights of the sample.

In this work was used a Dektak XT, Bruker profilometer (Figure 2.6) in order to determine the thickness of the deposited thin films by IBD. All the measurements were performed in a clean room environment (CEMUP - MNTEC)

To obtain the information on the thickness of the thin films, a piece of silicon wafer was marked with several lines of a chemically removable compound and placed on the IBD chamber, during the deposition. After the thin film deposition, the marked lines and the material deposited on the top, were chemically removed by sequential ultrasonic baths of acetone, ethanol and deionized water, exposing the silicon wafer surface.

After this procedure, the profilometer was able to measure the step height between the regions with and without thin film, determining the film thickness.

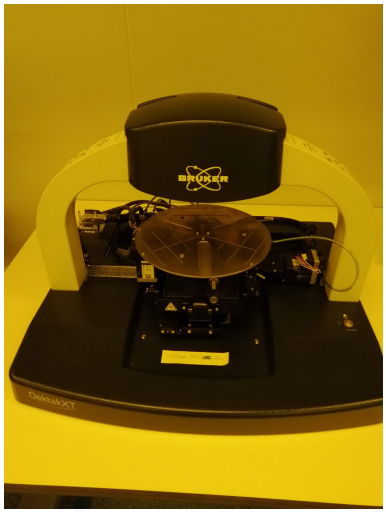


FIGURE 2.6: Profilometer system used to obtain the thickness of thin films (CEMUUP-MNTEC).

2.3.2 Structural Characterization

2.3.2.1 X-ray diffraction

X-ray diffraction is an essential tool to rigorously prove relevant properties like crystal structure, preferential directions of growing and crystallinity. The x-ray diffraction technique consists in the passage of x-rays through the sample, interacting with the electrons in the atoms of the sample, resulting in the scattering of the radiation [59].

Once the wavelength of x-rays is in the same magnitude as the lattice parameters of crystalline materials, the interference of the scattered waves will occur, forming a diffraction patters with constructive interference for in phase signals.

The positive interference occurs at characteristic angles, related to the spaces between the atomic planes, which is expressed on Bragg's law [73] (represented on Equation 2.1 and Figure 2.7).

$$n\lambda = 2d_{hkl}sin(\theta) \tag{2.1}$$

Where the wavelength (λ) is related to the atomic spacing (d_{hkl}) and the diffraction angle (θ) which is formed by the vector of incident and scattered waves.

Thought the diffraction pattern, is also possible to estimate the crystal grain size according to the Scherrer equation [9, 39] (Equation 2.2):

$$D = \frac{K\lambda}{\beta cos(\theta)} \tag{2.2}$$

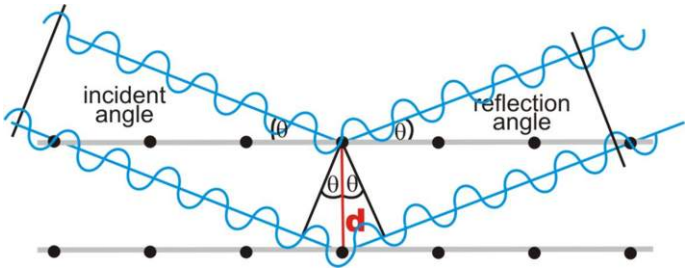


FIGURE 2.7: Representation of Bragg's law. (Adapted from [74])

where K is a dimensionless constant, 2θ is the diffraction angle, λ is the wavelength of the X-ray radiation, and β is the full width at half-maximum (FWHM) of the diffraction peak [9]. The equation expresses an inversely related relationship between the grain size and FWHM, which to a narrow peak corresponds a larger crystallite size.

In this work, the XRD measurements were performed using a SmartLab Rigaku diffractometer (Figure 2.8), relying on a cooper Cu K_α radiation with $\lambda = 1.540593$ and anode x-ray tube at 200mA and 45kV.



FIGURE 2.8: Rigaku XRD system used in the obtainment of thin films XRD spectra.

Due to the low thickness of the samples, ranging from 60 to 200nm, the FTO substrate presented a high contribution for the intensity of the XRD spectra, in order to reduce the signal from the substrate, the measurements relied on a parallel beam (PB) configuration to perform grazing angle X-ray diffraction (GAXRD).

On measurements performed with omega (ω) angle lower than 0.4 degrees, the produced spectrum was heavily influenced by noise. Increasing ω , the x-rays would interact more with the FTO, increasing their contribution for the spectrum, which lead to the fixation of the omega (ω) angle at a constant value of 0.4 degrees for all the performed measurements, once it showed a better ratio between the sample and substrate contributions.

2.3.3 Photoelectrochemical characterization

2.3.3.1 Photocurrent density vs Voltage curves

The photocurrent values are proportional to the number of charge carriers photo-exited that are produced by solar light and participate in the oxidation and reduction reactions of water, which are directly related with the rates of hydrogen produced [7].

The high sensitivity of the photoanode material to the spectral distribution of the illumination source can introduce bias on the data [30]. To mitigate the problem, the photo-currents should be compared with the same monochromatic incident photons at an electrode potential given relative to the reversible hydrogen electrode (RHE) [30]. If not possible, it's very important to specify the spectrum of the incident light as well as their intensity.

The measurements were performed under dark and 1 sun simulated sunlight (100 mW/cm^2) [75], calibrated with an c-Si photo-diode, with a 150 W Xe lamp (Oriel, Newport). A cappuccino PEC cell with an illuminated surface area of 0.528 cm^2 was used. The measurements resorted in 3 electrode configurations, where the photoanode acted like working electrode against a platinum wire (Alfa Aesar, 99.9 % counter electrode and a Ag/AgCl/saturated KCl (Metrohm, Switzerland) reference electrode), submersed in 1.0 M NaOH electrolyte solution.

To convert the measured potential vs Ag/AgCl electrode to the reversible hydrogen electrode (RHE), was applied the Nernst equation [42, 66]:

$$E_{RHE} = E_{Ag/AgCl} + 0.059pH + E^0_{Ag/AgCl} \tag{2.3}$$

Where $E^0_{Ag/AgCl} = 0.1976V$ at 25 ºC and $E_{Ag/AgCl}$ is the potential measured experimentally against the counter electrode.

For the j-V data acquisition was performed on Thales software in paired to a potentiostat attached to the photoelectrochemical cell, a Zennium (Zahner Elektrik, Germany)

workstation (Figure 2.9). The scan rate was kep at 10 mV/s in a potential range between $0.6 - 1.8\ V_{RHE}$.

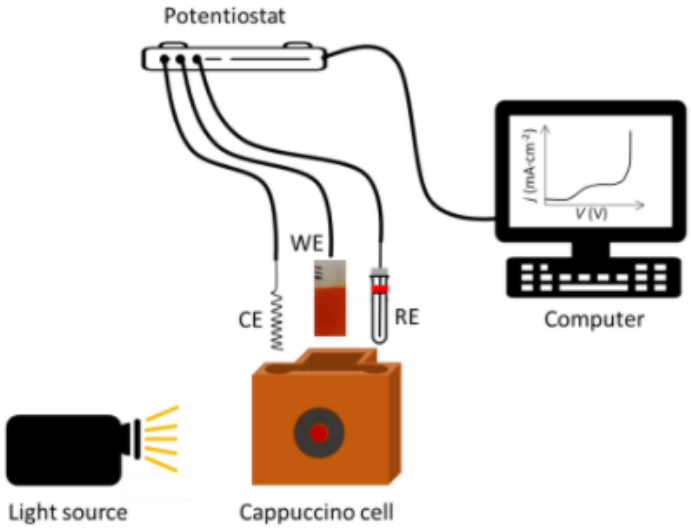


FIGURE 2.9: Cappucino cell with three electrode configuration for j-V curve measurements (Adapted from [66])

2.3.4 Optical absorption

The interaction between electromagnetic radiation and a material determines their optical properties [76].

The characterization of reflective and transmitted phenomenons of the samples was obtained through UV-Vis spectrophotometry, measuring the light reflection efficiency (reflectance) and the light transmission efficiency (transmittance) on the range of 200 to 700 nm.

The light absorption efficiency (absorbance) was determined indirectly by the subtraction of the other two components as indicated in the next equation [75].

$$Absorbance = 100 - Transmittance - Reflectance \tag{2.4}$$

The data was obtained using an UV-Vis-NIR spectrophotometer (Shimadzu Scientific Instruments Inc. model UV-3600, Kyoto).

On the measurements of reflectance, a $BaSO_4$ tablet was used as reference for a 100% reflective surface. The substrate contributions were subtracted in all the measurements (reflectance and transmittance).

Chapter 3

The role of thermal annealing on multilayered hematite and titanium dioxide thin films

In this chapter, it is described the synthesis of thin films based on hematite and titanium dioxide double layers configurations, deposited by ion beam deposition. The influence of the annealing conditions on the the structural, optic, morphological and photoelectrochemical behaviour was investigated as well as the influence of Ti layer on the performance of hematite photoanodes.

3.1 Thin films deposition

Before the deposition, the FTO substrates were cleaned and dried as described in the experimental section. Then the substrates were aligned and placed on the center of the IBD sample holder and fixed with kapton tape, since the sample holder is turned upside down during the deposition.

At the sample bottom the tape only contacts with the glass (without reaching the conductive layer of FTO) and at the top it overlaps the FTO, approximately for one centimeter due to the need of an area without thin film, to behave as a conductive contact during j-V measurements.

To ensure homogeneity of the deposition, the samples were placed as close and central as possible, and with a maximum of four samples per deposition, as represented on the Figure 3.1.

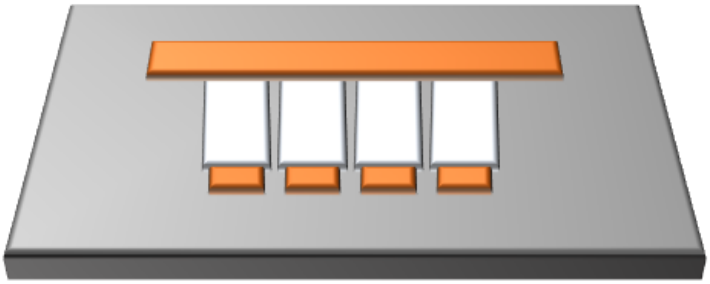


FIGURE 3.1: Scheme of the substrates (white) centered in the sample holder, and fixed with kapton tape (orange) at the bottom and top.

After placing the substrates on the IBD chamber, the chamber went to high vacuum pressures and then it was filled with Argon, achieving a constant pressure, as described in the previous chapter.

The calibration was performed by the deposition of several samples with different deposition times, and their thickness was obtained by multiple profilometer measurements. We obtained a growth rate of $0.44 \mathring{A}/s$ for iron and $0.46 \mathring{A}/s$ for titanium.

The depositions led to samples that were very mirror-like and had a metallic appearance as shown in Figure 3.2 for a Fe/Ti film with a thickness of 150 nm and 50 nm respectively.

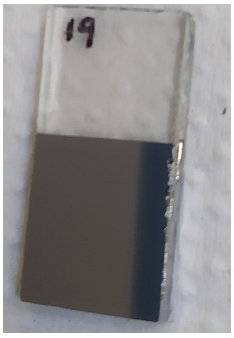


FIGURE 3.2: Thin film of Fe 150 nm/Ti 50 nm after deposition on FTO substrate

Through SEM images, it was possible to confirm the homogeneity of the thin film deposited by IBD (Figure 3.3 b) as well as their morphology. A single element present a similar morphology of the FTO substrate as shown in Figure 3.3.

In order to study the influence of Ti on Fe thin films, it was deposited several thin films with a different positioning for the *Ti* layer (top or bottom of Fe layer). The thickness of the Ti layers deposited were 5 and 50 nm for a Fe thin film of 150 nm.

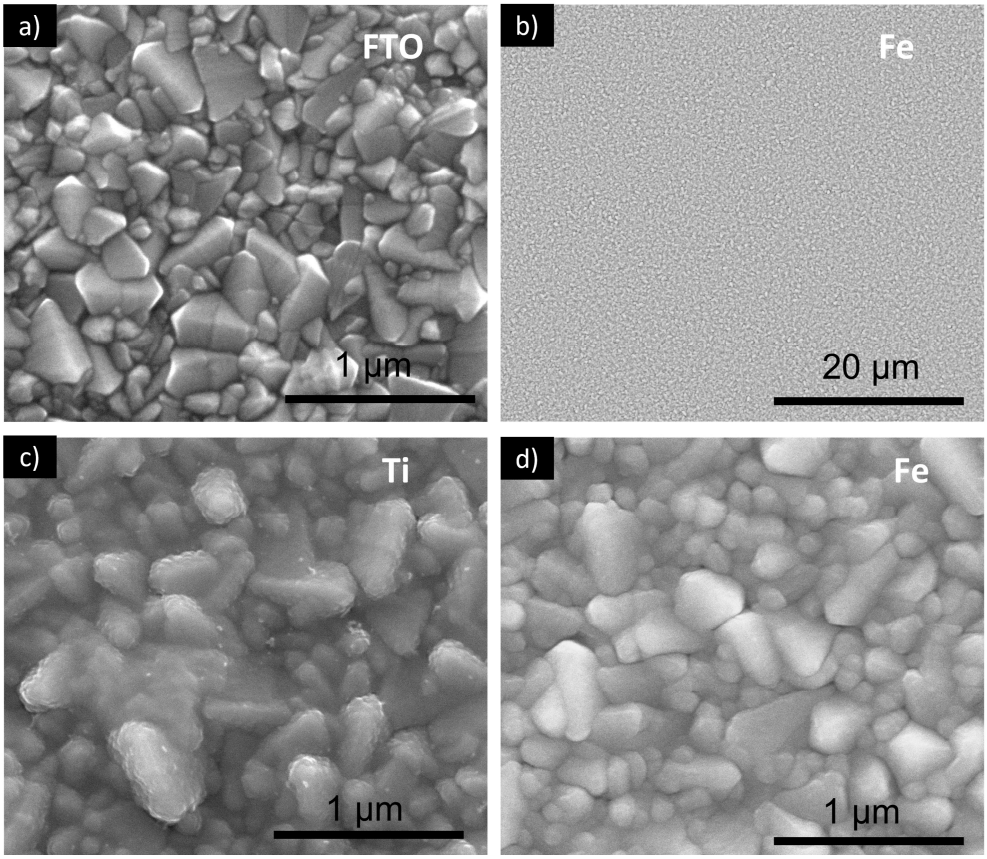


FIGURE 3.3: SEM images of (a) FTO substrate; (b, d) deposited thin films of Fe with a thickness of 150 nm (c) Ti with a thickness of 350 nm.

Double-layers heterojunctions of Fe and Ti kept the homogeneity of the thin film (Figure 3.4 (d)). For a Ti thickness of 5nm, it leaded to a rounding on the sharper areas of the FTO, regardless of the titanium position (Figure 3.4 (b, c)).

The increase on the titanium thickness re-shaped the FTO sharped morphology into an uniform and rounded one (Figure 3.4 (e, f)). The morphology transformation promoted by the junction of iron and titanium does not depend on which material is in contact with the FTO but in the interaction of elements, producing grains with a spherical morphology with an average radius of $0,195 \pm 0,021\ \mu m$ for Ti at the top and $0,189 \pm 0,023\ \mu m$ for Fe at the top.

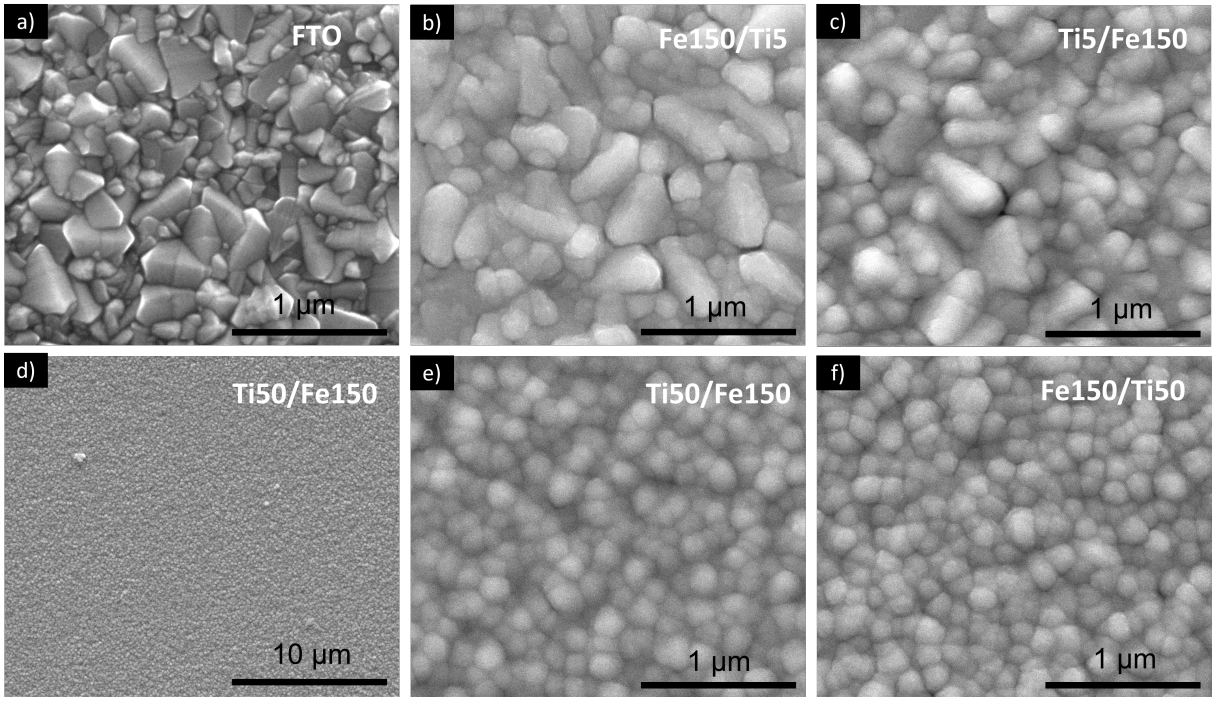


FIGURE 3.4: SEM images of (a) FTO substrate; and deposited thin films of (b) Fe 150 nm/Ti 5 nm; (c) Ti 5 nm/Fe 150 nm; (d, f) Ti 50 nm/Fe 150 nm; (e) Fe 150 nm/Ti 50 nm.

3.2 Influence of annealing conditions

3.2.1 One step annealing

By providing thermal energy to the thin films, on an air atmosphere, occurs their transformation into an oxidized form (Figure 3.5) . Taking into account the conversion temperature of Fe into $\alpha - Fe_2O_3$ ($\approx$ 390C), the maximum temperature supported by FTO of 800 ºC and previous literature reports [8, 50, 66], it was chosen the following annealing temperatures (table 3.1):

Annealing type	Annealing temperature (ºC)
A	550
B	600

TABLE 3.1: Annealing conditions applied to the Ti and Fe thin films in order to obtain enhanced oxide forms.

In both cases the heating rate used was 1 ºC/min until the reaching of the desired temperature, remaining two hours at the annealing temperature and then it cooled down to room temperature at a rate of 8 ºC/min.

To study the influence of annealing conditions, parameters such time, heating and cooling rates, annealing environment were kept constant while the maximum temperature varied. The study was performed using FTO 22-7 substrates [61] with deposition of Fe thin films (150 nm) and compositions of Ti (5 nm) and Fe (150 nm).

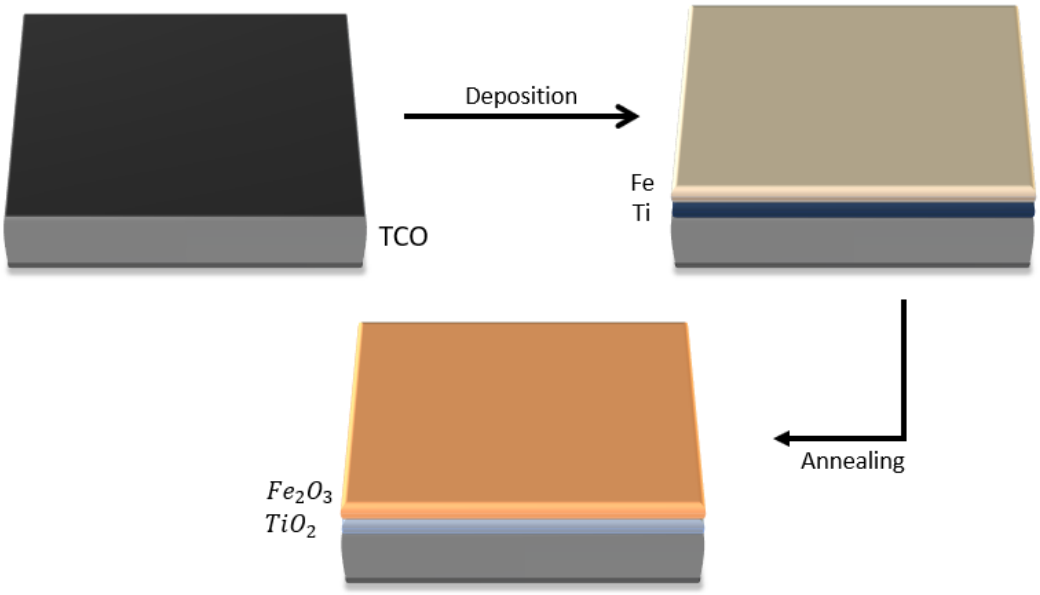


FIGURE 3.5: Transformation stages to produce double layer thin films of hematite and titanium dioxide.

3.2.1.1 Morphological characterization

Regardless of the annealing, it was possible to note at naked eye, a color change in the deposited thin films. On Fe thin films, the metallic aspect turned into a transparent smooth orange, for samples with Ti deposited at bottom of Fe, the thin film assumed a slightly translucent orange color and a more opaque film were obtained when Ti was on top of the Fe layer (Figure 3.6).

Thought SEM analyses, it was possible to compare and identify, at a microscopic level, some of the morphological changes in the thin films after the annealing treatment. After annealing, the Fe (150 nm) thin films developed ribbon shape features. The addition of a 5 nm Ti layer at the bottom of Fe thin film did not present any significant changes on the surface morphology, however for 5 nm Ti layers at the top of Fe thin films, it was developed a coat cover on the surface of the film, which is responsible for the grey color and also for the decrease in length and number of the ribbon shape features (Figure 3.7).

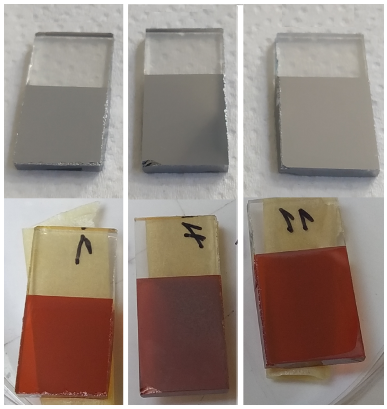


FIGURE 3.6: Samples pre (top) and post annealed (bottom) of 550ºC during 2 hours. Samples composed by Ti(5 nm)/Fe(150 nm), marked as 1 (left); Fe(150 nm)/Ti(5 nm), marked as 7 (center); Fe(150 nm) marked as 11 (right).

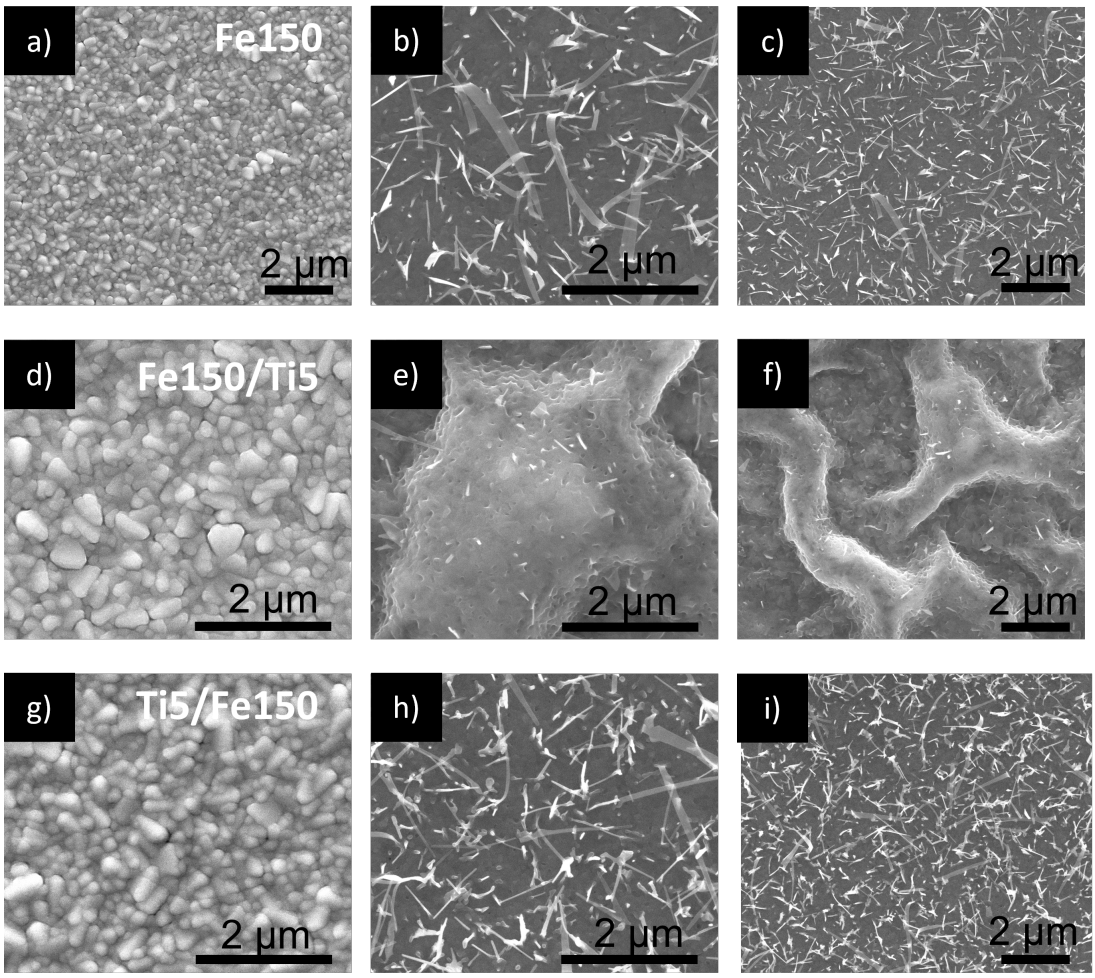


FIGURE 3.7: SEM image of a (a) Fe150nm thin film before annealing; (b, c) Fe150nm thin film after annealing; (d) Fe150nm/Ti5nm thin film before annealing; (e, f) Fe150nm/Ti5nm thin film after annealing; (g) Ti5nm/Fe150nm thin film before annealing; (h, i) Ti5nm/Fe150nm thin film after annealing. The annealings were all performed at 550ºC (Conditions associated with annealing A, Table 3.1)

The ribbon shape features phenomenon was proven to be due the Fe oxide presence, once thought the SEM analyses resorting on the back-scattered electrons, the resultant image, produced a smooth contrast (Figure 3.8), not revealing the presence of other elements besides the ones that are on the thin film surface.

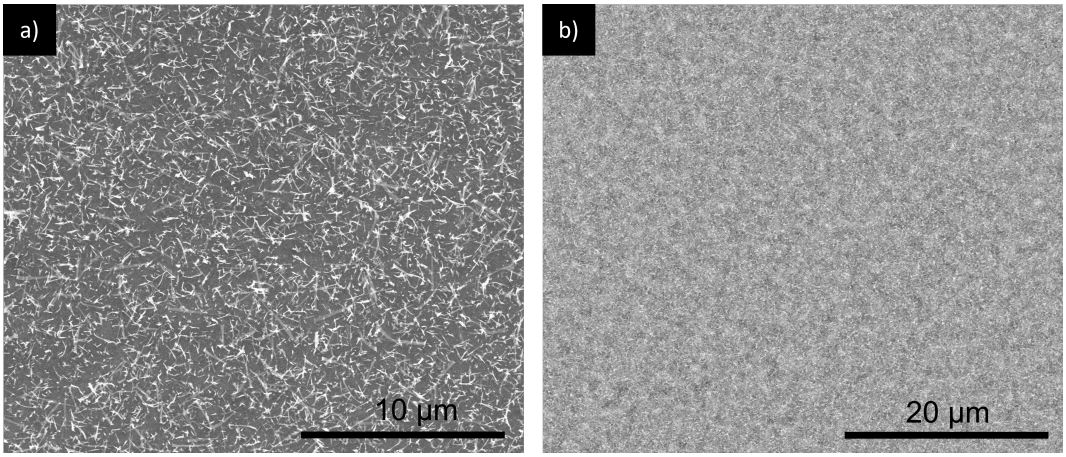


FIGURE 3.8: SEM image of a thin film of Ti5nm/Fe150nm produced by (a) Secondary electrons (b) Back-scattered electrons.

3.2.1.2 Structural analysis

From the XRD spectra (Figure 3.9), it was determined the crystalline phases originated by the annealing (in air atmosphere) of thin films with layers of Fe and Ti. Resorting on a parallel beam (PB) configuration with a grazing incident omega (ω) angle fixed at 0.4 degrees, it was possible to reduce significantly the FTO contribution [32], focusing on the interaction of the x-rays with the deposited material.

The XRD data revealed the presence of hematite crystallographic phase ($\alpha - Fe_2O_3$) with preferential peak growth orientation at the planes (104) and (110), showing also smaller peaks such as (012), (113), (024), (116), (214) and (300). It was also possible to identify some FTO contributions to the spectra (that were tagged with * in Figure 3.9). There was not possible to detect any peaks of Ti due to the low thickness of the deposited material.

The addition of a Ti layer bellow the Fe film presented a change on the preferential growth peak of hematite (Table 3.2). Thin films of Fe deposited through IBD and annealed at low temperatures, revealed a (104) hematite preferential growth peak, however, when Fe grows at the top of a Ti layers instead of the FTO substrate, the (110) peak assume the preferential direction of growth for hematite.

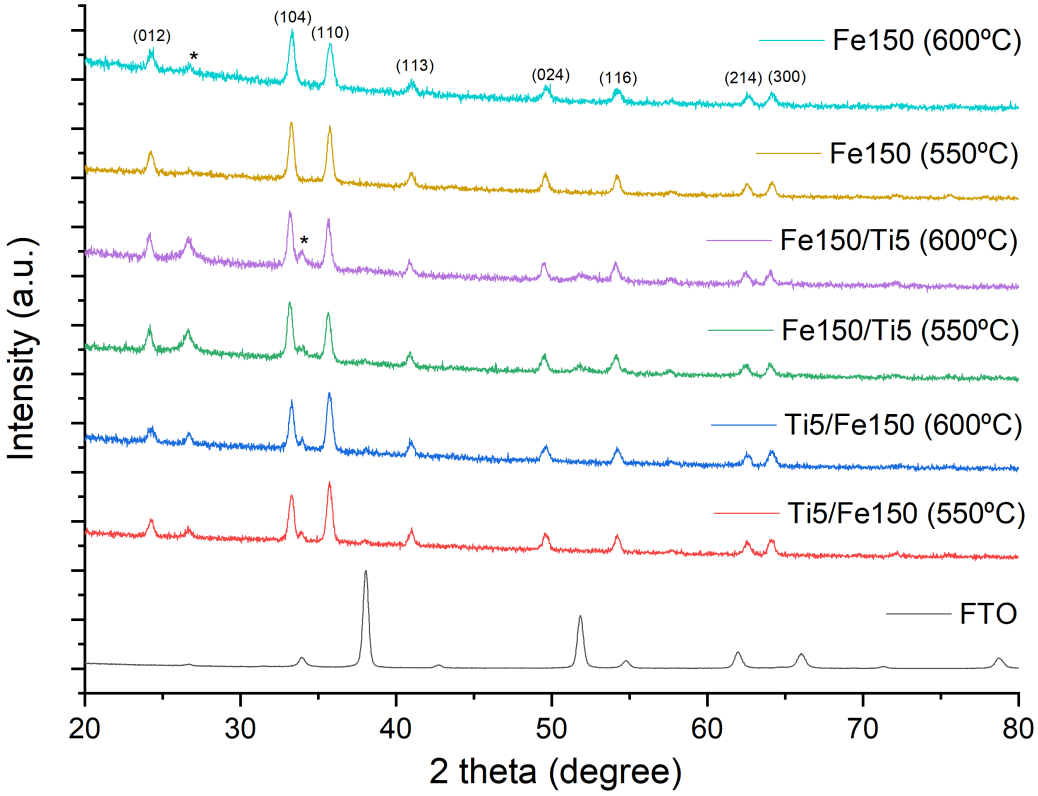


FIGURE 3.9: XRD spectra of thin films composed by $\alpha - Fe_2O_3$ and TiO_2, annealed at the temperatures of 550ºC and 600ºC. The peaks marked represent hematite and * symbol indicates FTO peak contributions.

The difference on the performed annealing temperature, did not produced any significant changes on the XRD spectra for thin films with the same composition, where the peak position and the ratio between the relative intensities kept similar values in both situations (Figure 3.10).

Composition	2θ (104) Peak	2θ (110) Peak	I (104)/I (110)
Fe150 (550ºC)	33.26	35.74	1.04
Fe150/Ti5 (550ºC)	33.14	35.66	1.11
Ti5/Fe150 (550ºC)	33.30	35.74	0.87
Fe150 (600ºC)	33.32	35.74	1.18
Fe150/Ti5 (600ºC)	33.16	35.62	1.09
Ti5/Fe150 (600ºC)	33.30	35.70	0.92

TABLE 3.2: Position (2θ) and relative intensity of the peaks (110) and (104) on hematite when combined with a titanium dioxide layer.

Thought the Scherrer equation (Equation 2.2) it was possible to estimate the the crystallite size, depending on the wavelength of the x-rays, the diffraction angle and the full

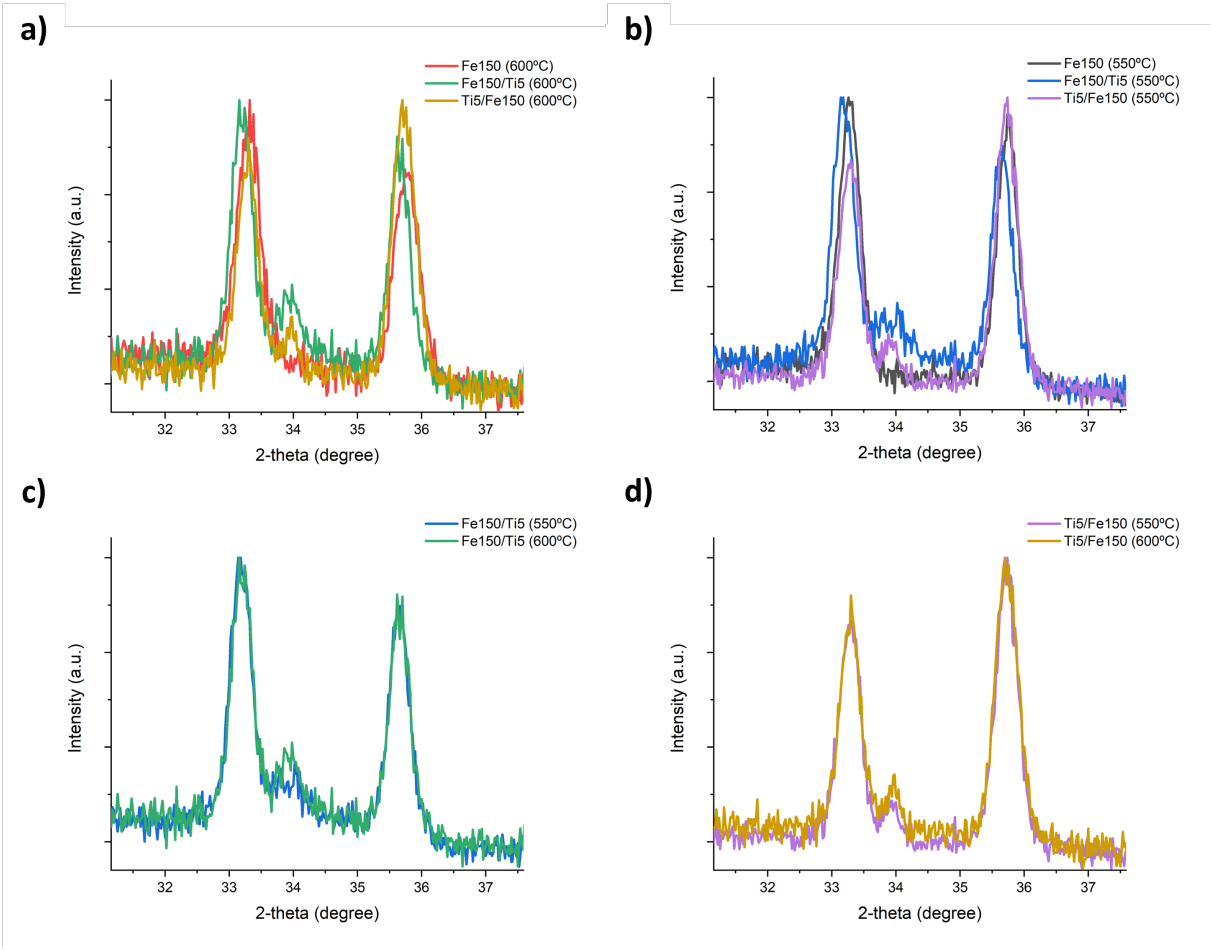


FIGURE 3.10: XRD spectra of hematite and titanium dioxide thin films, evidencing the influence of TiO_2 layer on peak intensity and their positioning. Comparison between the different compositions at a) 600 ºC ; b) 550 ºC; Comparison at different annealing temperatures at c) Fe150/Ti5 compositions; d) Ti5/Fe150 compositions.

width at half-maximum (FWHM). Applying a Pseudo-Voigt fitting to the presented major peaks (104) and (110), it was possible to determine rigorously their FWHM (it was used origin software to fit and calculate the parameters). Crystallite size estimation, presented in Table 3.3, was obtained by averaging the values resulting from the application of Scherrer's law to the two hematite main peaks. The temperature increase from 550ºC to 600ºC does not seems to have a direct impact on the crystallite size, and the difference on the values for each composition are in range of standard deviation.

Composition	Crystallite size (nm)
Fe150 (550ºC)	26.23 ± 1.51
Fe150/Ti5 (550ºC)	26.01 ± 1.36
Ti5/Fe150 (550ºC)	25.22 ± 1.29
Fe150 (600ºC)	22.76 ± 1.54
Fe150/Ti5 (600ºC)	26.22 ± 1.41
Ti5/Fe150 (600ºC)	25.13 ± 1.30

TABLE 3.3: Estimated crystalline size, obtained thought the application of Scherrer equation to the obtained XRD data.

3.2.1.3 Optical characterization

Figure 3.11 shows the absorption spectra for the photoanodes, presenting the characteristic hematite absorption peaks, the local maximum around 440 nm [8, 12] and the maximum around 530-540 nm, indicating occurrence of a red-shift [8, 31, 77]. A transition in the absorption coefficient for greater wavelengths has been previously attributed to spin-forbidden ligand field (6A1 $\rightarrow$ 4E) transition and is related to changes in the nanostructures morphology [8, 31, 78].

In agreement with the XRD data, the differences on annealing temperature for the same photoanode configuration did not presented observable variations on the absorption curve or intensity (Figure 3.11). However it is possible to observe a slight increase on the absorbance when a Ti layer bellow the Fe thin film and a significant increase, especially for higher wavelengths, when the Ti layer is presented at the top of Fe (Table 3.4).

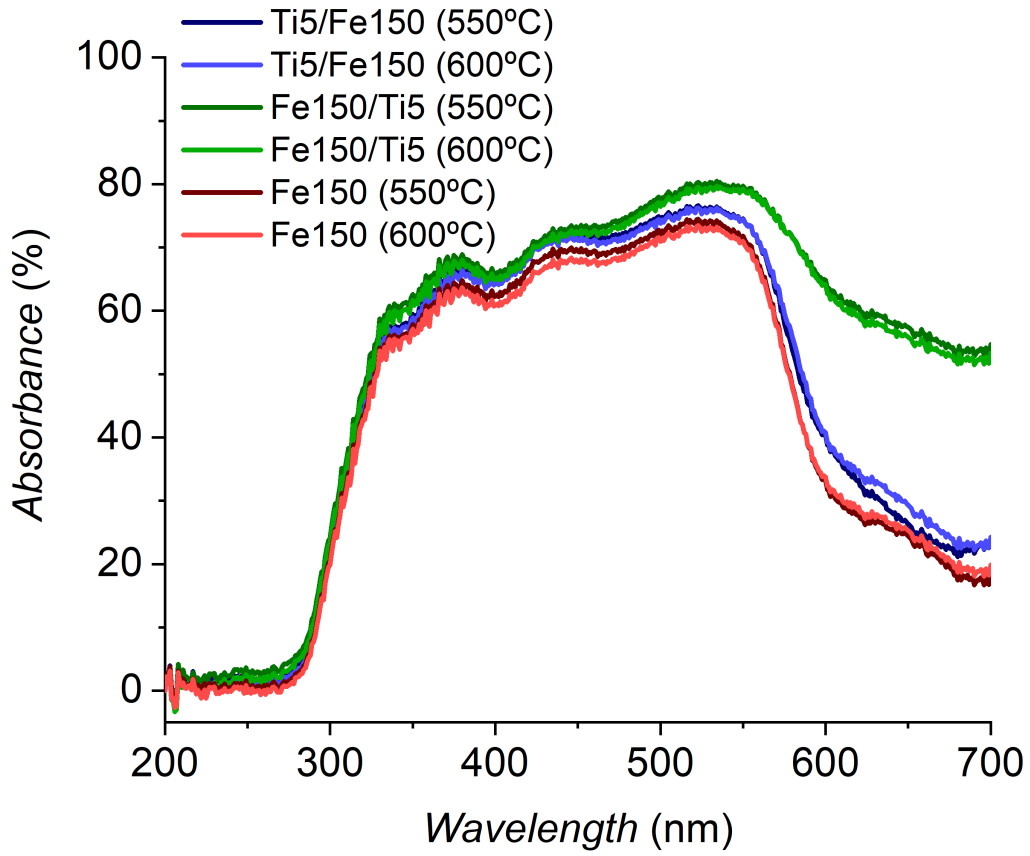


FIGURE 3.11: UV-Vis absorption spectrum of thin films of hematite and titanium dioxide.

Composition	Absorbance (%)
Fe150	74
Ti5/Fe150	76
Fe150/Ti5	81

TABLE 3.4: UV-Vis spectrum, absorbance at the maximum wavelength ($\approx$ 540 nm).

3.2.1.4 Photoelectrochemical performance

The photoelectrochemical performance of the photoanodes was measured thought photocurrent density-voltage (j-V), at AM (Air Mass) 1.5G (Global) under dark and simulated sunlight. The incidence of simulated sunlight occurred for front and back illumination photoanode setups.

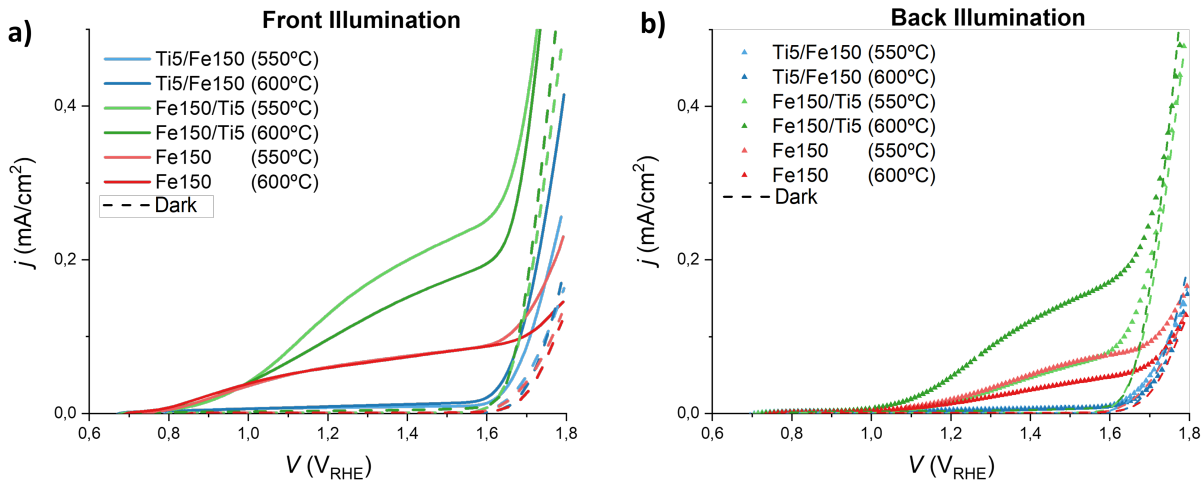


FIGURE 3.12: j-V characteristic curve for the different photoanodes compositions in study, prepared with a one step annealing at 550 ºC and 600 ºC (a) Front illumination (b) Back illumination

As predicted by the absorption of the compositions in study, Fe150/Ti5 presented higher photocurrents when compared with the other configurations (Figure 3.12). This indicates more photogenerated electron-hole pairs participating on the reactions, resulting in a higher production of hydrogen.

It was observed an increase in the photocurrent from 0.08 mA/cm^2 to 0.21 mA/cm^2 when a Ti layer was deposited on top of hematite, which translates in an enhancement of the PEC performance. This behaviour could be explained by an suppression of surface state recombination due to a stronger electric field near the surface [79]. The photocurrent decrease when Ti was present at the FTO interface could be explained by the introduction of recombination sites, at the FTO/TiO_2 interface [80], that due to their locations, are hardly avoidable for the photogenerated electrons.

3.2.2 Two step annealing

The previous study revealed an improvement on the photocurrent when the photoelectrodes were annealed at a temperature of 550 ºC during 2 hours. In order to study high temperature step of annealing, it was added a second-step at 800 ºC for 20 min as it is showed on Table 3.5. The 800 ºC annealing temperature was reported to enhance the photocurrent [8, 81, 82], promoting the Sn diffusion from the FTO to the photoanode, altering the hematite properties [79, 82, 83]. Despite the incorporation of Sn into the hematite lattice, the loss of Sn will degrade the electrical conductivity of FTO, making harder the electron collection [81]. To prevent an excessive depletion of Sn at FTO or the substrate deformation due to the high temperature, a 20 minutes annealing at 800 ºC was reported to be the optimized annealing time [8].

Through this procedure it was expected a better homogenization of the photoanode and the diffusion of Sn, present on the FTO substrate, to the thin film, doping him [8, 66, 79, 81, 83] . Due to the high temperature of annealing, it was used an FTO 10-10 substrate with higher temperature resistance than the FTO 22-7 used before.

Temperature(ºC)	Time (min)	Ramp (ºC/min)
550	120	1
800	20	8

TABLE 3.5: Two step annealing conditions.

3.2.2.1 Morphological Characterization

The two-step annealing did not significantly change the naked eye appearance of the samples, when compared with a lower temperature annealing. Although, through SEM analyses it was possible to verify some recurrent changes on the morphology of the thin films. Photoanodes of Fe and Ti/Fe (Figure 3.13 (a, c, d, f)), after a high temperature annealing step converted the Fe ribbon shape features into a more defined needle shape structures, occurring their reduction in number and apparent length. When Ti is present at the top of Fe (Figure 3.13 (b, e)), the conversion from ribbon shape features to needle features also occurred and the coating cover due to the Ti presence seems to decrease in roughness, possibly due to some Ti diffusion provided by the high temperatures.

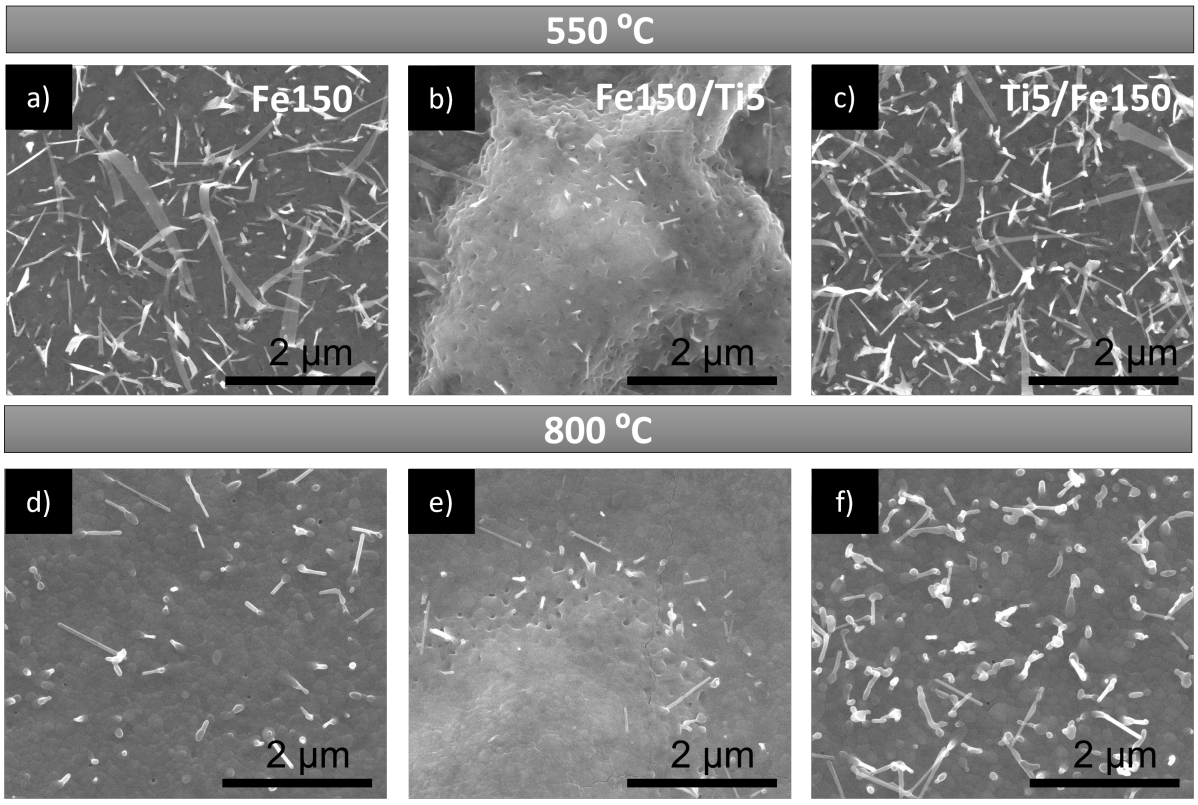


FIGURE 3.13: Thin films transformations after an extra annealing step of 800 ºC during 20 minutes, (a, d) FTO/Fe150 after 550 ºC and 800 ºC, respectively; (b,e) FTO/Fe150/Ti5 after 550 ºC and 800 ºC, respectively; (c,f) FTO/Ti5/Fe150 after 550 ºC and 800 ºC, respectively.

3.2.2.2 Structural Characterization

Figure 3.14 shows the XRD spectra of the hematite and titanium dioxide thin film compositions after a two-step annealing with a first step at 550 ºC, followed by an high temperature second annealing step at 800 ºC.

After the extra annealing step at 800 ºC, the (104) hematite preferential growth was presented in all the arrangements (Figure 3.15 and Table 3.6). The inversion on the preferential peak for Ti5/Fe150 thin films can be related to the conditions of the different substrates of the Fe nucleation during Fe deposition and growth, which occurs on TCO substrate or on the Ti layer.

Applying Scherrer equation as described before, it as possible to estimate the crystallite size (Table 3.7).

As seen before, the estimated crystalline size does not present significant changes when there is introduced a Ti layer, at the top or at the bottom of the Fe thin films. The

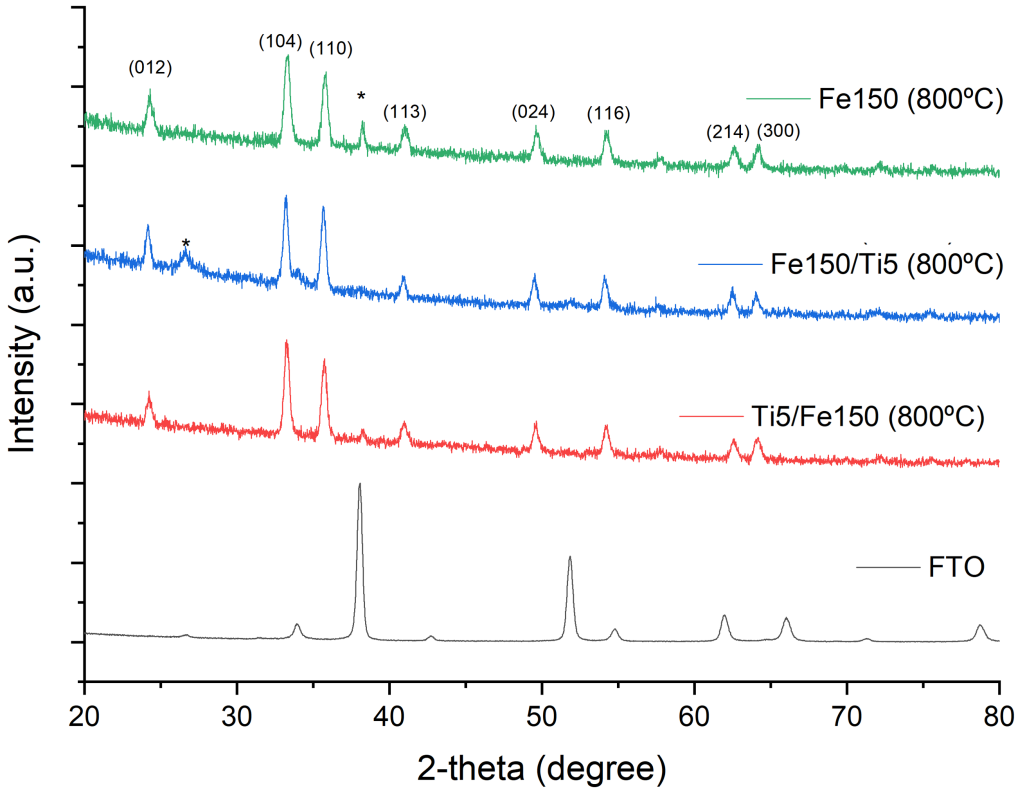


FIGURE 3.14: XRD spectra of thin films composed by $\alpha - Fe_2O_3$ and TiO_2, annealed at the 550 ºC plus 800 ºC. The peaks marked represent hematite and * symbol indicates FTO peak contributions.

Composition	2θ (104) Peak	2θ (110) Peak	I (104)/I (110)
Fe150 (550ºC)	33.26	35.74	1.04
Fe150/Ti5 (550ºC)	33.14	35.66	1.11
Ti5/Fe150 (550ºC)	33.30	35.74	0.87
Fe150 (800ºC)	33.30	35.80	1.12
Fe150/Ti5 (800ºC)	33.24	35.66	1.08
Ti5/Fe150 (800ºC)	33.26	35.76	1.13

TABLE 3.6: Position (2θ) and relative intensity of the peaks (110) and (104) on hematite when combined with a titanium dioxide layer after a two-step annealing with maximum temperature of 800 ºC, and the respective comparison with low annealing temperatures of 550 ºC.

increase on annealing temperature also does not present any variation on the crystallite sizes (Table 3.7).

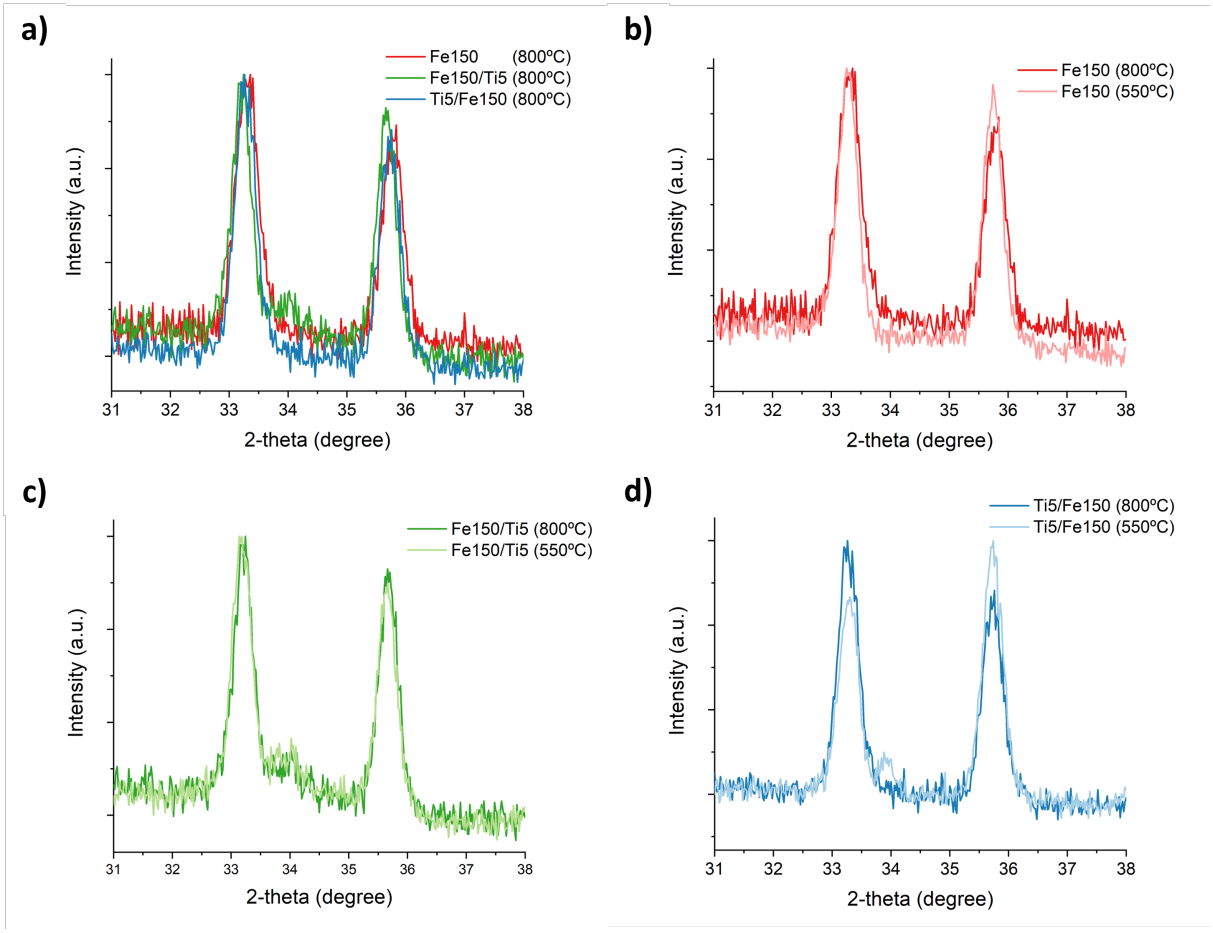


FIGURE 3.15: XRD spectra at the major peaks of hematite a) with all the configurations annealed at 800 ºC; and influence of the high annealing step on (b) Fe configurations (c) Fe/Ti configurations (d) Ti/Fe configurations.

Composition	Crystallite size (nm)
Fe150 (550ºC)	26.23 ± 1.51
Fe150/Ti5 (550ºC)	26.01 ± 1.36
Ti5/Fe150 (550ºC)	25.22 ± 1.29
Fe150 (800ºC)	22,95 ± 1.24
Fe150/Ti5 (800ºC)	26,65 ± 1.53
Ti5/Fe150 (800ºC)	24,47 ± 1.31

TABLE 3.7: Estimated crystalline size, obtained thought the application of Scherrer equation to the obtained XRD data for photoanodes submitted to an 800ºC annealing, and the respective comparison with low annealing temperatures of 550 ºC.

3.2.2.3 Optical Characterization

Comparing the absorbance spectra of compositions annealed at low temperature and high temperature, Figure 3.16, it is observed higher absorption intensity for the samples

submitted to a 800 ºC annealing step. This can be attributed to the fact that annealing temperature increases the hematite absorption, and to the diffusion of Sn from FTO substrates into hematite, as already reported in the literature for hematite nanostructures [8, 31, 84, 85].

The increase on the annealing temperature produced better absorbance intensities for photoanodes where a Ti layer was deposited. This results are in agreement with the absorbance data previously obtained for low temperature annealings, however the slight difference on absorption due to the Ti layer position on 550 ºC annealings seems to disappear after the 800 ºC annealing step (Table 3.8), which could indicate the diffusion of Ti into the hematite lattice. Another observable modification in the spectra is a slight redshift for the photoanodes annealed at 800ºC, which is usually attributed to factors such as nanostructuring, morphology, the annealing temperature or the use of dopants [8, 31, 84].

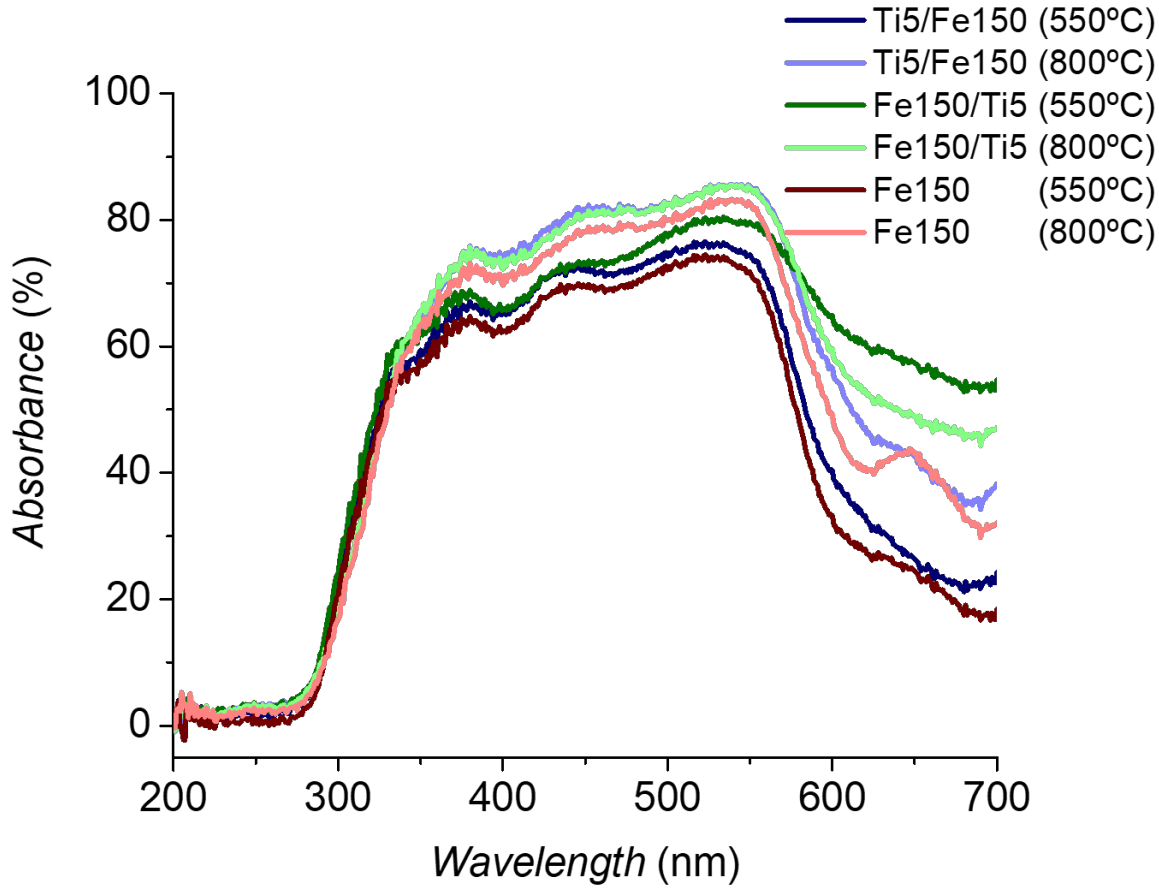


FIGURE 3.16: UV-Vis absorption spectrum of thin films of hematite and titanium dioxide annealed at high temperatures.

Composition	Absorbance (%) at 550 ºC	Absorbance (%) at 800 ºC
Ti5/Fe150	76	86
Fe150/Ti5	81	86
Fe150	74	83

TABLE 3.8: Absorbance in percentage at a maximum absorption wavelength for the different compositions, with and without 800 ºC step annealing.

3.2.2.4 Photoelectrochemical performance

Figure 3.17 shows the photocurrent density (j-V) curves after the addition of the second-step annealing at 800 ºC for 20 minutes. The high temperature annealing, promoted higher energy supplies for the atoms arrangement on the lattice, as well as the Sn diffusion from the FTO into the hematite lattice, altering the photoanode properties [79, 82], increasing the performance of the PEC cells.

The transformations provided by the high temperature favored all the photoanode configurations, where the best configuration (Fe150/Ti5) increased the photocurrent from 0.21 mA/cm^2 to 0.59 mA/cm^2, almost tripling the outputs (Table 3.9).

As occurred for the low temperature annealings, on high temperature annealings, front illumination measurements obtained better photoelectrochemical performances due to the photogeneration of e-h pairs near the semiconductor-electrolyte interface, where there is needed less travel length for the reaction of the minority charge carriers (holes). Thought the back-illumination measurements it is possible to observe an inversion on the photoelectrochemical performance, indicating the improvement on photocurrent when the sunlight illuminates firstly the TiO_2 layer, this happens due to relative position of the CB and VB of TiO_2 and hematite that favors the charge carrier passage from the TiO_2 to hematite.

On back illumination the holes tend to be produced near the FTO/film interface, and due to their short diffusion length, most of them recombine without reaching the electrolyte interface, reducing the photocurrent output when compared with front illumination measurements [8, 30].

The photocurrent enhancements promoted by the high temperature annealing (Table 3.9) are due to the Sn diffusion from the substrate into the hematite lattice, increasing the electron density [22] and promoting an upward multiband bending, forming electric fields that facilitate the movement of the photogenerated holes toward the semiconductor/electrolyte interface [10].

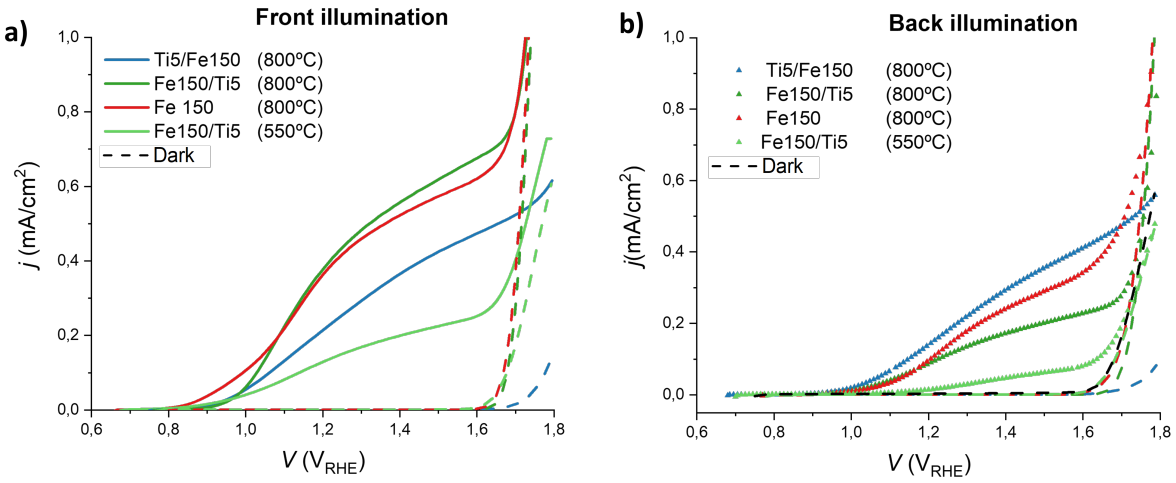


FIGURE 3.17: j-V characteristic curves for thin films of hematite and titanium dioxide with one-step annealing at 550 ºC or with an extra-step at 800 ºC. (a) Front-illumination (b) Back-illumination

Composition	Current (mA/cm^2) at $1.45V_{RHE}$
Fe150 (550 ºC)	0.08
Fe150/Ti5 (550 ºC)	0.21
Ti5/Fe150 (550 ºC)	0.01
Fe150 (800 ºC)	0.55
Fe150/Ti5 (800 ºC)	0.59
Ti5/Fe150 (800 ºC)	0.40

TABLE 3.9: Photocurrent values $1.45V_{RHE}$ for photoanodes composed by Fe and Ti, annealed at one step annealing of 550 ºC and at two step annealing with maximum temperature of 800 ºC.

Relating photocurrent with ratio between the principal hematite peaks, its possible to observe an increase of photocurrent when the peak ratio decreases, indicating a photocurrent favoring at relatively more intense (110) peaks (Figure 3.19). The peak (110) is referred by several reports to have a higher anisotropic conductivity, when compared with the direction perpendicular to it [(104) peak] [7, 8, 30, 66] , which is corroborated by the results showed on Figure 3.19.

The hematite bulk properties could be altered due to the incorporation of Ti atoms [46], enhancing the photoelectrochemical performance, however it is also noticeable an anodic shift in the photocurrent onset potential, due to Ti diffusion promoted by the thermal annealing (Table 3.10) [50]. The anodic shift can be related to the change on i-SS surface state, promoted by the addition of a Ti layer [50].

Composition	Onset potential (V)
Fe150 (800 ºC)	0.85
Fe150/Ti5 (800 ºC)	0.95
Ti5/Fe150 (800 ºC)	0.92

TABLE 3.10: Onset potentials for photoanodes composed by Fe and Ti, annealed at a two step annealing with maximum temperature of 800 ºC

3.3 Conclusions

In this chapter, it was studied the impact of the annealing temperature (550 ºC and 600 ºC) during 120 minutes on FTO 22-7 substrates and the influence of the addition of an second high temperature annealing step resulting in 550 ºC for 120 minutes + 800 ºC during 20 minutes, on FTO 10-10 substrates. Both annealings converted the Fe and Ti into their respective oxides, producing orange color thin films.

Firstly, the annealing at 550 ºC produced very similar results for the configurations of Fe and Ti/Fe thin films, however when it was applied on Fe150/Ti5 thin film, it produced an improve of more than 160 % on the photocurrent. Implementing an extra step of 800 ºC during 20 minutes to the previous best annealing (550 ºC), it was verified an increase in all the tested configurations.

The enhancement on the photocurrent after the 800 ºC annealing is explained through the Sn doping, increasing the electron density and promoting electric fields that facilitate the holes movement in the direction of electrolyte interface.

The photoanodes were characterized topologically thought SEM, revealing that for annealings at low temperature, the thin films formed characteristic ribbon shape features at the surface, due to the presence of Fe, that were transformed into needle shape features after the high temperature annealing step.

UV-Vis measurements revealed better absorbance for photoanodes with the presence of TiO_2. The increase on the temperature annealings produced an increase on the absorbance of the photoanodes, keeping the best performances for photoanodes with Ti, and introducing a red-shift on the maximum absorption wavelength for all the configurations.

In resume, the configuration of Fe150/Ti5 revealed higher photocurrents, regardless of the annealing, reaching (0,21 mA/cm^2) for the annealing at 550 ºC and (0,59 mA/cm^2)

with the addition of the 800 ºC extra step. This data is corroborated with the UV-Vis spectrum which demonstrates a greater absorption capacity for this configuration.

Chapter 4

The influence of Ti layers thickness in hematite photoanodes

The addition of a thin TiO_2 layer to hematite photoanodes enhanced the photoelectrochemical performance. In this chapter, the thickness variation of TiO_2 layer in the photoanodes performance is analysed as well as their morphological, optical and structural influence on the thin films.

4.1 Morphological characterization

As discussed in the previous chapter the double-layers Fe and Ti thin films growth, follows the FTO morphology. By increasing the Ti layer up to 50 nm and maintaining Fe at 150 nm, the morphology took a similar spherical shape with an average radius of $0.195 \pm 0.021\ \mu m$ for Ti at the top and $0.189 \pm 0.023\ \mu m$ for Fe at the top (Figure 3.4).

Samples annealed at a low temperature, with Ti50/Fe150 configuration, kept the ribbon shape features presented in Ti5/Fe150 configuration (Figure 4.1). On Fe/Ti configurations, the Ti layers acts as a coating layer, decreasing the total number of ribbon features, leading almost to their disappearance for thickness in order of 50 nm (Figure 4.1).

When the annealing treatment proceeded to a second step at 800 ºC, the ribbon shape features on Ti/Fe configurations, were transformed into needle shape features, independently on the Ti thickness bellow the Fe layer. While on Fe150/Ti50 thin film, Ti fully covers the surface of the film, hiding any presence of Fe as well as the appearing of the features observed on the previous configurations (Figure 4.2).

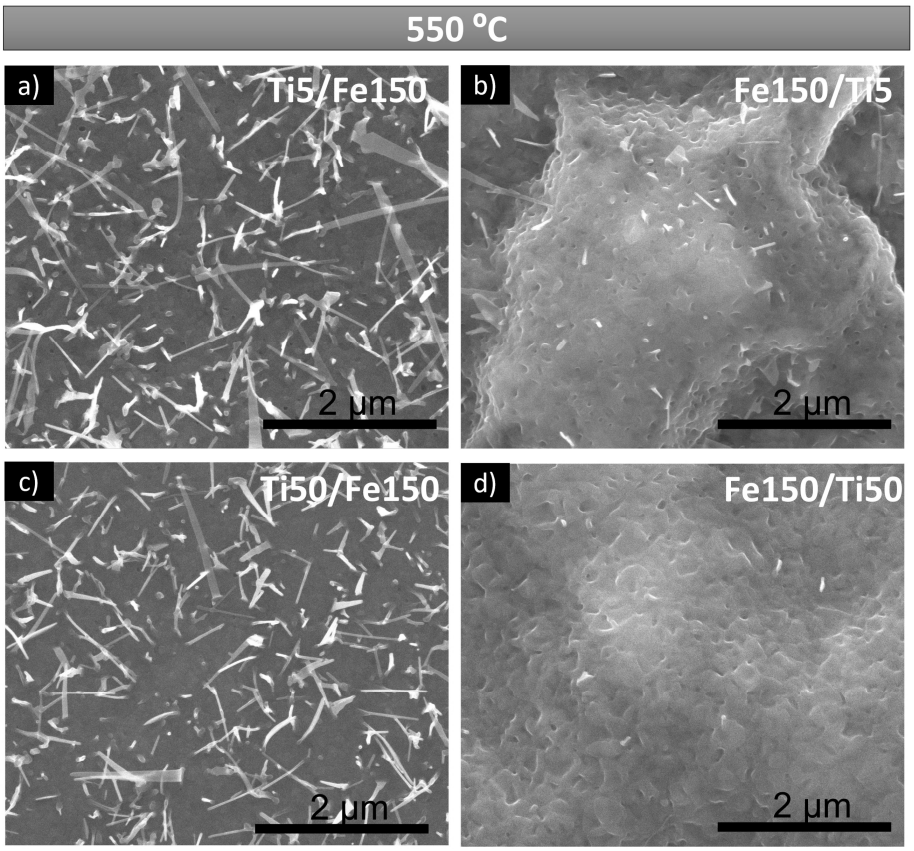


FIGURE 4.1: SEM image of the surface morphology of thin films annealed at 550 ºC with compositions of a) Ti5/Fe150; b) Fe150/Ti5; c) Ti50/Fe150; d) Fe150/Ti50.

High temperature annealing at 800 ºC, allows the film to restructure, converting the ribbon shape features into a more solid structure (needles), however, due to the high temperature, it also produce some unavoidable cracks on the films surface, visible on the Figure 4.2 (d).

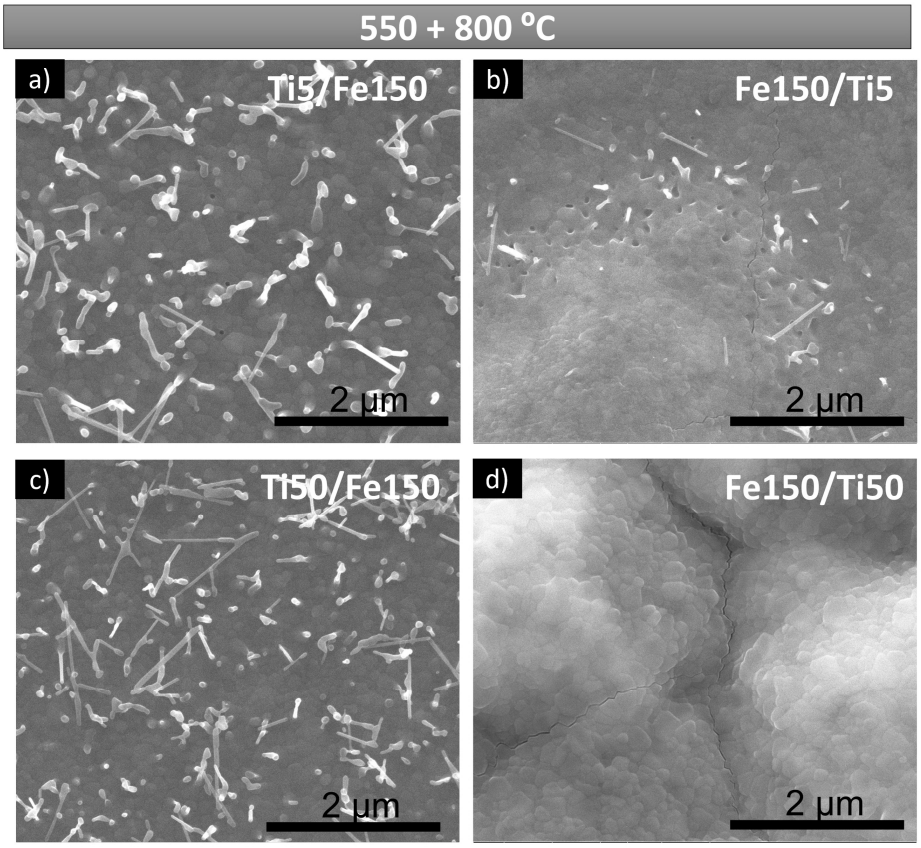


FIGURE 4.2: SEM image of the surface morphology of thin films annealed with an extra step at 800 °C with compositions of a) Ti5/Fe150; b) Fe150/Ti5; c) Ti50/Fe150; d) Fe150/Ti50.

4.2 Structural characterization

Figure 4.3, shows the XRD spectra for photoanodes with increased thickness of Ti layer (50 nm). The increase of Ti layer leaded to the appearing of some titanium dioxide peaks on the spectra.

TiO_2 presence is visible on XRD analysis trough the peaks (110), at the respective 2θ angle of 27.48 degrees, corresponding to the Rutile phase. Due to the annealing conditions, we believe that this crystalline phase TiO_2 is also present on the thin films with 5 nm of Ti, however due to the thin thickness the peaks are only detectable when the thickness increases.

Figure 4.4 shows the XRD difractograms for different Ti thickness on thin films annealed at the same temperature to analyse the hematite major peak position and their intensities (Table 4.1). In agreement with the results of Chapter 3, is evidenced that the growth of Fe at the top of Ti after their oxidation, for both annealing temperatures, leads to the peak (110) as preferential, where an increase on the Ti thickness leads to an increase

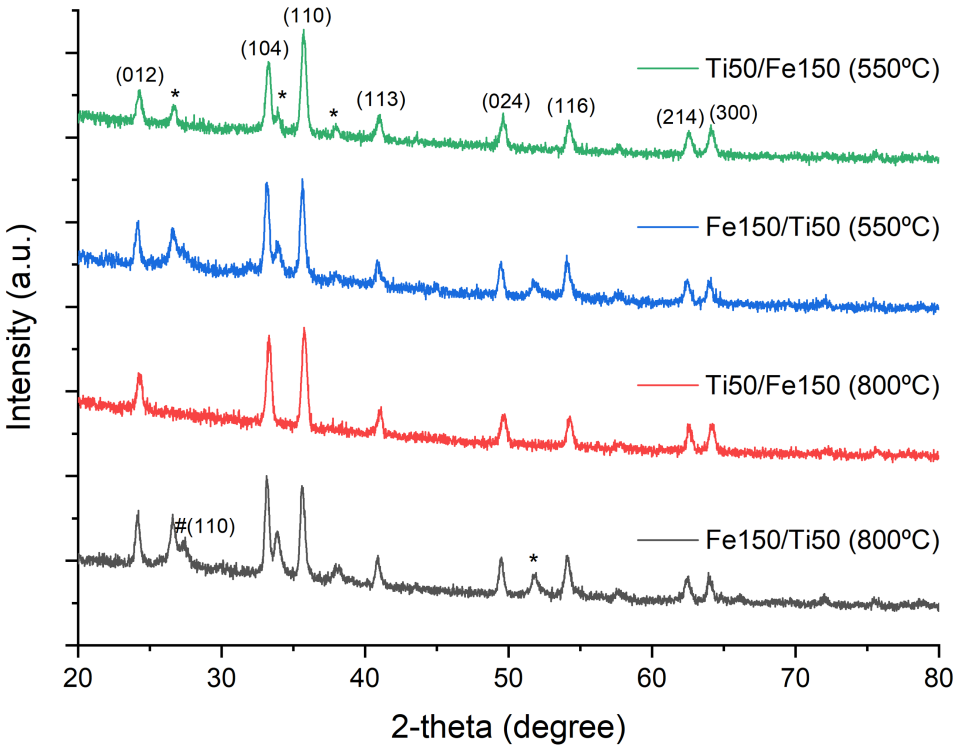


FIGURE 4.3: XRD spectra of thin films composed by hematite and TiO_2, annealed at low and high temperature. The peaks marked represent hematite, * symbol indicates FTO peak contributions and # represent the titanium dioxide phase.

on the relative intensity of (110) peak. After high temperature annealings, (104) becomes the preferential crystallographic growth direction except when the hematite grows above Ti layers with thicknesses in order of 50 nm.

Composition	2θ (104) Peak	2θ (110) Peak	I (104) / I (110)
Fe150/Ti5 (550ºC)	33.14	35.66	1.12
Fe150/Ti50 (550ºC)	33.16	35.64	0.98
Ti5/Fe150 (550ºC)	33.30	35.74	0.87
Ti50/Fe150 (550ºC)	33.26	35.72	0.81
Fe150/Ti5 (800ºC)	33.24	35.66	1.08
Fe150/Ti50 (800ºC)	33.14	35.60	1.06
Ti5/Fe150 (800ºC)	33.26	35.76	1.14
Ti50/Fe150 (800ºC)	33.32	35.76	0.95

TABLE 4.1: Peak position and relative intensity of hematite preferential planes, for 50nm Ti thin films at different configurations and annealings.

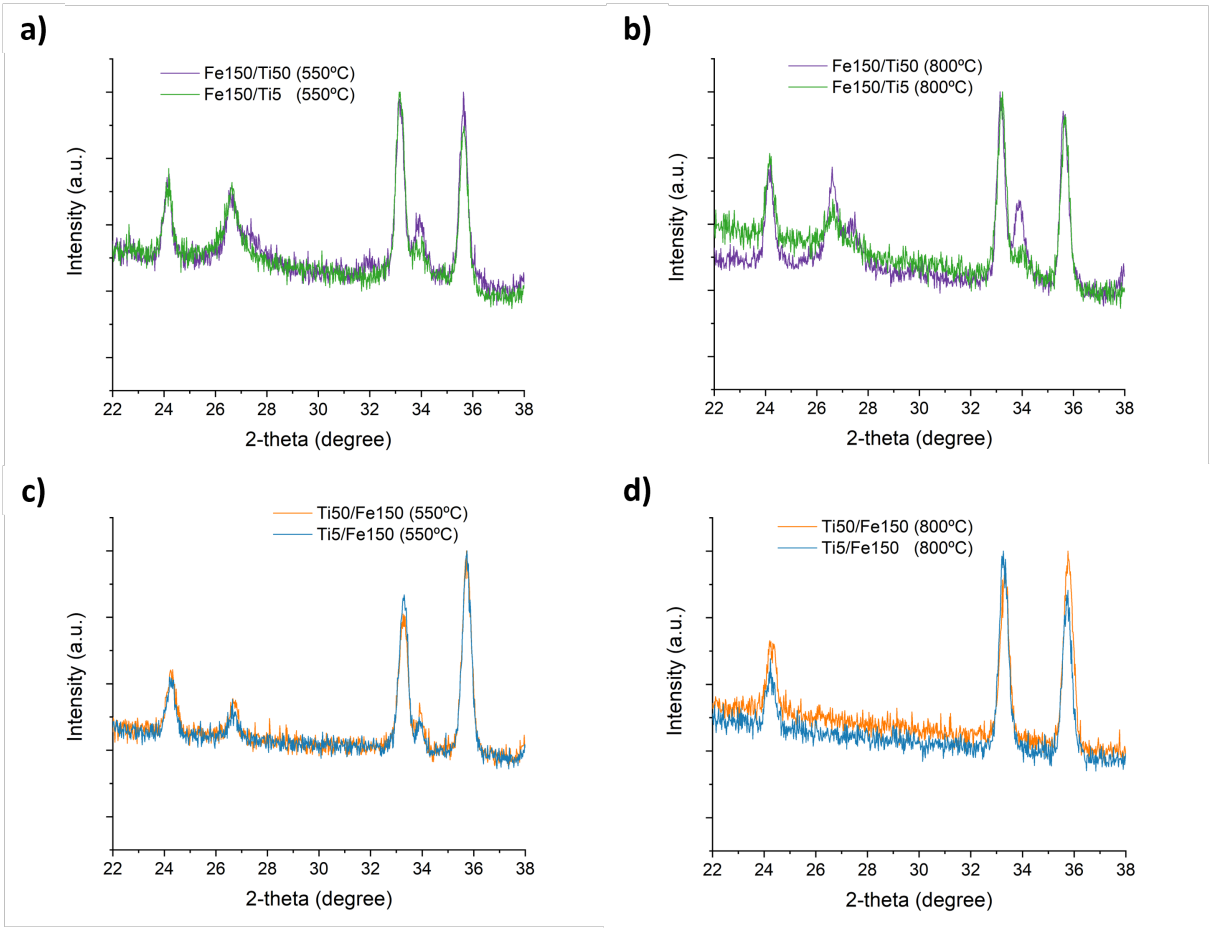


FIGURE 4.4: XRD spectra at the major peaks of hematite and rutile, comparing the influence of Ti thickness variation in thin films on Fe/Ti configurations (a) annealed at 550 ºC (b) annealed at 800 ºC; and on Ti/Fe configurations (c) annealed at 800 ºC (d) annealed at 550 ºC.

Using Scherrer equation to estimate the crystallite size (Table 4.2), there is no significant evidences of the Ti influence on the crystallite size, once the obtained values are similar to the calculated on chapter 3.

Composition	Crystallite size (nm) @550 ºC	Crystallite size (nm) @800 ºC
Fe150/Ti5	26.01 ± 1.36	26.65 ± 1.53
Fe150/Ti50	27.55 ± 1.55	26.88 ± 1.47
Ti5/Fe150	25.22 ± 1.29	24.47 ± 1.31
Ti50/Fe150	24.25 ± 1.34	24.26 ± 1.27

TABLE 4.2: Crystallite size obtained through Scherrer equations applied to the (104) and (110) hematite peaks, on combined Fe and 50nm Ti films.

4.3 Optical characterization

Through UV-Vis optical measurements, (Figure 4.5), the increase on Ti layer thickness did not produced relevant increase on the absorption of the photoanodes.

As concluded in chapter 3, when we compare the absorption lines of Fe , Ti/Fe, Fe/Ti configurations, the latter has demonstrated higher absorption for low and high temperature annealings. This configuration seems to improve the optical properties of the photoanodes.

In the case of thicker Ti layers, as already observed for 5 nm thin films, the high temperature annealing at 800 ºC also enhance the photoanodes absorption (Table 4.3). This behaviour is mainly assigned to changes on morphology and the diffusion of Sn from FTO substrates into hematite [8, 31, 84, 85]. As seen previously, the annealing at 800 ºC produced a red-shift on the maximum absorbance peak, this can be related with the annealing temperature, the incorporation of Sn into the hematite lattice and the presence of Ti layers. [8, 31, 84].

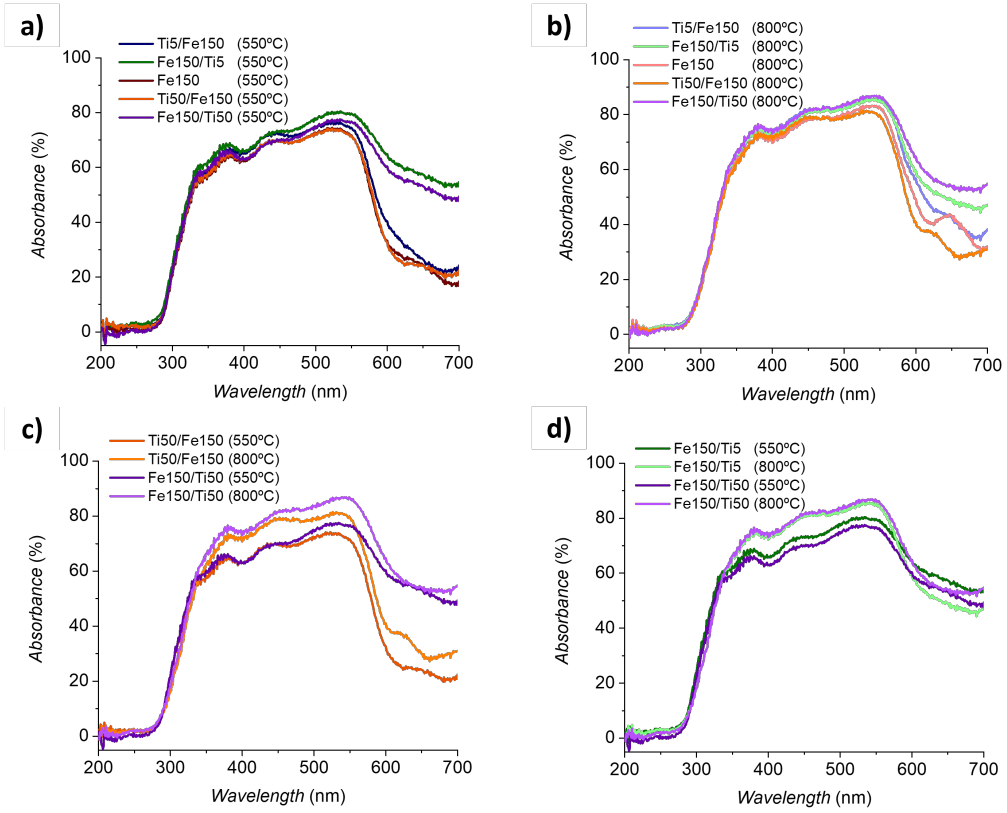


FIGURE 4.5: UV-Vis characterization, depending on the variation of Ti thickness (a) at 550 ºC annealing temperature; (b) at 800 ºC annealing temperature; (c) Ti layers with 5 and 50nm (d) on Fe/Ti configurations.

Composition	Absorbance (%) at 550 ºC	Absorbance (%) at 800 ºC
Fe150/Ti5	81	86
Fe150/Ti50	78	87
Fe150	75	83
Ti5/Fe150	77	86
Ti50/Fe150	74	82

TABLE 4.3: UV-Vis spectrum, maximum absorption peak ($\approx$ 540 nm), depending on the thickness and thin film composition.

4.4 Photoelectrochemical Performance

The photoelectrochemical performance for thicker layers of Ti (50 nm) compared with thin Ti layers (5 nm) is shown in Figure 4.6. The low temperature annealings (550 ºC), it was possible to verify that the increase from 5 to 50 nm of Ti did not produce any significant changes in the photoelectrochemical behaviour of Fe/Ti and Ti/Fe configurations, maintaining a low photocurrent performance (0.20 mA/cm^2 for Fe150/Ti50 and 0.01 mA/cm^2 for Ti50/Fe150)(Figure 4.6 (a)).

As seen in the previous chapter, the Fe/Ti configuration leads to an increase on the photocurrent density relative to Ti/Fe photoanodes that presented low photocurrent densities in all the cases.

After annealing at a high temperature, the photoanodes with increased Ti thickness kept their photocurrent for Fe/Ti configurations, while on Ti/Fe configurations it decreases. This behaviour could be explained through an limitation on the incorporation of Ti in the hematite [80] due to the high presence of Ti that can introduce charged defects which act as recombination centers [80].

Comparing with thinner Ti layers, the increase of Ti above a threshold, decreases the j-V response [42, 46], however the j-V curves corroborate the previous conclusion of the best thin film configuration, where Fe/Ti favors the performance of the device.

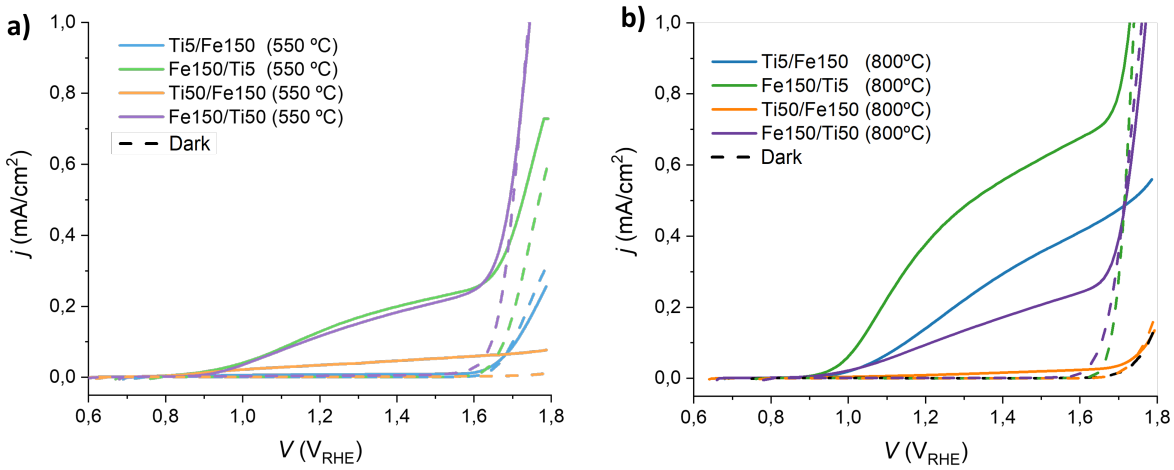


FIGURE 4.6: j-V characteristic curves for photoanodes based on hematite and titanium dioxide (a) annealed at 550 ºC; (b) annealed with an extra step at 800 ºC.

Composition	j (mA/cm^2) at 1.45V vs V_{RHE}
Fe150/Ti5 (550 ºC)	0.21
Fe150/Ti50 (550 ºC)	0.20
Ti5/Fe150 (550 ºC)	0.01
Ti50/Fe150 (550 ºC)	0.01
Fe150/Ti5 (800 ºC)	0.59
Fe150/Ti50 (800 ºC)	0.19
Ti5/Fe150 (800 ºC)	0.40
Ti50/Fe150 (800 ºC)	0.02

TABLE 4.4: j (mA/cm^2) at 1.45V vs RHE for the different samples Ti-Fe double-layers configurations at different annealing temperatures

4.5 Conclusions

When compared to thinner photoanodes, the increase on Ti thickness did not produce improvements on the photoelectrochemical performances. This behaviour can be explained due to a excessive thicker presence of TiO_2 on the films. This maybe is due to very large peculation distances that holes has to travel to reach the surface, leading to their recombination and consequent lowering on the performance of the device.

The XRD data revealed that when the hematite grows at the top of a thicker Ti layer, the (110) peak is the preferential direction of growth, being decreased their relative intensity in detriment of (104) peak after a 800 ºC annealing. As previously seen for thinner Ti

layers (5 nm), the Fe ribbon shape features presented when Ti is bellow Fe, were transformed into a more defined needle structure after the high temperature annealing while when Ti is at the top, SEM images showed a coating cover that unable the growth of those structures. The 800 ºC annealing step also produced cracks at the surface of the photoanode.

UV-Vis measurements showed that the high temperature annealing improves the photoanodes absorbance and reinforced the Fe/Ti as the best configuration on the absorption of light.

Chapter 5

The influence of hematite thickness in hematite-titanium dioxide thin films double-layers photoanodes

In this chapter, the photoanodes were optimized by decreasing the hematite thicknesses in the hematite/TiO_2 double-layers. Since the best photocurrents results were achieved with thinner TiO_2 (5 nm Ti), the layer of TiO_2 was fixed at this range of thickness. Once more, the annealing temperature was optimized for this range of thinner thicknesses. Hematite thickness was optimized and the addition of TiO_2 on thinner hematite photoanodes was studied.

Other strategies were performed in the fabrication of these photoanodes. Titanium solution was deposited through spin-coating in order to study new possibilities to achieve improved PEC performances, relying on titanium dioxide compounds. Additionnaly, a co-catalyst of FeCo oxide was deposited on the hematite thin films photoanodes as a strategy for obtaining enhanced photoresponses.

5.1 Fe thickness optimization

The photoelectrochemical mechanisms occurring on the PEC cell when sunlight photogenerates electron-hole pairs, highly depend on characteristics of the semiconductor. Hematite, as main semiconductor in study, should be optimized in order to maximize the hydrogen production outputs.

The study of the Fe layer thickness impact on the photoanodes performance (j-V characteristic curves) was performed by depositing Fe thin films layers with 50, 60 and 70 nm. Afterwards, an annealing at 600 ºC for 2 hours and a second step annealing at 800 ºC for 20 minutes was performed .

The layer with 60 nm of Fe obtained the best result with a photocurrent density of 0,55 mA/cm^2, leading to the same result that of the Fe150 nm (Table 5.1). This achievement allows to reduce the material used in cost-production of the PEC cell, facilitating the large scale implantation of PEC cells to harvest environmental friendly energy.

Fe thickness (nm)	Photocurrent density @1.45V vs RHE (mA/cm^2)
50	0.50
60	0.55
70	0.53
150	0.55

TABLE 5.1: Photo-current densities of hematite thin films with (50, 60 and 70) nm, annealed at 600 ºC + 800 ºC and Fe150 nm thin film annealed at 550 ºC + 800 ºC.

Hematite thin films typically shows enhanced photocurrents for thinner thicknesses, due to shortening of charge carrier diffusion path [44]. However literature reports that due to less interactions between the radiation and the film material, the optical absorbance decreases, counterbalancing the generated photocurrent [10, 44].

On this sense, we have performed further studies with the selected Fe thickness of 60 nm. Features like double-layers of TiO_2 (and position order) as well as the annealing conditions were explored. Figure 5.1 shows the photoanodes with 60 nm for different annealing temperatures, 550 and 600 ºC, (as previously studied in chapters 3) and with a second step annealing at 800 ºC. Either for front or back illumination (Fig 5.1 (a) and (b) respectively), an increase of the photocurrent is observed for higher temperatures, 800 ºC (550 or 600 shows the same range of results). Once again, the unintentional diffusion of Sn from the FTO substrate, doped the hematite film, acting like an electron donor and increasing the carrier density [10].

Moreover, in contrast to what happened for thicker thin films ($\leq$ 150 nm), for the samples with 60 nm the one step annealing at 600 ºC possessed a higher impact on photoelectrochemical performances than 550 ºC annealings (Figure 5.2). The second step at 800 ºC improved equally the performances of the photoanodes, with j-V curves almost overlapped in both front and back illumination.

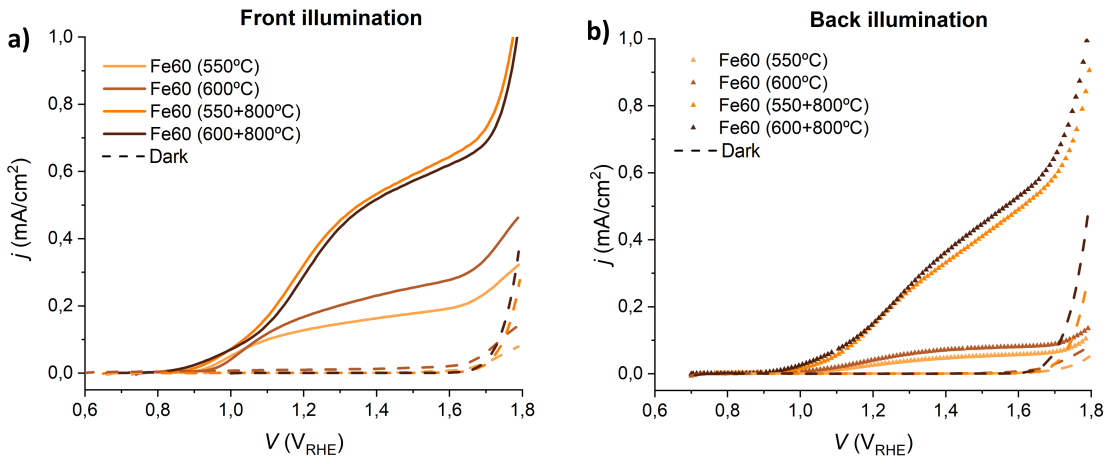


FIGURE 5.1: j-V curves on the study of annealing influence of Fe 60 nm thin film photoanodes. (a) Front illumination (b) Back illumination.

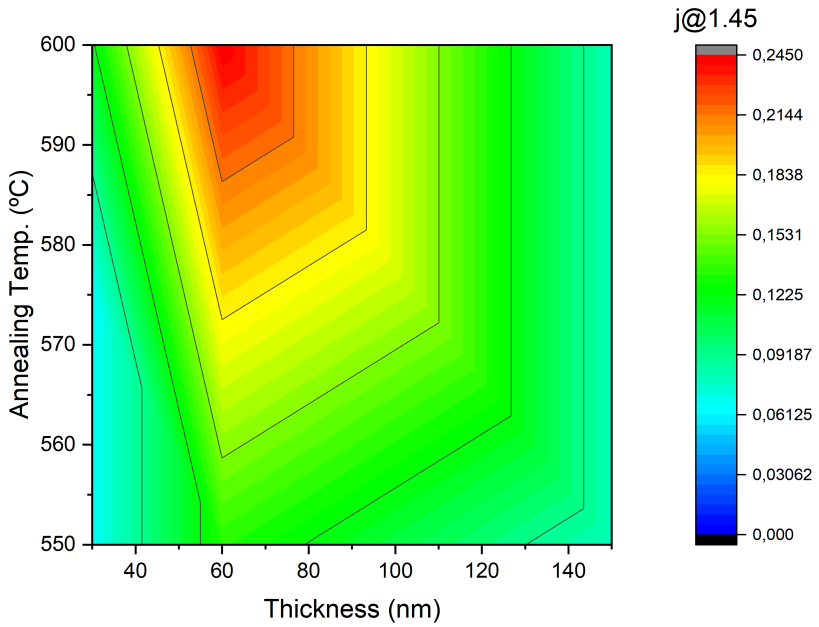


FIGURE 5.2: Contour map of annealing temperature influence on photocurrent outputs of Fe photoanodes with variable thickness.

The previous studies in chapter 3 and 4, revealed that improved photocurrent outputs are achieved with the addition a thin layer of Ti on the top of Fe. In order to study the same double-layer position effects on thinner photoanodes, 5 nm of Ti (since it was the optimized Ti thickness) was deposited above 60 nm of Fe. Afterwards, the photoanodes double layers were annealed with the sames annealing conditions as described above (Figure 5.3). Adding 5 nm of Ti, the PEC performances is enhanced, corroborating the influence of a Ti layer above Fe that was observed in chapter 3 and 4 (Table 5.2). However

on the back illumination measurements, the Fe/Ti photoanode configuration, decreased the photocurrent output. Due to an increase on the diffusion distance for the minority charge carriers to react. However, the same photocurrent trend was observed, best photocurrents for both samples with 800 ºC, followed by the ones with one step annealing at 600 and then 550 ºC.

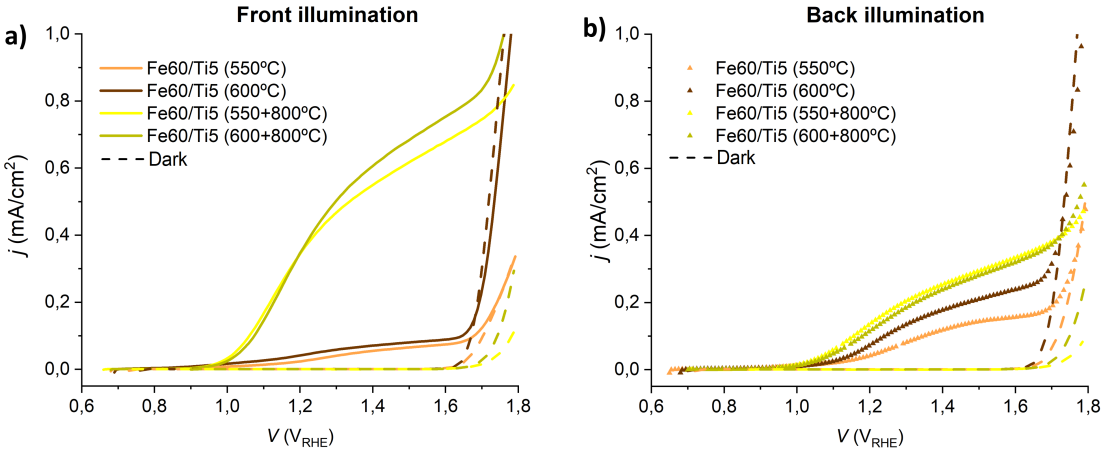


FIGURE 5.3: j-V curves on the study of annealing influence of Fe60/Ti5 thin film photoanodes. (a) Front illumination (b) Back illumination.

Configuration	Photocurrent density @1.45V (mA/cm^2)
Fe60 (550+800ºC)	0.60
Fe60 (600+800ºC)	0.55
Fe60/Ti5 (550+800ºC)	0.59
Fe60/Ti5 (600+800ºC)	0.65

TABLE 5.2: Photocurrent density of Fe60 and Fe60/Ti5 with variable annealing conditions at 1.45V vs. RHE.

Figures 5.2 and 5.4 shows the annealing temperature at the Y axis and the thin film thickness at X axis, where the color gradient represents the respective photocurrent density at 1.45V vs RHE. The j dependence on annealing temperature and film thickness revealed that low annealing temperatures at 600 ºC produced enhanced photocurrent for thinner photoanodes (in range of 60 nm), occurring an inversion of tendency for thicker photoanodes ($\geq$ 150 nm) with a Ti layer, where annealings at 550 ºC obtained higher output, as it is possible to observe on Figure 5.4.

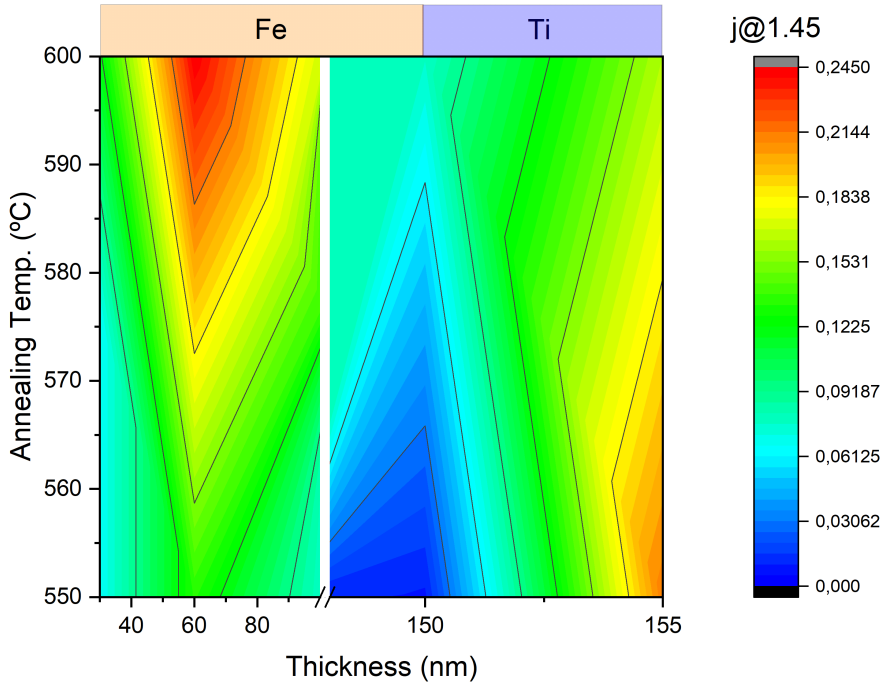


FIGURE 5.4: Contour map of annealing temperature influence on photocurrent outputs of Fe and Ti photoanodes.

5.1.1 Optical characterization

The reduction of photoanode material dimensions, directly affects their absorbance. Once their absorption is reduced due to a decrease on the interactions between the material and the electromagnetic radiation [10, 44].

The absorption spectra for thin films composed of 60 nm Fe, with and without 5 nm of Ti and with different annealing conditions, was measured through UV-Vis (Figure 5.5). For low temperature annealings, Fe60 and Fe60/Ti5 based photoanodes, the absorbance spectra does not present significant changes. The decrease on the Fe thickness caused a reduction on the maximum absorbance ($\lambda \approx 530$ nm) presented on thicker photoanodes, for high temperatures annealings the maximum absorbance for hematite photoanodes was presented at wavelengths around 440 nm. The addition of a 5 nm Ti layer, improved the absorbance of the photoanode, as previously seen on chapter 3 and 4.

By comparing the photoanodes with the 60 vs 150 nm, thicker thicknesses posses an higher absorption of the incident solar light, which is related to more photogenerated electron-hole pairs. However their photocurrent is reduced due to an higher quantity of recombination phenomenons [10].

Composition	Absorption (%) @550ºC	Absorption (%) @600ºC	Absorption (%) @550+800ºC	Absorption (%) @600+800ºC
Fe150	69	68	79	-
Fe60	62	62	73	75
Fe60/Ti5	74	75	76	80

TABLE 5.3: Maximum absorbance value obtained through UV-Vis measurements ($\lambda \approx$ 440 nm), for hematite and TiO_2 thin films with varying thickness.

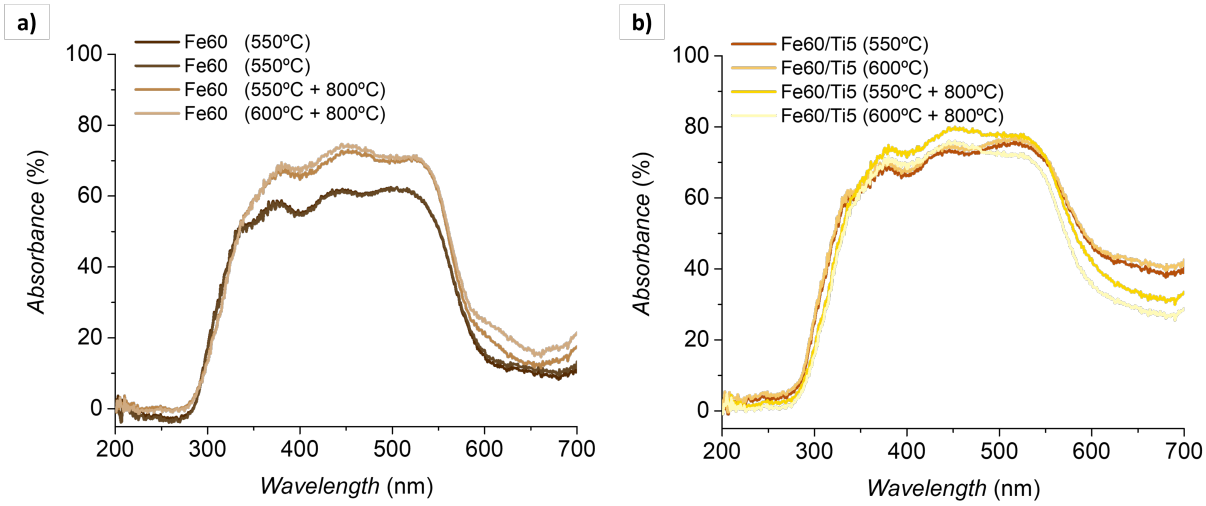


FIGURE 5.5: UV-Vis characterization, with different annealing conditions for compositions of (a) Fe60; (b) Fe60/Ti5.

By adding 5 nm Ti layer on the top of Fe (Figure 5.6 (b-d)), proved to increase the absorption of the thin film [42], achieving values comparable to thicker hematite films, which allied to the low thickness, can be the reason for the enhancement on the photocurrent density output.

On the comparison between Fe60 and Fe60/Ti5 configurations, the addition of Ti layer produced a significant increase on absorbance for low temperature annealings (Table 5.3). The increase of temperature annealing (800 ºC) shortened the differences between configurations but Ti contributions still favoured the absorbance (Figure 5.6 (c, d)).

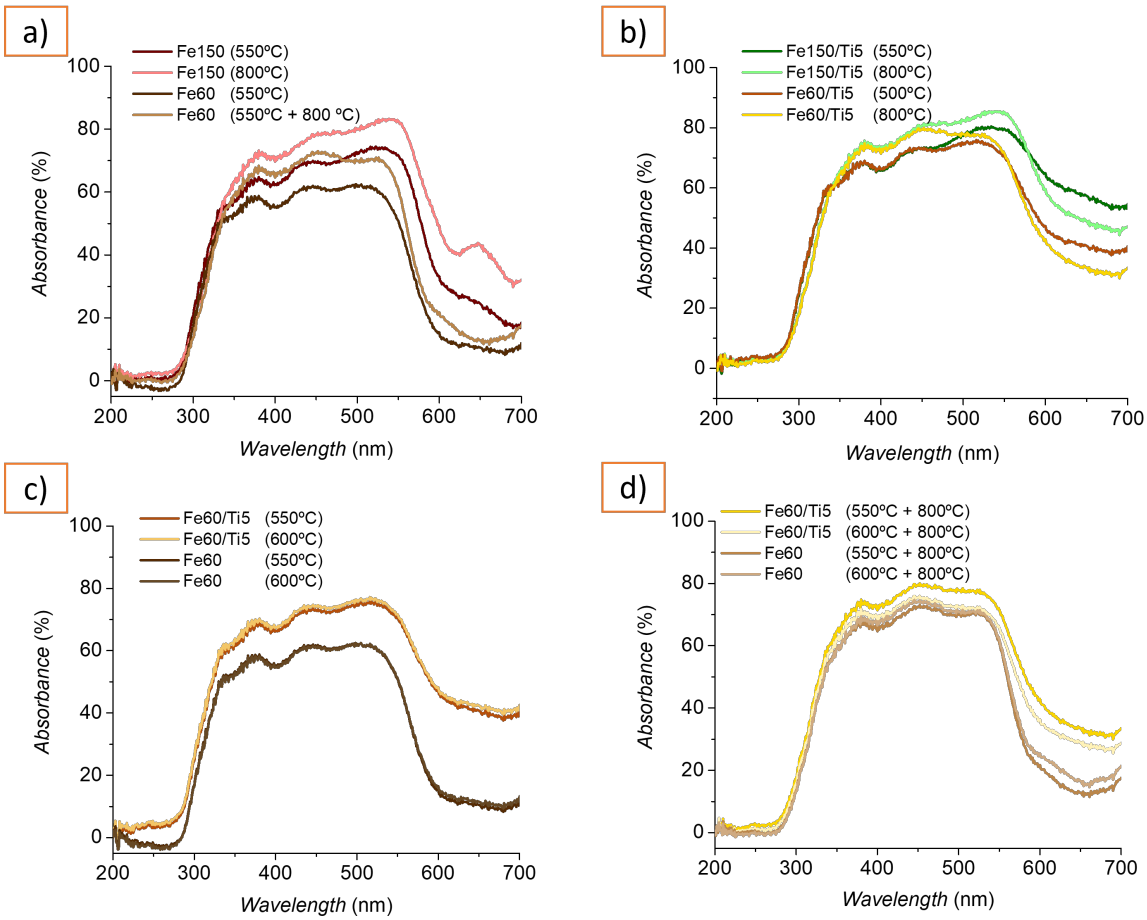


FIGURE 5.6: UV-Vis characterization, depending on the variation of annealing conditions for (a) different Fe thin film thickness, (b) with addition of a 5 nm Ti layer ; UV-Vis characterization of Fe thin films with and without 5nm of Ti at (c) low temperature annealings, (d) high temperature annealings.

5.1.2 Structural Characterization

Through the XRD measurements, the decrease on the film thickness kept the hematite DRX diffraction peaks observed for thicker films (Figure 5.7).

Taking into account the XRD data similarity between samples with a first step annealing at 550 ºC or 600 ºC, only the data corresponding to 550 ºC and 550+800 ºC annealings will be shown, in order to not overload this section.

Taking on account the ratio between the peak (104) and (110) for photoanodes thicker photoanodes ($\approx$ 150 nm of deposited material), the decrease on the Fe thickness did not presented any significant changes on the preferential growth directions in any case of study (Table 5.4, Figure 5.8, Figure 5.9).

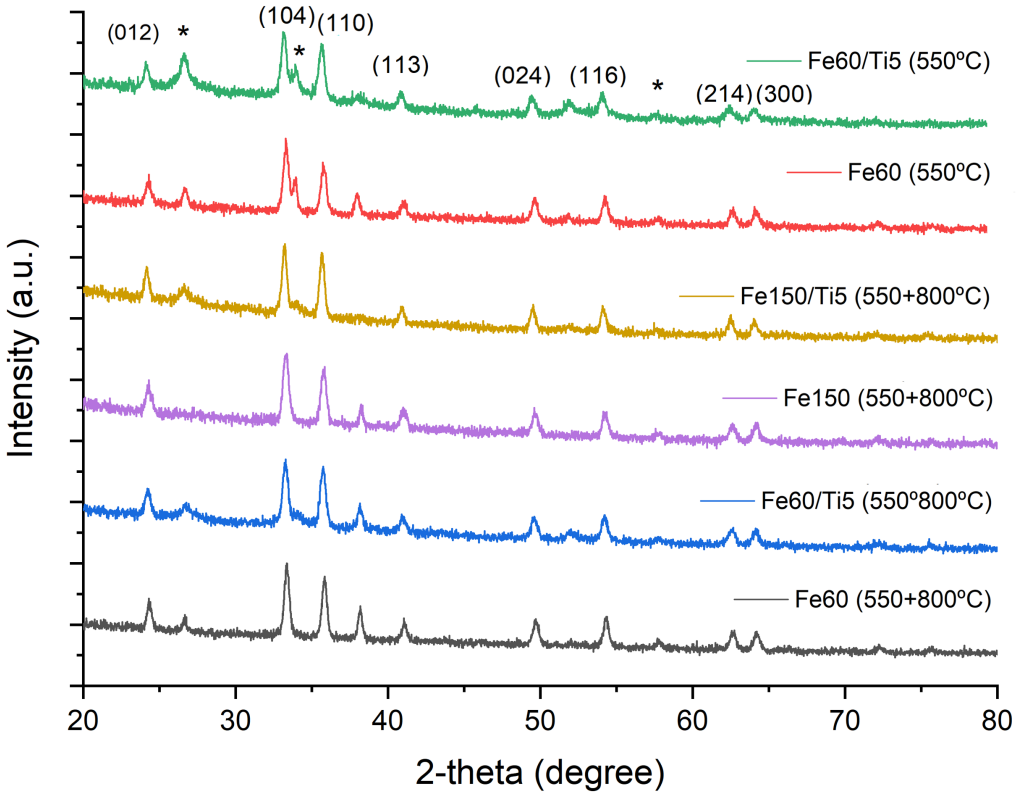


FIGURE 5.7: XRD spectra of thin films composed by hematite and TiO_2 , annealed at low and high temperature. The peaks marked represent hematite, * symbol indicates FTO peak contributions.

Composition	2θ (104) Peak	2θ (110) Peak	I (104) / I (110)
Fe150 (550ºC)	33.26	35.74	1.04
Fe150 (550+800ºC)	33.36	35.84	1.12
Fe60 (550ºC)	33.30	35.74	1.25
Fe60 (550+800ºC)	33.36	35.84	1.12
Fe150/Ti5 (550ºC)	33.16	35.66	1.11
Fe150/Ti5 (550+800ºC)	33.24	35.66	1.08
Fe60/Ti5 (550ºC)	33.12	35.62	1.11
Fe60/Ti5 (550+800ºC)	33.28	35.76	1.06

TABLE 5.4: Peak position and relative intensity of hematite preferential planes, for thinner Fe layers, at different configurations and annealings.

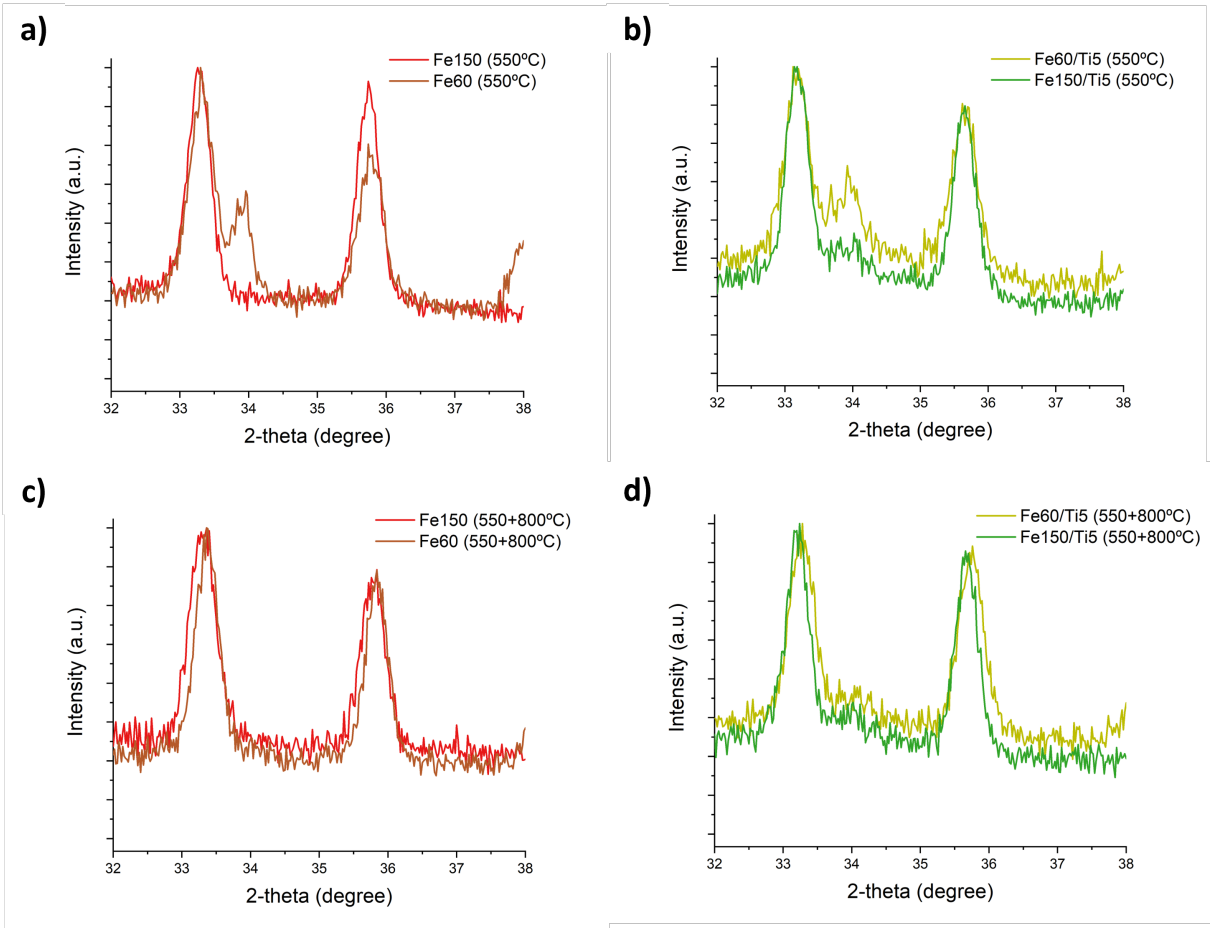


FIGURE 5.8: XRD spectra at the major peaks of hematite, comparing the influence of Fe thickness (a) at 550 ºC annealing (c) at 800 ºC annealing; and on Ti/Fe configurations (b) annealed at 550 ºC (d) annealed at 800 ºC.

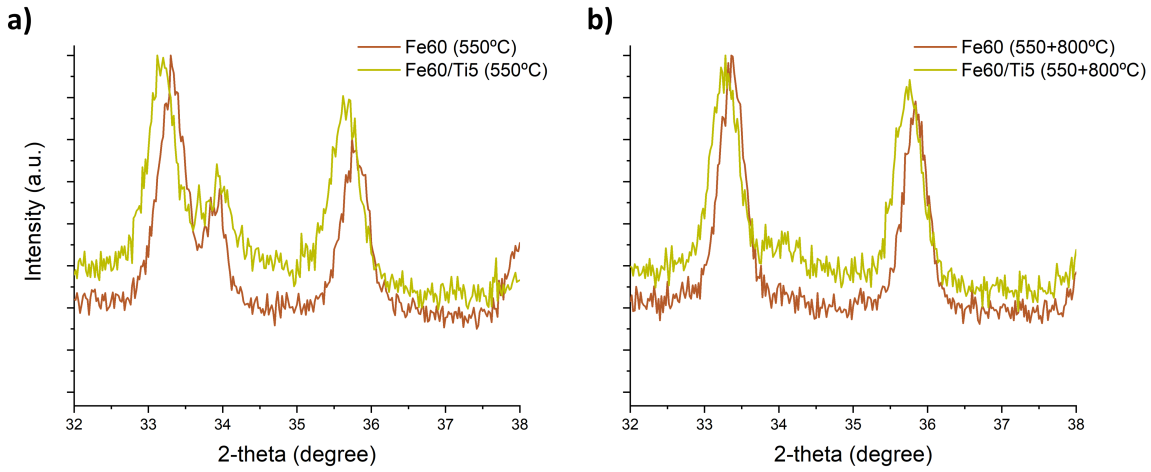


FIGURE 5.9: XRD spectra at the major peaks of hematite, comparing the influence of 5nm Ti layer addition (a) at 550 ºC annealing (b) at 800 ºC annealings.

5.1.3 Morphological characterization

On chapter 3 and 4, SEM images revealed the existence of ribbon (low temperature annealings) and needle shape features (high temperature annealings) at the surface of the film. The decrease on the Fe thickness reduced the number and the apparent size of those features (Figure 5.10), which confirms that those features are due Fe presence.

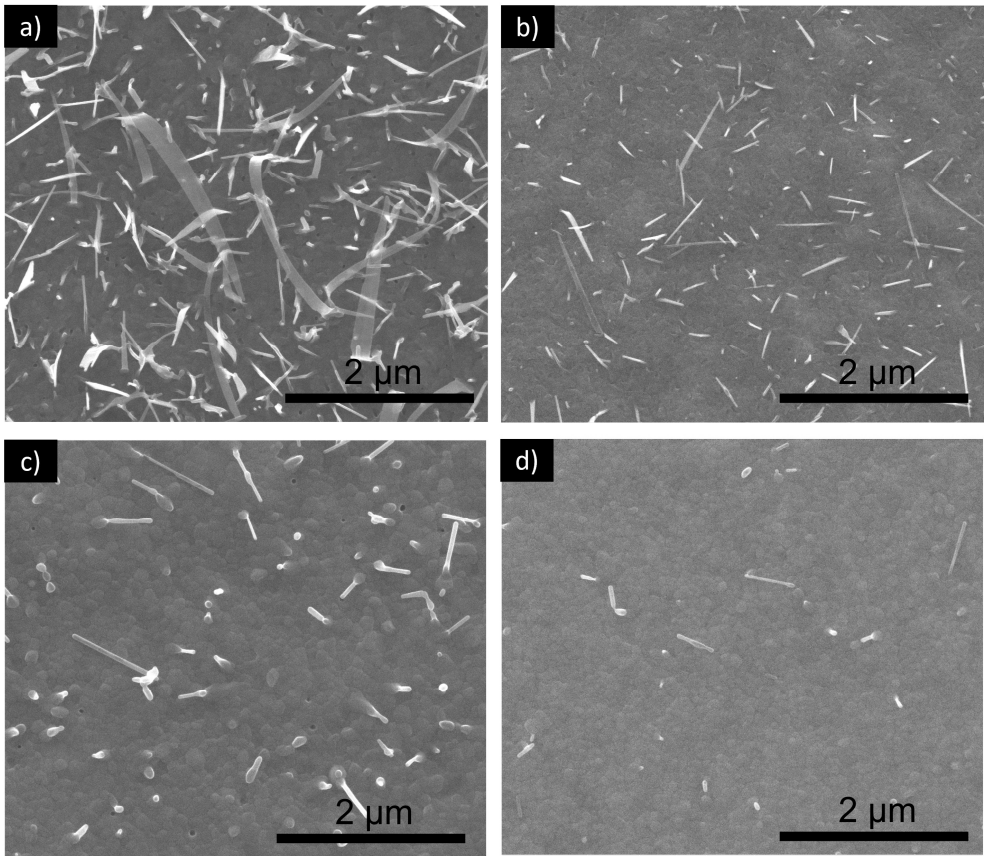


FIGURE 5.10: SEM image of thin films surface morphology with variation on Fe thickness. (a) Fe150 annealed at 550 ºC (b) Fe60 annealed at 550 ºC (c) Fe150 annealed at 800 ºC (d) Fe60 annealed at 800 ºC.

Films resorting on lower thickness of Fe (60 nm) with a Ti layer on the top, also presented a lower number of features. It appears that the number of features decreases with the decrease of Fe thickness, the increase of annealing temperature and with an increase of Ti layers at the top of the film (Figure 5.11).

With respect to photoanodes with 150 nm of Fe annealed at 800 ºC, the disappearance of these features, occurred when the Ti layer at the top of the film increased to 50 nm. For thinner Fe layers (60 nm), a 5 nm Ti layer is enough to suppress the arising of those features (Figure 5.11 (d)).

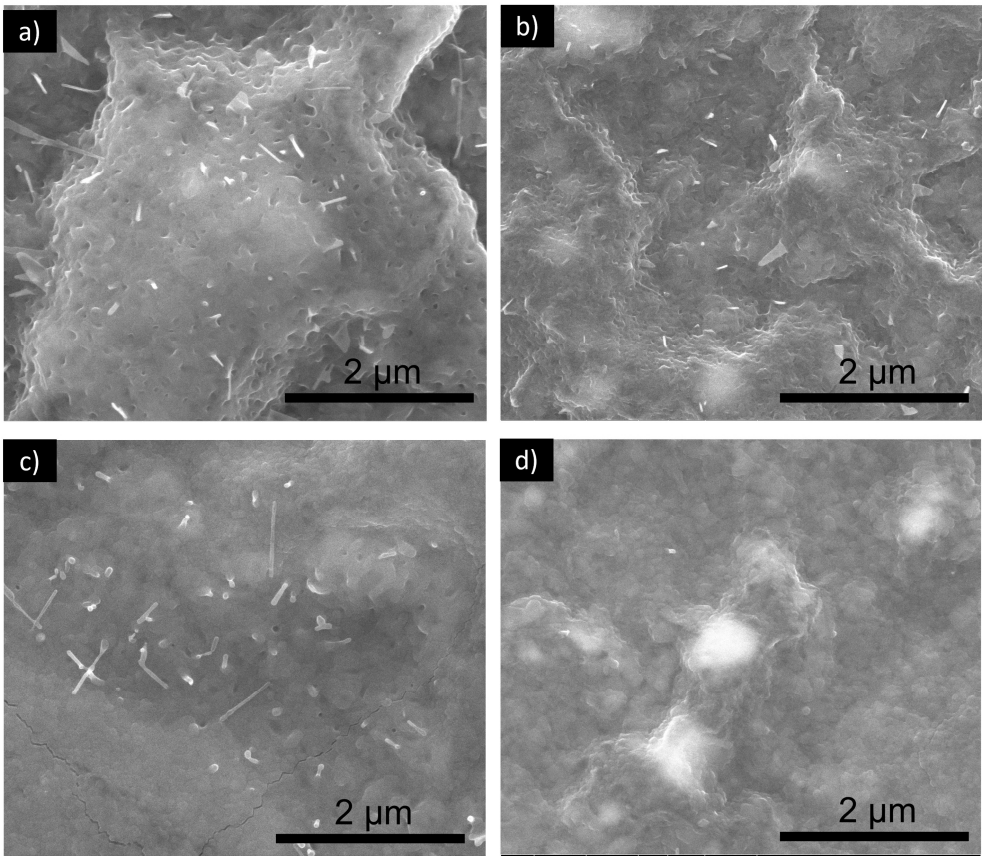


FIGURE 5.11: SEM image of thin films surface morphology with variation on Fe thickness. (a) Fe150/Ti5 annealed at 550 ºC (b) Fe60/Ti5 annealed at 550 ºC (c) Fe150/Ti5 annealed at 800 ºC (d) Fe60/Ti5 annealed at 800 ºC.

5.2 Alternative Ti deposition

Until now, chapter 3, 4 in the previous sections shown that the introduction of TiO_2 layers on hematite photoanodes changes the photoresponse. In this section we introduce an alternative fabrication route, spin coating, to deposit TiO_2 layers. Spin coating offers a uniform, fast and low-cost deposition of several titanium solutions.

To study the alternative method of depositing titanium, a 10mM titanium diisopropoxide bis(acetylacetante) solution in 75% isopropanol was used, applied on the FTO or Fe thin films as described in Experimental Techniques (Chapter 2), during 30 seconds at 1500 rpm, producing a layer of approximately 6 nm [65]. To maintain consistency in the designation of samples, titanium thin films deposited through spin coating will be designed as S.C. (Spin Coating), e.g. Fe150/S.C. (represents a thin film of 150 nm of Fe with a titanium solution at the top, deposited by spin coating).

5.2.1 Morphological and structural characterization

Through the XRD spectra of samples produced by Ti spin coating and comparison with Ti deposited by IBD (Figure 5.12), the hematite plane (104) was the preferential orientation in all the photoanodes. Ti deposited through spin coating decreased the relative intensity of (110) peak, increasing the (104) peak, principally when the Ti was deposited on the top of the film (Table 5.5, Figure 5.13).

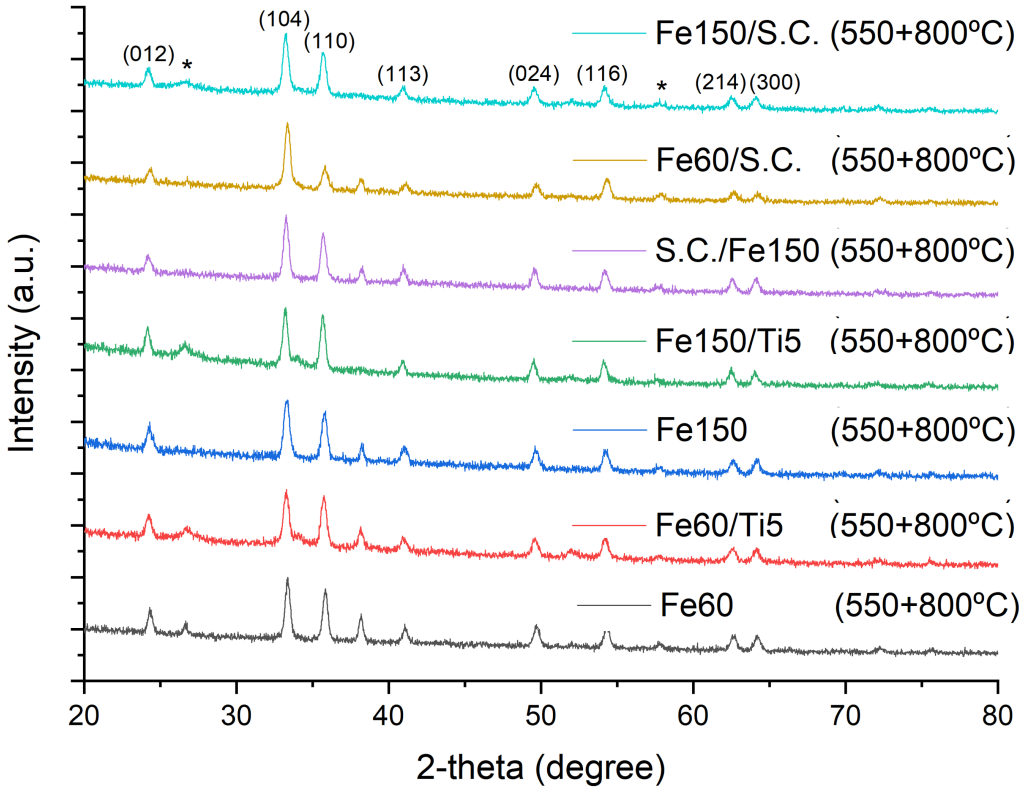


FIGURE 5.12: XRD spectra of thin films composed by hematite and TiO_2, annealed at low and high temperature. The peaks marked represent hematite, * symbol indicates FTO peak contributions. S.C. represents a layer of Ti deposited through spin coating, with a approximated thickness of 6 nm.

When the Ti based solution is deposited at the top of Fe thin film, after annealing at high temperatures, the Fe layer develops board shape features. In agreement with the previous results, the number and size of the features, depends on Fe thickness, where for thinner layers (Figure 5.14 (a, c)), the features are considerably reduced in number when compared with thicker Fe layers (Figure (b, d)).

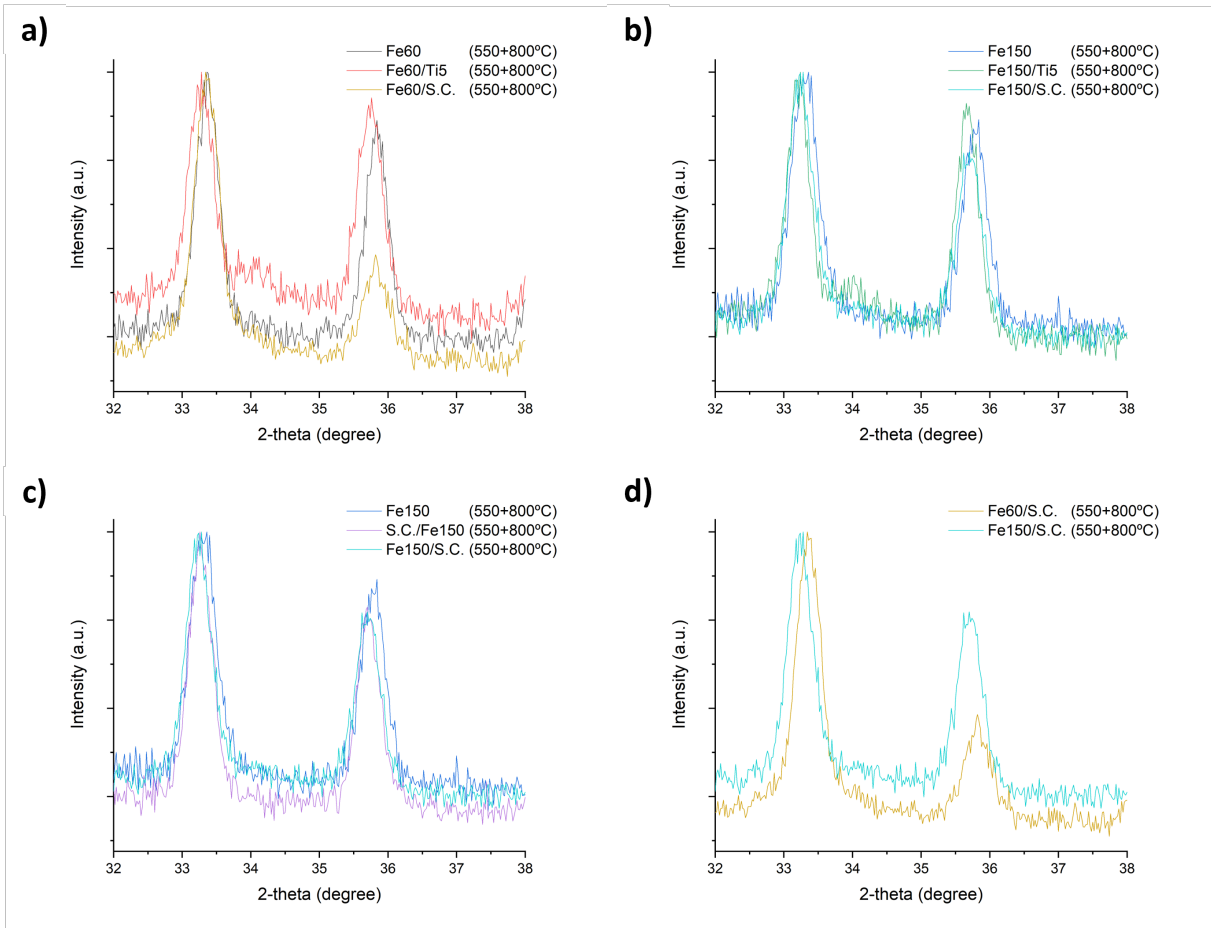


FIGURE 5.13: XRD spectra at the major peaks of hematite, comparing the influence of Ti layer addition deposited through IBD and spin coating. (a) Fe60 with Ti contributions on the top, annealed at 550+800 ºC (b) Fe150 with Ti contributions on the top, annealed at 550+800 ºC (C) Fe60 with Ti contributions, annealed at 550+800 ºC (d) Fe thickness variation with Ti spin coated on the top and annealed at 550+800 ºC.

Composition	2θ (104) Peak	2θ (110) Peak	I (104) / I (110)
Fe60	33.36	35.84	1.12
Fe60/Ti5	33.28	35.76	1.06
Fe150	33.36	35.84	1.12
Fe150/Ti5	33.24	35.66	1.08
Fe60/S.C.	33.34	35.82	1.69
Fe150/S.C.	33.28	35.70	1.22
S.C./Fe150	33.26	35.70	1.20

TABLE 5.5: XRD 2θ peak position for the hematite main peaks and the corresponding their relative intensities. Thin films annealed at 550 + 800 ºC.

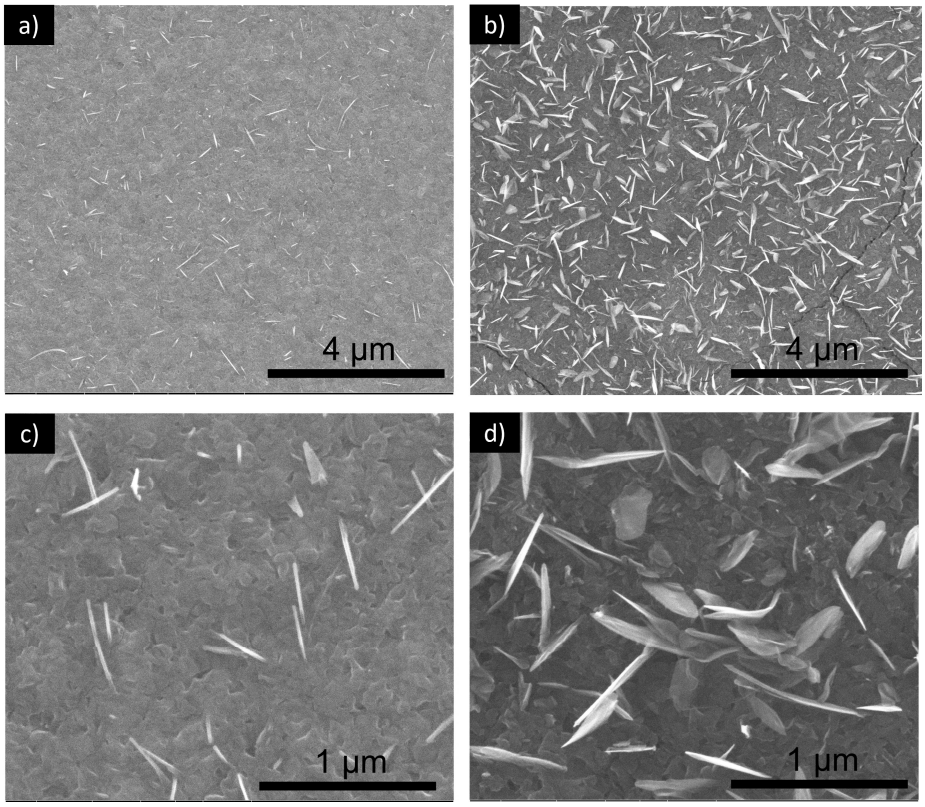


FIGURE 5.14: SEM image of thin films surface morphology with variation on Fe thickness with spin coating deposition of Ti. (a, c) Fe60/S.C. annealed at 550+800 ºC (b, d) Fe150/S.C. annealed at 550+800 ºC.

5.2.2 Photoelectrochemical performance

Among the photoanodes with a Ti layer deposited through a spin coating method, the photoelectrochemical performance at 1.45V vs RHE revealed to be better for photoanodes based on Fe (60 nm) with the Ti spin coated at the top (Table 5.6 and Figure 5.15).

For back illumination, the best performance was achieved when the radiation focused first on the titanium layer, as it was observed in the previous studies. For thinner photoanodes, the photocurrent density decayed on back measurements.

Comparing the samples SC/Fe150 with Ti/Fe150 configuration obatined by IBD, the spin coating produced better photocurrents (Figure 5.16 (a)). On back illumination measurements the spin coated Ti presented a slight improvement in comparison with the Ti5/Fe150 configuration and a considerable increase on the remaining configurations deposited by IBD (Figure 5.16 (b)).

On photoanodes based on 60 nm of Fe, when compared with the Ti deposited through IBD, spin coated Ti at the top of Fe, did not express an enhancement on the photocurrent, neither on front or back illumination measurements (Figure 5.16 (c, d)).

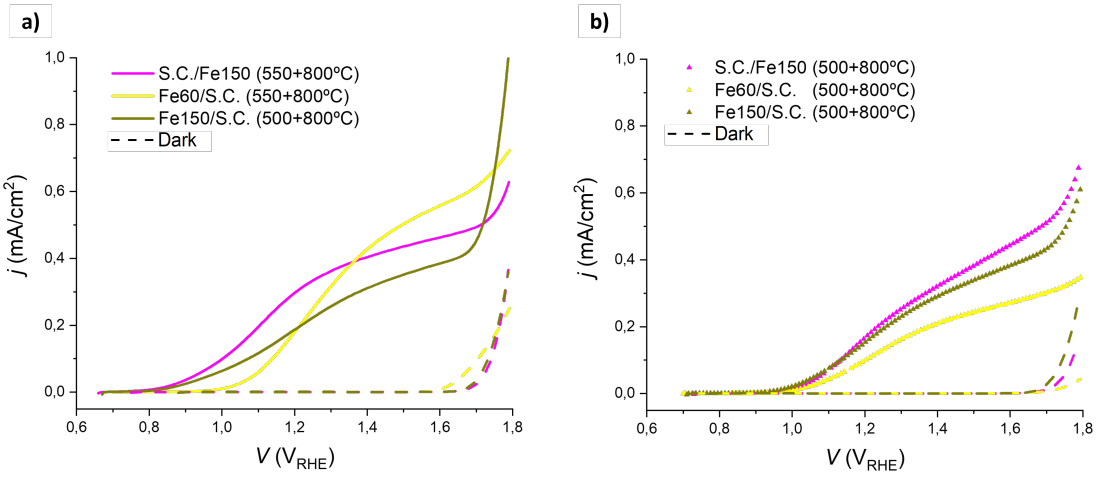


FIGURE 5.15: j-V curves of Fe photoanodes enhanced with a Ti layer deposited through spin coating deposition (a) Front illumination, (b) Back illumination.

Composition	Current density (mA/cm^2)
Fe60/S.C.	0.47
Fe150/S.C.	0.33
S.C./Fe150	0.42

TABLE 5.6: Current density at a 1.45V vs RHE, on Fe photoanodes with a Ti layer deposited through spin coating

In contradiction with the results obtained for samples deposited fully by IBD, the Ti at the top of Fe thin films did not improve the photoresponse. A possible cause for this unexpected result could be the high annealing temperatures that affected the Ti solution.

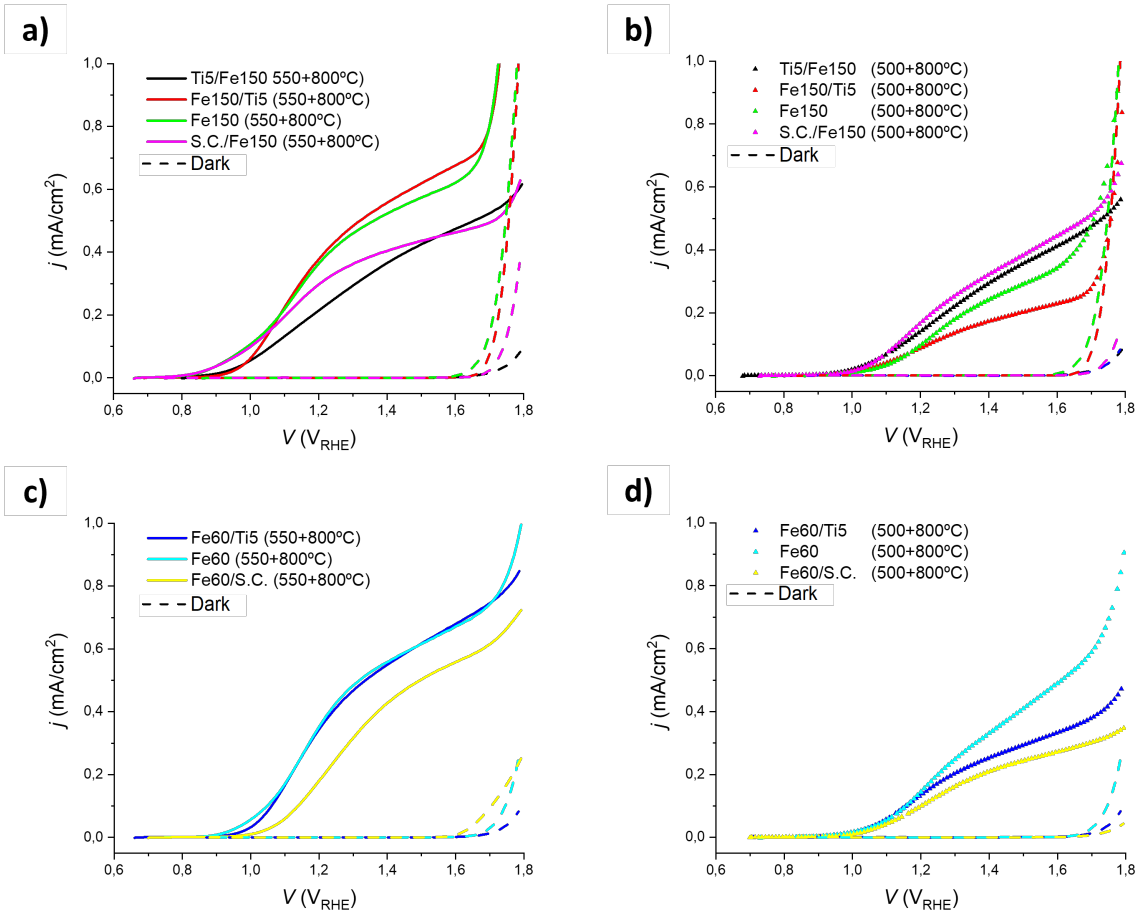


FIGURE 5.16: j-V curves comparison between Fe photoanodes enhanced with a Ti layer deposited through spin coating deposition or by IBD, on Fe150 photoanodes (a) Front illumination, (b) Back illumination. Comparison on Fe60 thin films with the Ti layer addition (c) Front illumination (d) Back illumination.

5.3 Improvement of the photoanodes photoresponse by FeCo oxide based co-catalyst

Co-catalysts on photoanodes can improve the photocurrent and negatively shift the onset potential by decreasing the activation energy [10], enhancing the PEC cell performance. $FeCo_2O_4$ is a co-catalyst, although not much explored for PEC cells applications, can be applicable in devices for water splitting [86–88].

For the first time, as far as we know, this catalyzer, in the optimized stoichiometry of Fe10-Co90, produced an enhancement on the photoelectrochemical process of water splitting.

The catalyzer was deposited through a DC electrodeposition method, which consists in a voltage application between the cathode (PEC photoelectrode) and the anode (Pt

mesh) while all the system is immersed on an ionic electrolyte with the metallic ionic species (in this case Fe and Co). The applied potential drives the metallic ions for the PEC photoelectrode, where they are electrochemically reduced, resulting in the growth of the metallic material on the top of PEC cell.

The reduction equation of the metallic ions can be, generally expressed as:

$$(M_xW_y)^z + nxe \rightarrow xM^0 + yW \tag{5.1}$$

where M is the metallic ion and W is a molecule, ion or radical bounded to M, both forming the complex species $(M_xW_y)^z$, n represents the amount of electrons involved in the reaction.

The electrodeposition of a single metallic atom, requires n electrons, corresponding to a charge of $n * e$ Coulombs. By measuring the amount of current (I) flowing through the circuit, it is possible to estimate the net charge (Q) used to reduced the metal ions. This process follows the Faraday's law of electrolysis, thus the deposited metal mass (m, in g) can be estimated using the following expression:

$$m = \frac{QM}{nF} \tag{5.2}$$

where M is the atomic weight of the metal and F is the Faraday's constant (96485 C mol^{-1}). Through this approach, is possible to estimate the thickness of metal material deposited by the density.

The DC electrodeposition occurred at -1.8 V vs Ag/AgCl and resorted in the combination of 0.16 M $FeSO_4 * 7H_2O$, 0.02 M $CoSO_4 * 7H_2O$, 0.16 M H_3BO_3 and 0.06 M $C_6H_8O_6$. After the process, the photoanodes were submitted to an annealing at 550 ºC for 120 minutes .

The application of FeCo in the optimized stoichiometry, with a estimated thickness of 37 nm. In a hematite photoanode of 150 nm that was annealed with 550 ºC, the obtained photocurrent was 0.17 mA/cm^2, after applying the FeCo co-catalyst the photocurrent achieved values in order of 0.28 mA/cm^2 at 1.45V vs RHE (Figure 5.17), representing an increasing on the photocurrent output more than 60%. Additionally, the V_{OnSet} was also improved due to the catalyst, suffering a cathodic shift of slight more than 10 mV.

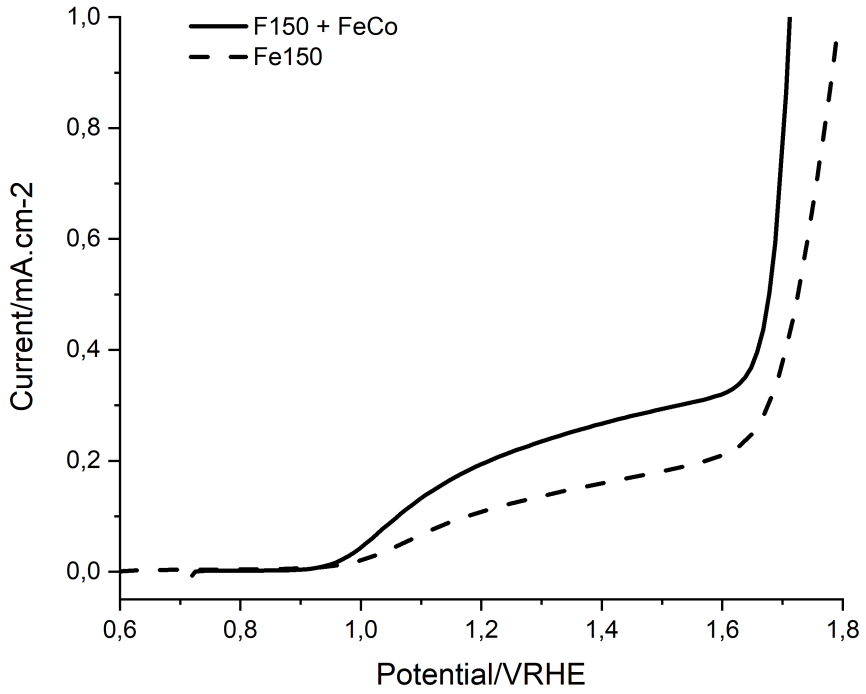


FIGURE 5.17: j-V curves before and after the electrodeposition of FeCo catalyst on Fe 150 nm thin film annealed at 550 ºC.

5.4 Conclusions

Photoanodes with 60 nm of Fe showed better results than 150 nm, due to the fact that for thinner photoanodes shorter charge carrier diffusion paths are reached.

First step annealings at 600 ºC with a second step at 800 ºC, allowed to decrease the Fe thickness while the photocurrent at 1.45 vs RHE was maintained, reducing the material used and the total cost of production.

The decrease on thickness leaded to a decrease on absorbance of the Fe photoanodes, once there was less photo-active material to absorb the incident photons. However, adding a 5nm Ti layer, the photoanode absorption was enhanced, achieving values higher than the thicker (150 nm) hematite photoanodes. This work strategies, relies on thinning (60 nm) the photoanodes (with less material) that with the optimized parameters annealing (600+800 ºC), order and thickness of Ti deposition (surface and 5nm Ti) (from the previous studies,) had led to a photocurrents in order of 0.7 mA/cm^2. Combining the high absorption (due to the Ti layer) and the shortening of charge carrier diffusion path

(due to the reduced thickness), it is possible to enhance the photocurrent output while the production cost of photoanode decreases.

The better photocurrents occurred when Ti was deposited bellow the Fe layer, however, deeper studies are needed to take more solid conclusions about the Ti spin coated influence on the resultant PEC cells.

The introduction of the catalyst produced an improvement of more than 60% on the photocurrent at 1.45V vs RHE and on the V_{OnSet}, being a promising technique to enhance the efficiency of the PEC cells.

Chapter 6

Nanostructured anodic hematite-titanium dioxide photoanodes

This chapter is presented the anodization process of the photoanodes, in order to overcome the semiconductors oxides disadvantages by nanostructuring their morphology to increase the photoactive surface area for both, the occurrence of water splitting reactions, and the absorbed photons. In particular, in order to compare the 2D planar thin films morphology with a 1D nanoporous one, equivalent photoanodes were prepared as the ones prepared in the previous chapters (Fe and Ti thin films double-layers). These samples were then anodized to grow an anodic nanoporous oxide of both doubles layers. Afterwards an thermal annealing with different temperatures was performed.

6.1 Anodization advantages

As explained in the Introduction (Chapter 1), the nanostructuration of photoanodes can significantly reduce the main disadvantages presented by the semiconductors oxides, such hematite or TiO_2. Photocurrent contributions depend on the fraction of photogenerated hole that reach the interface semiconductor/electrolyte [10]. Nanostructures such 1D nanowires or nanopores/nanotubes leads overcomes several limitations presented for these semiconductors, such as, shortening the path for charge carriers to the semiconductor/electrolyte interface [34, 44], increasing the active area and in some morphologies can lead to the light trapping [44], increasing the overall absorbance.

6.2 Anodization experiments

Thin films of Fe and Ti (150 nm and 300 nm) were anodized individually at 60, 50 and 40 V, in order to determine the respective anodization rates. The high anodization rates presented on Fe thin films anodized at 60 and 50V, lead to an extremely fast anodization process, undesirably exposing the FTO substrate.

In order to have a higher control over the anodization process and avoiding the complete anodization, the anodization rates on Fe and Ti were calibrated for potentials at 40 V.

Figure 6.1 shows the different anodizations for the Fe and Ti films, with varying anodization potentials. It is possible to observe a very characteristic curve for Ti thin films anodized at the same potential, however the anodization of Fe thin films leads to hardly reproducible anodization curves.

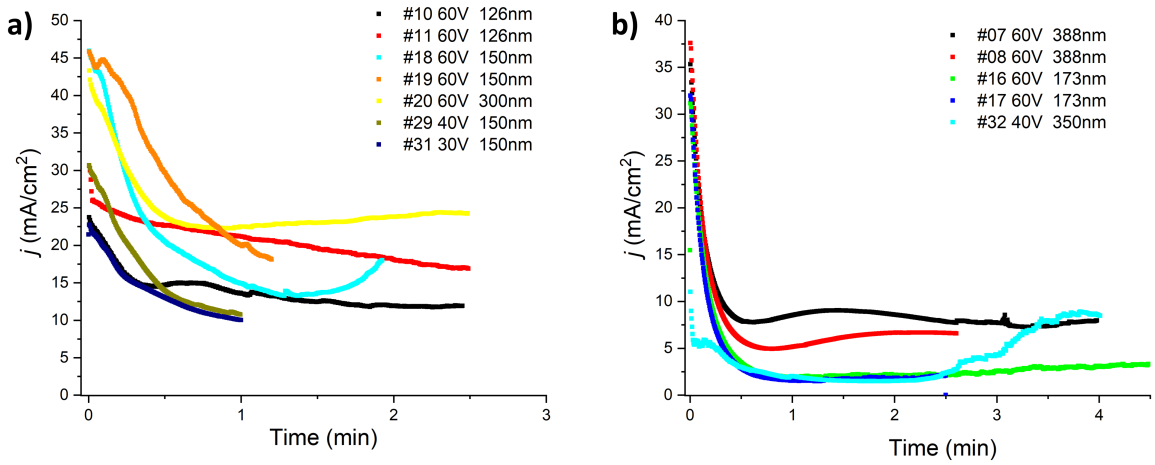


FIGURE 6.1: Electrochemical anodization curves of thin films of (a) Iron (b) Titanium at different potentials, thicknesses and time duration .

To avoid the complete anodization of the double layer thin films, electrochemical anodization was performed at 40 V with anodization times depending on the different material anodization rates and their thickness (Table 6.1). The anodizations for each configuration are showed on Figure 6.2.

The photoanodes Fe/Ti thin films double-layers post anodization, were then annealed at different temperatures 550 ºC (and second step 800 ºC). The photoanodes of Fe 150 annealed at 550 ºC, showed improved photocurrents (0.14 mA/cm^2) for front-illumination

Composition	Anodization time (seconds)
Fe150	60
Fe150/Ti5	62
Fe150/Ti50	72
Ti50/Fe150	72

TABLE 6.1: Anodization times for the different double layer thin films compositions.

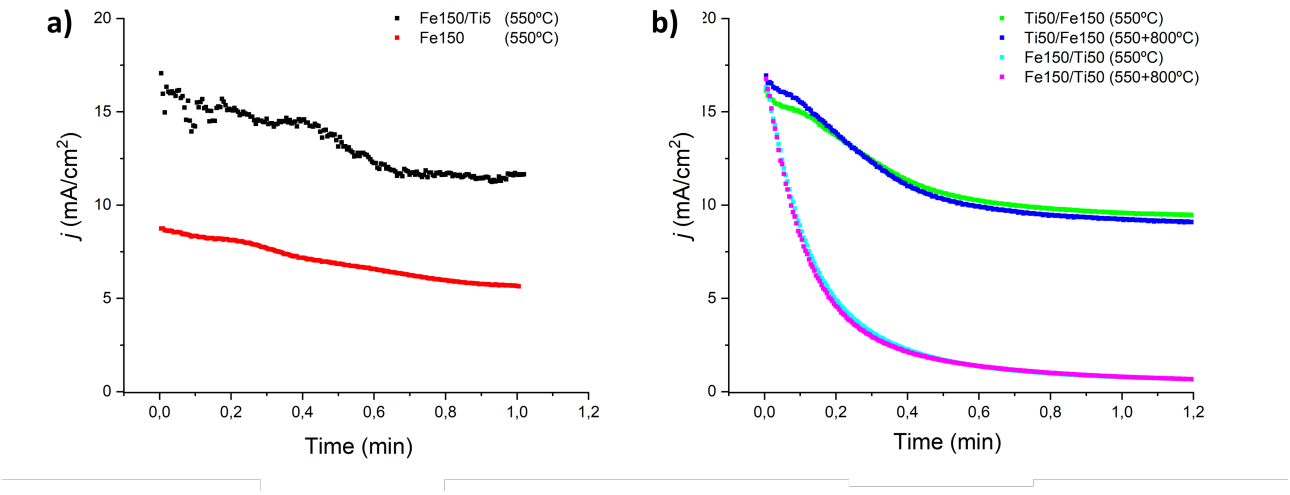


FIGURE 6.2: Electrochemical anodization curves of Fe and Ti thin films double-layers for (a) Fe150 and Fe150/Ti5 (b)Fe150/Ti50 and Ti50/Fe150.

when compared with the 2D thin film configuration (0.08 mA/cm^2), representing an increase of 75 %. Furthermore, the values for Fe150 presented an increase of 200 % on back illumination measurements. For the sample Fe150/Ti5, the one with anodization showed a photocurrent 4 times higher than without anodization (for back illumination)(Figure 6.3).

The outstanding increases on the back illumination photocurrent of nanostructured photoanodes, corroborates the positive influence of nano features, decreasing the needed travelling path for the minority charge carriers and consequently the e-h recombination rates.

Figure 6.4 shows the morphological changes on the photoanodes after the electrochemical anodization. On Fe150 the current density of anodization was lower than in Fe150/Ti5, corresponding to lower amounts of transferred charge and consequently a smoother anodizations, where is only possible to observe an decreasing on the ribbon shape features at the surface and the beginning of the nanostructuration (Figure 6.4(a)).

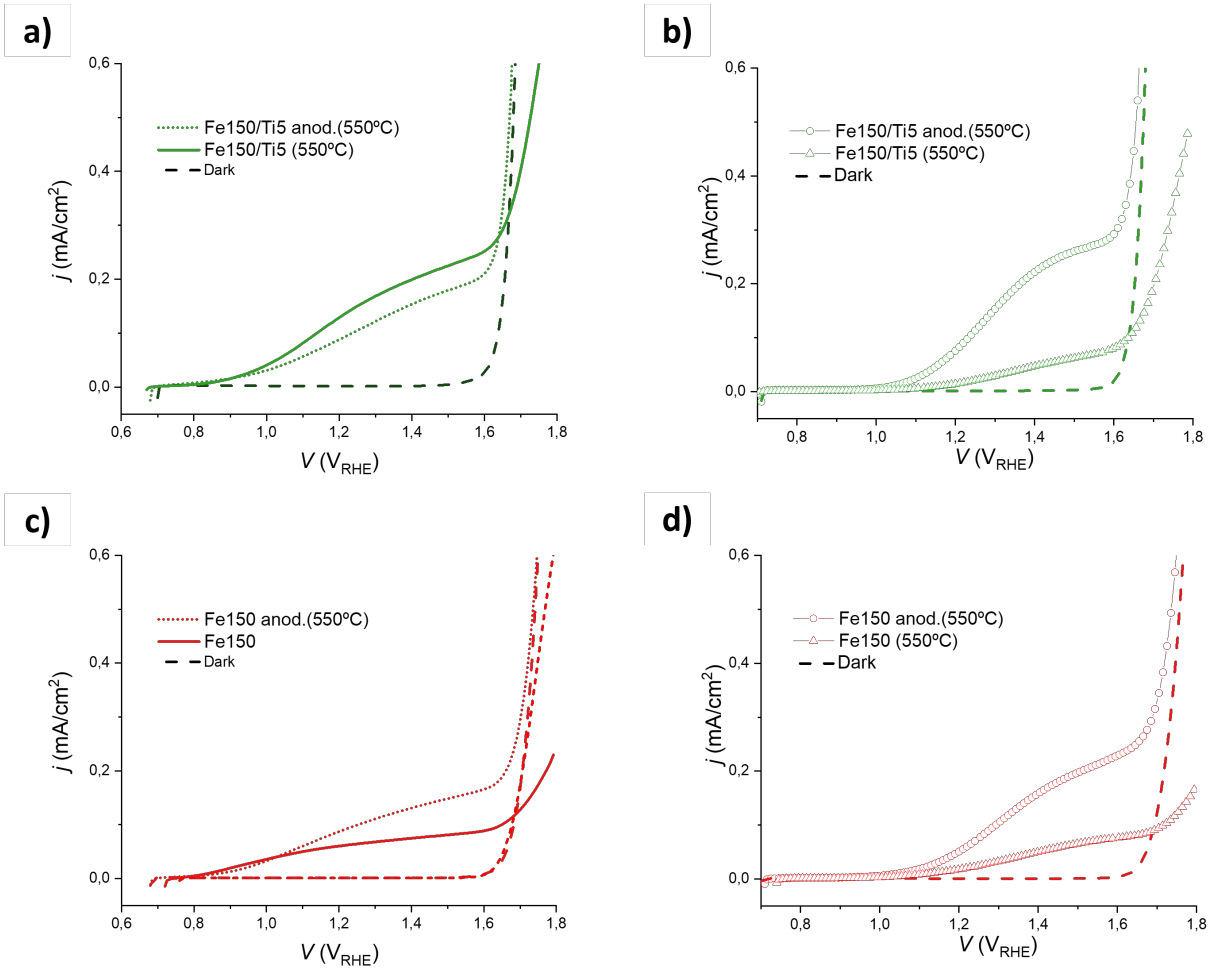


FIGURE 6.3: j-V curves comparison between anodized and non anodized Fe photoanodes (a) Front illumination (b) Back illumination; and with the addition of a 5nm Ti layer (c) Front illumination (d) Back illumination. All the films were annealed at 550 ºC for 2h.

With higher charge values transferred during the anodization of Fe150/Ti5, the final morphology presented nanoporous oxide (Figure 6.4(b)), shortening the path for the minority charge carriers and enhancing the photocurrent outputs.

Composition	Current density (mA/cm^2)	Current density (mA/cm^2) (back illumination)
Anod. Fe150	0.14	0.18
Anod. Fe150/Ti5	0.17	0.24
Fe150	0.08	0.06
Fe150/Ti5	0.21	0.06

TABLE 6.2: Current density at a 1.45V vs RHE, on (a, b) Fe/Ti and (c, d) Fe photoanodes.

Due to the volume expansion of anodic iron oxide, showed on Figure 6.4 (a), to form nanostructured features, some bubble shape zones were produced on Fe thin films (Figure

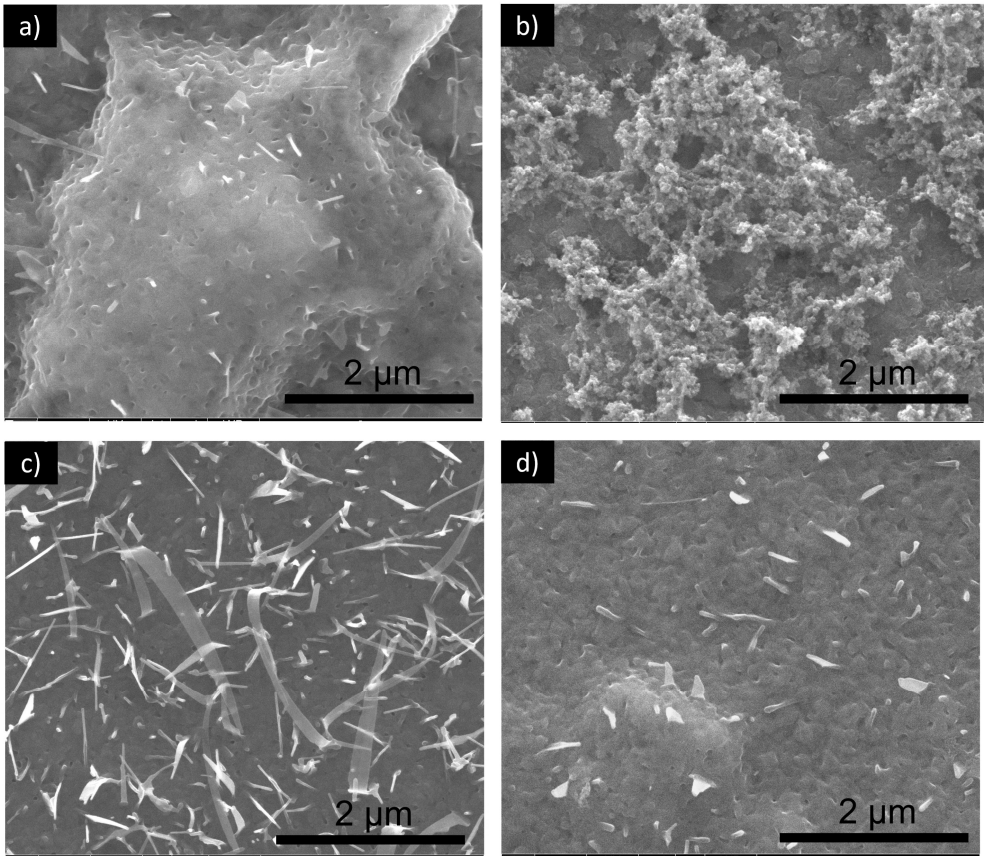


FIGURE 6.4: Anodized thin films (Top) of (a) Fe150 (b) Fe150/Ti5, compared with the non anodized ones (Bottom) (c) Fe150 (d) Fe150/Ti5. All the films were annealed at 550 ºC.

6.5(a)), corresponding to an oxide accumulation, producing roughness on the photoanode and increasing the effective area. Despite of the formation of nanostructures, on Fe150/Ti5 thin film it was observed residual zones of boards where the FTO was exposed (Figure 6.5(b)), decreasing the photoanode active area and the overall efficiency of the cell.

Thicker thin films with 150Fe/50Ti, after anodization and annealing (independently of the conditions), produced better outputs when the Ti layer was on the top of Fe, independently of front or back illumination (Figure 6.7). However when compared with non anodized photoanodes, their photocurrent decreased. The high temperature step, reduced the photocurrent obtained (Figure 6.6) in all the cases. The anodization of thin films with thicker Ti layers did not presented promising photocurrent values, independently of the annealing conditions or the photoanode nanostructuration.

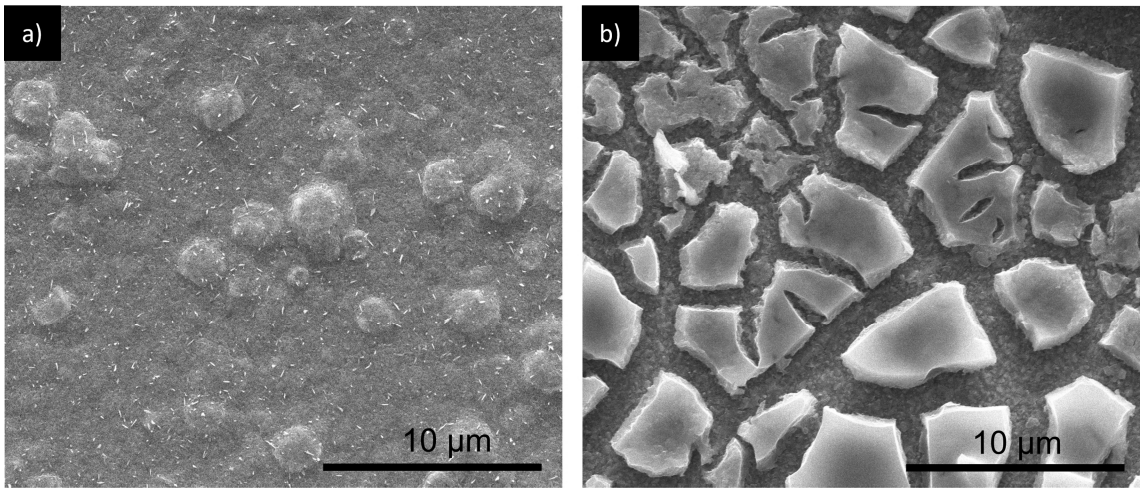


FIGURE 6.5: SEM images after anodization, presenting (a) recurrent bubble zone formation on Fe150 thin films and (b) residual board zones on Fe150/Ti5 thin films. Both films were annealed at 550 ºC

Composition	Current density (mA/cm^2)	Current density (mA/cm^2) (back illumination)
Anod. Fe150/Ti50 (550 ºC)	0.18	0.10
Anod. Fe150/Ti50 (550+800 ºC)	0.10	0.08
Anod. Ti50/Fe150 (550 ºC)	0.06	0.06
Anod. Ti50/Fe150 (550+800 ºC)	0.01	0.02
Ti50/Fe150 (550 ºC)	0.05	0.03
Ti50/Fe150 (550+800 ºC)	0.02	0.01
Fe150/Ti50 (550 ºC)	0.20	0.13
Fe150/Ti50 (550+800 ºC)	0.19	0.15

TABLE 6.3: Current density at a 1.45V vs RHE, on Fe photoanodes with a Ti 50 nm layer, with and without anodization.

For Ti50/Fe150 configurations, the anodization led to the formation of compact bubble zones (Figure 6.8 (b)). As seen in the previous chapters, the anodization decreased the number of features at the surface as well as their apparent length (Figure 6.8).

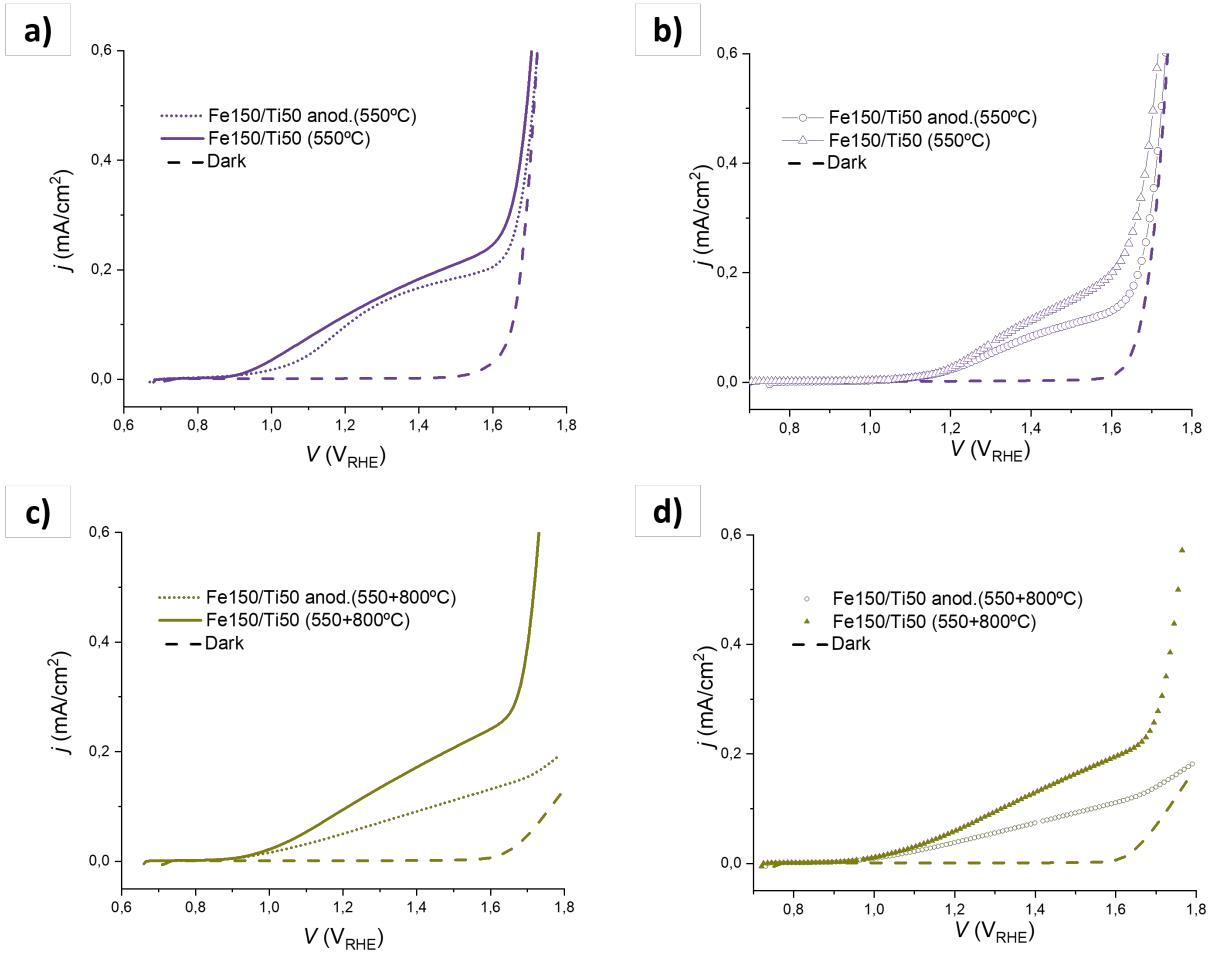


FIGURE 6.6: j-V curves comparison between anodized and non anodized Fe150/Ti50 thin films(a) Front illumination (b) Back illumination; and Ti50/Fe150 thin film (c) Front illumination (d) Back illumination.

For the Ti (50 nm) layers at the top of 150 nm of Fe, the Fe features only appears when the thin films are anodized and annealed at a low temperature (Figure 6.9 (b)).

On an overview, when the 50 nm Ti layer was on the top of the film, the surface acquired a more unevenness morphology, with several burst bubbles that can be assigned to the oxide expansion and to the faster anodization of the Fe layer bellow that forced the volume expansion. On Figure 6.10 (b), the open zone was identified through EDS as Fe while the upper layer corresponds to Ti (Appendix). This behaviour led to us to believe that are some adhesion problems on the Fe-Ti interface, even for the thin films with lower thickness of deposited Ti.

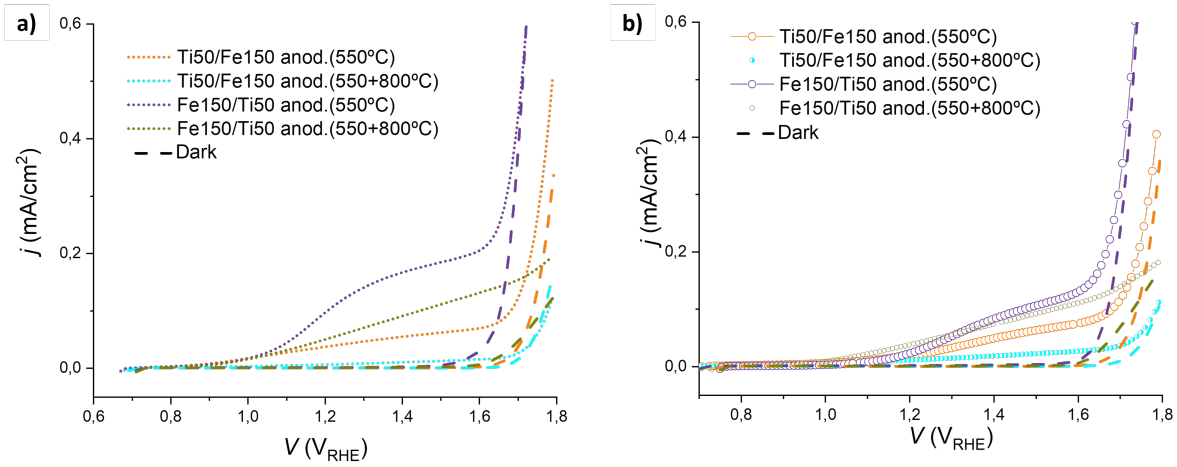


FIGURE 6.7: j-V curves comparison between anodized Fe150/Ti50 and Ti50/Fe150 thin films(a) Front illumination (b) Back illumination.

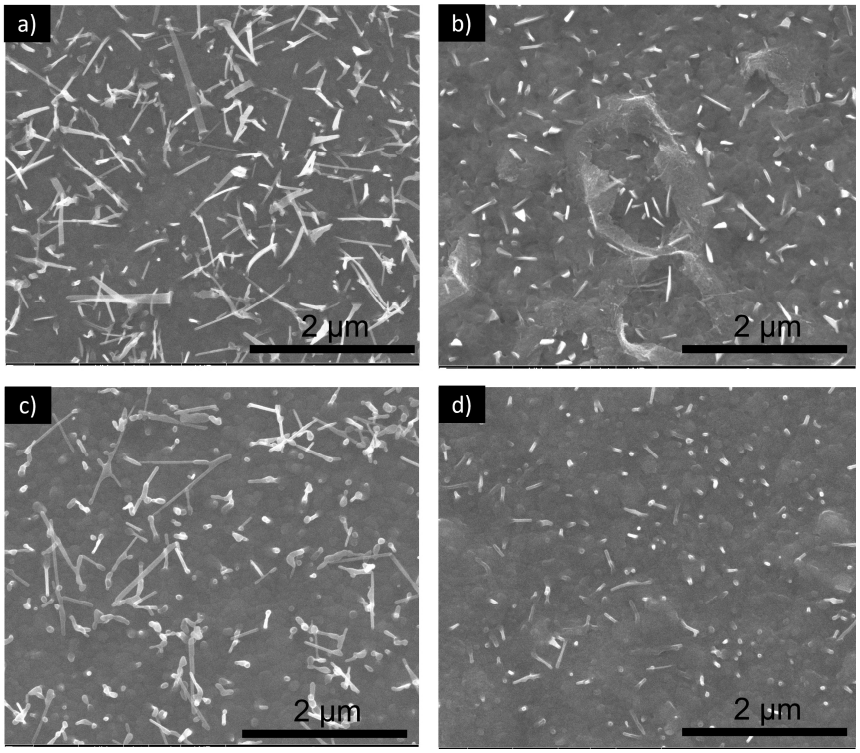


FIGURE 6.8: Non anodized thin films (Left) of Ti50/Fe150 (a) annealed at 550 ºC (c) annealed at 550+800 ºC and the respective anodization (right)with annealings at (c) 550 ºC (d) 550+800 ºC.

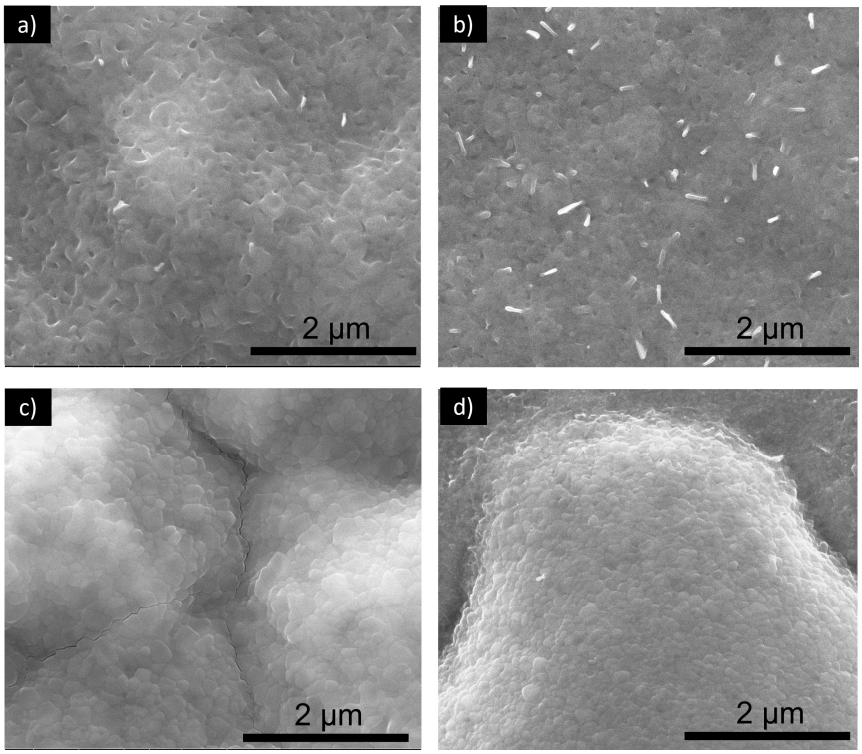


FIGURE 6.9: Non anodized thin films (Left) of Fe150/Ti50 (a) annealed at 550 ºC (c) annealed at 550+800 ºC and the respective anodization (right) with annealings at (c) 550 ºC (d) 550+800 ºC.

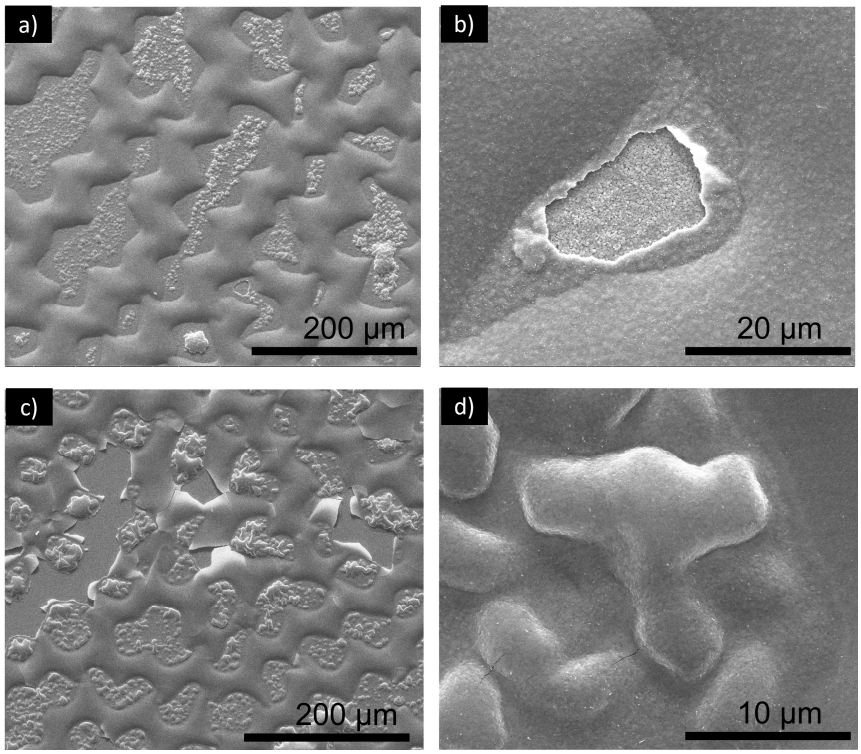


FIGURE 6.10: Surface morphological characteristics of anodized Fe150/Ti50 thin films (a,b) annealed at 550 ºC (c,d) annealed at 550+800 ºC.

6.3 Conclusions

The nanostructuration of photoanodes led to photocurrent improvement on Fe150 and Fe150/Ti5 photoanodes for back illumination measurements. On the previous chapters, back illumination presented lower photocurrents when compared with front illumination measurements due to the long diffusion path for the holes that are photogenerated near the FTO interface. On the other hand, the anodization produced the size reduction, nanostruturing the materials morphology, an thus, shortening the paths for the holes to react with the electrolyte, as well as increasing the photoanode surface area, ultimately leading to an increase of the absorption coefficient. An improvement of the photocurrent from 0.06 to 0.24 mA/cm^2 at 1.45 vs RHE was observed for Fe150/Ti5 nm films to Fe150/Ti5 nm anodized, respectively, representing an percentage increase of 200%.

Despite the improvements of anodized photoanodes with thinner Ti layers, when the Ti thickness increases, the achieved photocurrent decreases. This happens due to a high concentration of Ti that produces intermediate energy levels, limiting the photoresponses.

The anodization of Fe thin films involves a very complex process, where further studies need to be performed. Despite the astonishing relative increases on the photocurrent, the process of anodization needs more optimizations due to the different anodization rates of Fe and Ti, that could lead to film damaging.

Chapter 7

General Conclusions and future perspectives

7.1 Main Conclusions

In this work, we perform photoanodes based on double-layers of hematite/TiO_2 (and opposite order) by the Fe/Ti (and opposite order) thin film depositions with Ion Beam Deposition for PEC cells and H_2 generation.

Studies of the annealing conditions optimization have revealed that for thicker photoanodes ($\geq$ 150nm), the low-temperature annealing at 550 ºC led to improved photocurrents when compared with the one at 600 ºC. Decreasing the photoanodes thickness, an inversion of the photoanodes efficiency occurred, where the annealing at 600 ºC generated the best photocurrent output.

It was studied and concluded that the best arrangement for the Ti layer (5 nm) in the hematite photoanodes was at the top, producing a 0.21 mA/cm^2 on low temperature annealings and 0.60 mA/cm^2 at two-step annealings with a high temperature step, at 1.45V vs RHE. These results were further corroborated by the analysis of thinner hematite and TiO_2 photoanodes, where the incorporation of Ti at the surface leaded to the highest photocurrents presented at this work, $\approx$ 0.7 mA/cm^2 at 1.45V vs RHE.

By decreasing the layer of hematite (maintaining a thinner layer of TiO_2 at the surface), it was possible shortening the hole diffusion path, reducing the recombination rates as well as increasing the absorbance. It was found that increasing the thickness of Ti from 5 nm to 50 nm led to a photocurrent decrease.

We believe that the bulk properties are modified by the Ti addition, which also produces modifications on the i-SS surface state properties, resulting in an undesirable anodic shift on the onset potential. However, the presence of Ti above a threshold, produces considerable recombination sites that decrease the photocurrent output.

Additionally, an high temperature annealing of 800 ºC provided the diffusion of Sn from the FTO into the hematite lattice, which produced modifications on the optical properties, studied by UV-Vis measurements, revealing that the maximum absorption peak had a red- shift (higher wavelengths).

Further approaches to improve the PEC performance was the use of co-catalysts of FeCo oxide, with optimized stoichiometry that proved to increase the photocurrent for more than 60% on hematite based photoanodes as well as produced a approximately 10 mV cathodic shift on the Onset potential.

Additionally, we perform another strategy to improve the photoresponse. The anodization of the photoanodes, although not fully optimized, revealed astonishing photocurrent values with an increase of 200% for Fe 150 nm / Ti 5 nm photoanodes.

Both these results, adding the co-catalyst (FeCo oxide) and nanostructuring the hematite/-TiO2 planar thin films (by anodization) stands as two key-strategical features to the route of achieving efficient photoanodes with improved photoresponses. However the main focus should be the bulk properties modification, in order to retard the electron-hole recombination or accelerate their extraction through the external circuit.

Spin coated Ti layers, revealed to produce less influences on the hematite structures as well as interesting photocurrent results, however to produce more solid conclusions about their influence it is needed deeper studies.

7.2 Future perspectives

The enhancement of hematite photoanodes through nanostructuration or heterojunctions presented astonishing outputs. Due to these results, the future work is focused on the enhancement of hematite photoanodes through improvements on bulk charge transport properties. To study in depth the effects of Ti incorporation, it is programmed for future work the deposition of Ti layers on the top of Fe, with thicknesses varying around 5nm. After Ti thickness optimization, it is expected the deposition of Ti and Fe multi-layers , in order to enhance the separation of photogerenated electron-hole pairs, increasing the number of charge carriers on water oxidation and reduction processes.

The performance of photoanodes was enhanced by the thin films electrochemical anodization, however for low Ti thicknesses, it was only studied under low temperature annealings (550 ºC). For future work it is expected the anodization of photoanodes with the second step strategies (800 ºC). The anodization of Fe is also a parameter to be optimized as well as the anodization of Ti and Fe thin film compositions, this approach can be very complex due to the distinct material behaviours under anodization.

Further studies should rely on a deeper analysis of the obtained XRD data, refining the difractograms in order to obtain the lattice parameters, identifying some possible peak overlaps, and searching for the Ti structural modifications in all of the peaks, instead of the hematite two major peaks.

Through UV-Vis data, it is also important to obtain the photoanodes bandgap, resorting on the Tauc plots analysis [89], and study its tuning due to the nanostructuration of the photoanode as well as with the possible incorporation of Ti into the lattice.

The improvements promoted by the use of a FeCo co-catalyst in an optimized stoichiometry, enhanced significantly the photocurrent outputs whereby the FeCo should be applied on the photoanodes for two step annealings at 800 ºC .

This thesis approached almost all the possible methods to enhance the photocurrent outputs of PEC cells. Resorting in the relative increases produced by each one of the methods and by the obtained photocurrent curves, we estimate that the simultaneous application of all the approaches, should lead to a photocurrent in range of $1.1 mA/cm^2$ at 1.45V vs RHE.

The introduction of Ti through spin coating, was projected due the Annamalai et al [65] reports, focused on the deposition of a Ti layer at the interface with the FTO. To consolidate the Ti atoms after the Ti solution deposition, it was reported the heating of the thin film to 250ºC for 30min. This procedure was rigorously followed when the spin coated Ti solution was deposited at the FTO interface, however when the Ti was deposited at the surface, the heating step was substituted by the usual annealings performed on the other samples (this happened due to the necessary temperatures to convert the Fe into hematite). This change on the Ti solution treatment could leaded to unwanted transformations that effected their properties and consequently degraded their performance. In the future work, for deeper understanding of the spin coated Ti influence, an interesting approach is to, anneal the Fe thin film before the deposition of Ti, deposit the Ti layer and then heat the composition at 250 ºC for 30 min. Due to technical issues, it was not possible

to produce a S.C./Fe60 sample to analyse and compare with the produced samples. On latter work, it was expected to deposit that configuration to complete the sample group and consolidate the conclusions.

Appendix A

Sample list

Sample	Composition (nm)	Annealing (ºC)	Anodization
01	Ti(5)Fe(150)	550	No
02	Ti(5)Fe(150)	600	No
03	Ti(5)Fe(150)	550	Yes
04 *	Ti(5)Fe(150)	550 + 800	No
05	S.C.Fe(150)	550	Yes
06 *	S.C.Fe(150)	550 + 800	No
07	Fe(150)Ti(5)	550	No
08	Fe(150)Ti(5)	600	No
09	Fe(150)Ti(5)	550	Yes
10 *	Fe(150)Ti(5)	550 + 800	No
11	Fe(150)	550	No
12	Fe(150)	600	No
13	Fe(150)	550	Yes
14 *	Fe(150)	550 + 800	No
15	Ti(50)Fe(150)	550	No
16	Ti(50)Fe(150)	550	Yes
17 *	Ti(50)Fe(150)	550 + 800	No

Sample	Composition (nm)	Annealing (ºC)	Anodization
18 *	Ti(50)Fe(150)	550 + 800	Yes
19	Fe(150)Ti(50)	550	No
20	Fe(150)Ti(50)	550	Yes
21 *	Fe(150)Ti(50)	550 + 800	No
22 *	Fe(150)Ti(50)	550 + 800	Yes
23	Fe(60)Ti(5)	550	No
24	Fe(60)Ti(5)	600	No
25 *	Fe(60)Ti(5)	550 + 800	No
26 *	Fe(60)Ti(5)	600 + 800	No
27	Fe(60)	550	No
28	Fe(60)	600	No
29 *	Fe(60)	550 + 800	No
30 *	Fe(60)	600 + 800	No

TABLE A.1: Characteristics of the deposited samples by IBD and spin coating; (*) represents the high temperature FTO 10-10 [61], while unmarked samples were deposited in a low temperature FTO 22-7 [60]

Bibliography

[1] T. Lopes, P. Dias, L. Andrade, and A. Mendes, "An innovative photoelectrochemical lab device for solar water splitting," *Solar Energy Materials and Solar Cells*, vol. 128, pp. 399–410, 2014. [Online]. Available: https://www.sciencedirect.com/science/article/pii/S0927024814003225

[2] M. Gratzel, "Photoelectrochemical cells," *Nature*, vol. 414, no. 6861, pp. 338–344, Nov 2001. [Online]. Available: https://doi.org/10.1038/35104607

[3] M. Höök and X. Tang, "Depletion of fossil fuels and anthropogenic climate change—a review," *Energy Policy*, vol. 52, pp. 797–809, 2013, special Section: Transition Pathways to a Low Carbon Economy. [Online]. Available: https://www.sciencedirect.com/science/article/pii/S0301421512009275

[4] S. Shafiee and E. Topal, "When will fossil fuel reserves be diminished?" *Energy Policy*, vol. 37, no. 1, pp. 181–189, 2009. [Online]. Available: https://www.sciencedirect.com/science/article/pii/S0301421508004126

[5] F. E. Osterloh and B. A. Parkinson, "Recent developments in solar water-splitting photocatalysis," *MRS Bulletin*, vol. 36, no. 1, p. 17–22, 2011.

[6] Solargis. Solar resource maps of europe. [Online]. Available: https://solargis.com/maps-and-gis-data/download/europe

[7] J. Y. Kim, G. Magesh, D. H. Youn, J.-W. Jang, J. Kubota, K. Domen, and J. S. Lee, "Single-crystalline, wormlike hematite photoanodes for efficient solar water splitting," *Scientific Reports*, vol. 3, no. 1, p. 2681, Sep 2013. [Online]. Available: https://doi.org/10.1038/srep02681

[8] P. Quitério, A. Apolinário, D. Navas, S. Magalhães, E. Alves, A. Mendes, C. T. Sousa, and J. P. Araújo, "Photoelectrochemical water splitting: Thermal

annealing challenges on hematite nanowires," *The Journal of Physical Chemistry C*, vol. 124, no. 24, pp. 12 897–12 911, 2020. [Online]. Available: https://doi.org/10.1021/acs.jpcc.0c01259

[9] X. Chen and S. S. Mao, "Titanium dioxide nanomaterials: synthesis, properties, modifications, and applications," *Chemical Reviews*, vol. 107, no. 7, pp. 2891–2959, 2007, pMID: 17590053. [Online]. Available: https://doi.org/10.1021/cr0500535

[10] A. G. Tamirat, J. Rick, A. A. Dubale, W.-N. Su, and B.-J. Hwang, "Using hematite for photoelectrochemical water splitting: a review of current progress and challenges," *Nanoscale Horizons*, vol. 1, no. 4, pp. 243–267, 2016.

[11] X. Qi, G. She, X. Huang, T. Zhang, H. Wang, L. Mu, and W. Shi, "High-performance n-si/$\alpha - fe_2o_3$ core/shell nanowire array photoanode towards photoelectrochemical water splitting," *Nanoscale*, vol. 6, pp. 3182–3189, 2014. [Online]. Available: http://dx.doi.org/10.1039/C3NR05429B

[12] N. D. Sankir and M. Sankir, *Photoelectrochemical Solar Cells*. John Wiley & Sons, 2018.

[13] S. Ardo, D. Fernandez Rivas, M. A. Modestino, V. Schulze Greiving, F. F. Abdi, E. Alarcon Llado, V. Artero, K. Ayers, C. Battaglia, J.-P. Becker, D. Bederak, A. Berger, F. Buda, E. Chinello, B. Dam, V. Di Palma, T. Edvinsson, K. Fujii, H. Gardeniers, H. Geerlings, S. M. H. Hashemi, S. Haussener, F. Houle, J. Huskens, B. D. James, K. Konrad, A. Kudo, P. P. Kunturu, D. Lohse, B. Mei, E. L. Miller, G. F. Moore, J. Muller, K. L. Orchard, T. E. Rosser, F. H. Saadi, J.-W. Schüttauf, B. Seger, S. W. Sheehan, W. A. Smith, J. Spurgeon, M. H. Tang, R. van de Krol, P. C. K. Vesborg, and P. Westerik, "Pathways to electrochemical solar-hydrogen technologies," *Energy Environ. Sci.*, vol. 11, pp. 2768–2783, 2018. [Online]. Available: http://dx.doi.org/10.1039/C7EE03639F

[14] E. Verlage, S. Hu, R. Liu, R. J. R. Jones, K. Sun, C. Xiang, N. S. Lewis, and H. A. Atwater, "A monolithically integrated, intrinsically safe, 10% efficient, solar-driven water-splitting system based on active, stable earth-abundant electrocatalysts in conjunction with tandem iii–v light absorbers protected by amorphous tio2 films," *Energy Environ. Sci.*, vol. 8, pp. 3166–3172, 2015. [Online]. Available: http://dx.doi.org/10.1039/C5EE01786F

[15] J. Jia, L. C. Seitz, J. D. Benck, Y. Huo, Y. Chen, J. W. D. Ng, T. Bilir, J. S. Harris, and T. F. Jaramillo, "Solar water splitting by photovoltaic-electrolysis with a solar-to-hydrogen efficiency over 30%," *Nature communications*, vol. 7, no. 1, pp. 1–6, 2016.

[16] J. de Negócios. Évora vai ter produção de hidrogénio verde com tecnologia portuguesa pioneira. [Online]. Available: https://www.jornaldenegocios.pt/empresas/energia/detalhe/evora-vai-ter-producao-de-hidrogenio-verde-com-tecnologia-portuguesa-pioneira

[17] O. Khaselev and J. A. Turner, "A monolithic photovoltaic-photoelectrochemical device for hydrogen production via water splitting," *Science*, vol. 280, no. 5362, pp. 425–427, 1998.

[18] A. Fujishima and K. Honda, "Electrochemical photolysis of water at a semiconductor electrode," *nature*, vol. 238, no. 5358, pp. 37–38, 1972.

[19] G. K. Mor, H. E. Prakasam, O. K. Varghese, K. Shankar, and C. A. Grimes, "Vertically oriented tifeo nanotube array films: toward a useful material architecture for solar spectrum water photoelectrolysis," *Nano Letters*, vol. 7, no. 8, pp. 2356–2364, 2007, pMID: 17608445. [Online]. Available: https://doi.org/10.1021/nl0710046

[20] B. D. Alexander, P. J. Kulesza, I. Rutkowska, R. Solarska, and J. Augustynski, "Metal oxide photoanodes for solar hydrogen production," *J. Mater. Chem.*, vol. 18, pp. 2298–2303, 2008. [Online]. Available: http://dx.doi.org/10.1039/B718644D

[21] K. Sivula, F. LeFormal, and M. Grätzel, "Solar water splitting: Progress using hematite (-fe2o3) photoelectrodes," *ChemSusChem*, vol. 4, no. 4, pp. 432–449, 2011. [Online]. Available: https://chemistry-europe.onlinelibrary.wiley.com/doi/abs/10.1002/cssc.201000416

[22] Y. Ling and Y. Li, "Review of sn-doped hematite nanostructures for photoelectrochemical water splitting," *Particle & Particle Systems Characterization*, vol. 31, no. 11, pp. 1113–1121, 2014.

[23] M. Al-Kuhaili, M. Saleem, and S. Durrani, "Optical properties of iron oxide ($\alpha - fe_2o_3$) thin films deposited by the reactive evaporation of iron," *Journal of Alloys and Compounds*, vol. 521, pp. 178–182, 2012. [Online]. Available: https://www.sciencedirect.com/science/article/pii/S0925838812001879

[24] B. M. Klahr, A. B. F. Martinson, and T. W. Hamann, "Photoelectrochemical investigation of ultrathin film iron oxide solar cells prepared by atomic layer deposition," *Langmuir*, vol. 27, no. 1, pp. 461–468, 2011, pMID: 21126056. [Online]. Available: https://doi.org/10.1021/la103541n

[25] Z. Li, W. Luo, M. Zhang, J. Feng, and Z. Zou, "Photoelectrochemical cells for solar hydrogen production: current state of promising photoelectrodes, methods to improve their properties, and outlook," *Energy Environ. Sci.*, vol. 6, pp. 347–370, 2013. [Online]. Available: http://dx.doi.org/10.1039/C2EE22618A

[26] Y. Lin, G. Yuan, S. Sheehan, S. Zhou, and D. Wang, "Hematite-based solar water splitting: challenges and opportunities," *Energy Environ. Sci.*, vol. 4, pp. 4862–4869, 2011. [Online]. Available: http://dx.doi.org/10.1039/C1EE01850G

[27] F. Francisco, P. Dias, D. Ivanou, F. Santos, J. Azevedo, and A. Mendes, "Synthesis of host-guest hematite photoelectrodes for solar water splitting," *ChemNanoMat*, vol. 5, no. 7, pp. 911–920, 2019.

[28] S. D. Tilley, M. Cornuz, K. Sivula, and M. Grätzel, "Light-induced water splitting with hematite: improved nanostructure and iridium oxide catalysis," *Angewandte Chemie International Edition*, vol. 49, no. 36, pp. 6405–6408, 2010.

[29] Y. W. Phuan, W.-J. Ong, M. N. Chong, and J. D. Ocon, "Prospects of electrochemically synthesized hematite photoanodes for photoelectrochemical water splitting: A review," *Journal of Photochemistry and Photobiology C: Photochemistry Reviews*, vol. 33, pp. 54–82, 2017. [Online]. Available: https://www.sciencedirect.com/science/article/pii/S1389556717300771

[30] A. Kay, I. Cesar, and M. Grätzel, "New benchmark for water photooxidation by nanostructured $\alpha - fe_2o_3$ films," *Journal of the American Chemical Society*, vol. 128, no. 49, pp. 15 714–15 721, 2006, pMID: 17147381. [Online]. Available: https://doi.org/10.1021/ja064380l

[31] K. Sivula, R. Zboril, F. Le Formal, R. Robert, A. Weidenkaff, J. Tucek, J. Frydrych, and M. Grätzel, "Photoelectrochemical water splitting with mesoporous hematite prepared by a solution-based colloidal approach," *Journal of the American Chemical Society*, vol. 132, no. 21, pp. 7436–7444, 2010, pMID: 20443599. [Online]. Available: https://doi.org/10.1021/ja101564f

[32] H. Wang and J. A. Turner, "Characterization of hematite thin films for photoelectrochemical water splitting in a dual photoelectrode device," *Journal of The Electrochemical Society*, vol. 157, no. 11, p. F173, 2010. [Online]. Available: https://doi.org/10.1149/1.3489940

[33] Z. Najaf, D. L. T. Nguyen, S. Y. Chae, O.-S. Joo, A. U. H. A. Shah, D.-V. N. Vo, V.-H. Nguyen, Q. V. Le, and G. Rahman, "Recent trends in development of hematite (-fe2o3) as an efficient photoanode for enhancement of photoelectrochemical hydrogen production by solar water splitting," *International Journal of Hydrogen Energy*, vol. 46, no. 45, pp. 23 334–23 357, 2021, hydrogen Separation, Production and Storage. [Online]. Available: https://www.sciencedirect.com/science/article/pii/S0360319920326860

[34] A. Mao, K. Shin, J. K. Kim, D. H. Wang, G. Y. Han, and J. H. Park, "Controlled synthesis of vertically aligned hematite on conducting substrate for photoelectrochemical cells: Nanorods versus nanotubes," *ACS Applied Materials & Interfaces*, vol. 3, no. 6, pp. 1852–1858, 2011, pMID: 21557610. [Online]. Available: https://doi.org/10.1021/am200407t

[35] D. A. H. Hanaor and C. C. Sorrell, "Review of the anatase to rutile phase transformation," *Journal of Materials Science*, vol. 46, no. 4, pp. 855–874, Feb 2011.

[36] S.-D. Mo and W. Y. Ching, "Electronic and optical properties of three phases of titanium dioxide: Rutile, anatase, and brookite," *Phys. Rev. B*, vol. 51, pp. 13 023–13 032, May 1995. [Online]. Available: https://link.aps.org/doi/10.1103/PhysRevB.51.13023

[37] A. Riaz, H. Qi, Y. Fang, J. Xu, C. Zhou, Z. Jin, Z. Hong, M. Zhi, and Y. Liu, "Enhanced intrinsic photocatalytic activity of tio_2 electrospun nanofibers based on temperature assisted manipulation of crystal phase ratios," *Journal of Materials Research*, vol. 31, no. 19, pp. 3036–3043, 2016.

[38] K. M. Glassford and J. R. Chelikowsky, "Structural and electronic properties of titanium dioxide," *Phys. Rev. B*, vol. 46, pp. 1284–1298, Jul 1992. [Online]. Available: https://link.aps.org/doi/10.1103/PhysRevB.46.1284

[39] A. Bakri, M. Z. Sahdan, F. Adriyanto, N. Raship, N. Said, S. Abdullah, and M. Rahim, "Effect of annealing temperature of titanium dioxide thin films on structural and electrical properties," vol. 1788, no. 1, p. 030030, 2017.

[40] D. Dambournet, I. Belharouak, and K. Amine, "Tailored preparation methods of tio2 anatase, rutile, brookite: Mechanism of formation and electrochemical properties," *Chemistry of Materials*, vol. 22, no. 3, pp. 1173–1179, 2010. [Online]. Available: https://doi.org/10.1021/cm902613h

[41] P. Spathis, E. Karagiannidou, and A.-E. Magoula-a3, "Influence of titanium dioxide pigments on the photodegradation of paraloid acrylic resin," *Studies in conservation*, vol. 48, no. 1, pp. 57–64, 2003.

[42] F. Feng, C. Li, J. Jian, X. Qiao, H. Wang, and L. Jia, "Boosting hematite photoelectrochemical water splitting by decoration of tio2 at the grain boundaries," *Chemical Engineering Journal*, vol. 368, pp. 959–967, 2019. [Online]. Available: https://www.sciencedirect.com/science/article/pii/S1385894719304644

[43] K. U. Wijayantha, S. Saremi-Yarahmadi, and L. M. Peter, "Kinetics of oxygen evolution at α-fe 2 o 3 photoanodes: a study by photoelectrochemical impedance spectroscopy," *Physical chemistry chemical physics*, vol. 13, no. 12, pp. 5264–5270, 2011.

[44] Y. Qiu, S.-F. Leung, Q. Zhang, B. Hua, Q. Lin, Z. Wei, K.-H. Tsui, Y. Zhang, S. Yang, and Z. Fan, "Efficient photoelectrochemical water splitting with ultrathin films of hematite on three-dimensional nanophotonic structures," *Nano Letters*, vol. 14, no. 4, pp. 2123–2129, 2014, pMID: 24601797. [Online]. Available: https://doi.org/10.1021/nl500359e

[45] J. A. Glasscock, P. R. F. Barnes, I. C. Plumb, and N. Savvides, "Enhancement of photoelectrochemical hydrogen production from hematite thin films by the introduction of ti and si," *The Journal of Physical Chemistry C*, vol. 111, no. 44, pp. 16 477–16 488, 2007. [Online]. Available: https://doi.org/10.1021/jp074556l

[46] O. Zandi, B. M. Klahr, and T. W. Hamann, "Highly photoactive ti-doped -fe2o3 thin film electrodes: resurrection of the dead layer," *Energy Environ. Sci.*, vol. 6, pp. 634–642, 2013. [Online]. Available: http://dx.doi.org/10.1039/C2EE23620F

[47] E. Fabbri, A. Habereder, K. Waltar, R. Kötz, and T. J. Schmidt, "Developments and perspectives of oxide-based catalysts for the oxygen evolution reaction," *Catalysis Science & Technology*, vol. 4, no. 11, pp. 3800–3821, 2014.

[48] S. Licht, B. Wang, S. Mukerji, T. Soga, M. Umeno, and H. Tributsch, "Over 18% solar energy conversion to generation of hydrogen fuel; theory and experiment for efficient solar water splitting," *International journal of hydrogen energy*, vol. 26, no. 7, pp. 653–659, 2001.

[49] Q. Mei, F. Zhang, N. Wang, Y. Yang, R. Wu, and W. Wang, "Tio 2/fe 2 o 3 heterostructures with enhanced photocatalytic reduction of cr (vi) under visible light irradiation," *RSC advances*, vol. 9, no. 39, pp. 22 764–22 771, 2019.

[50] L. Palmolahti, H. Ali-Löytty, R. Khan, J. Saari, N. V. Tkachenko, and M. Valden, "Modification of surface states of hematite-based photoanodes by submonolayer of tio2 for enhanced solar water splitting," *The Journal of Physical Chemistry C*, vol. 124, no. 24, pp. 13 094–13 101, 2020. [Online]. Available: https://doi.org/10.1021/acs.jpcc.0c00798

[51] J. Zhang and S. Eslava, "Understanding charge transfer, defects and surface states at hematite photoanodes," *Sustainable Energy & Fuels*, vol. 3, no. 6, pp. 1351–1364, 2019.

[52] M. G. Ahmed, I. E. Kretschmer, T. A. Kandiel, A. Y. Ahmed, F. A. Rashwan, and D. W. Bahnemann, "A facile surface passivation of hematite photoanodes with tio2 overlayers for efficient solar water splitting," *ACS applied materials & interfaces*, vol. 7, no. 43, pp. 24 053–24 062, 2015.

[53] T. H. Jeon, G.-h. Moon, H. Park, and W. Choi, "Ultra-efficient and durable photoelectrochemical water oxidation using elaborately designed hematite nanorod arrays," *Nano Energy*, vol. 39, pp. 211–218, 2017.

[54] X. Yang, R. Liu, C. Du, P. Dai, Z. Zheng, and D. Wang, "Improving hematite-based photoelectrochemical water splitting with ultrathin tio2 by atomic layer deposition," *ACS applied materials & interfaces*, vol. 6, no. 15, pp. 12 005–12 011, 2014.

[55] O. Zandi, A. R. Schon, H. Hajibabaei, and T. W. Hamann, "Enhanced charge separation and collection in high-performance electrodeposited hematite films," *Chemistry of Materials*, vol. 28, no. 3, pp. 765–771, 2016. [Online]. Available: https://doi.org/10.1021/acs.chemmater.5b03707

[56] C. Vichery, I. Maurin, P. Bonville, J.-P. Boilot, and T. Gacoin, "Influence of protected annealing on the magnetic properties of -fe2o3 nanoparticles," *The Journal of Physical Chemistry C*, vol. 116, no. 30, pp. 16 311–16 318, 2012. [Online]. Available: https://doi.org/10.1021/jp305069a

[57] T. J. LaTempa, X. Feng, M. Paulose, and C. A. Grimes, "Temperature-dependent growth of self-assembled hematite (α-fe2o3) nanotube arrays: rapid electrochemical synthesis and photoelectrochemical properties," *The Journal of Physical Chemistry C*, vol. 113, no. 36, pp. 16 293–16 298, 2009.

[58] A. Apolinario, C. Sousa, J. Ventura, J. Costa, D. Leitao, J. Moreira, J. Sousa, L. Andrade, A. Mendes, and J. Araujo, "The role of the ti surface roughness in the self-ordering of tio 2 nanotubes: a detailed study of the growth mechanism," *Journal of Materials Chemistry A*, vol. 2, no. 24, pp. 9067–9078, 2014.

[59] Arlete, "Nanostructured photoanodes for solar cells," Ph.D. dissertation, 2015.

[60] Solaronix. Tco22-7. [Online]. Available: https://shop.solaronix.com/electrode-materials/conductive-glass-substrates/tco22-8.html

[61] ——. Tco10-10. [Online]. Available: https://shop.solaronix.com/electrode-materials/conductive-glass-substrates/tco10-10.html

[62] Catarina, "Resistive switching in mgo and si/ag metal-insulator-metal structures," Ph.D. dissertation, 2019.

[63] C. Bundesmann and H. Neumann, "Tutorial: The systematics of ion beam sputtering for deposition of thin films with tailored properties," *Journal of Applied Physics*, vol. 124, no. 23, p. 231102, 2018.

[64] "What is ion beam deposition?" Dec 2019. [Online]. Available: https://www.dentonvacuum.com/what-is-ion-beam-deposition/

[65] A. Annamalai, P. S. Shinde, A. Subramanian, J. Y. Kim, J. H. Kim, S. H. Choi, J. S. Lee, and J. S. Jang, "Bifunctional tio 2 underlayer for α-fe 2 o 3 nanorod based photoelectrochemical cells: enhanced interface and ti 4+ doping," *Journal of Materials Chemistry A*, vol. 3, no. 9, pp. 5007–5013, 2015.

[66] Paula, "Environmentally friendly photoanodes for solar water splitting," Ph.D. dissertation, 2020.

[67] B. Inkson, "2 - scanning electron microscopy (sem) and transmission electron microscopy (tem) for materials characterization," in *Materials Characterization Using Nondestructive Evaluation (NDE) Methods*, G. Hübschen, I. Altpeter, R. Tschuncky, and H.-G. Herrmann, Eds. Woodhead Publishing, 2016, pp. 17–43. [Online]. Available: https://www.sciencedirect.com/science/article/pii/B978008100040300002X

[68] W. Zhou, R. Apkarian, Z. L. Wang, and D. Joy, "Fundamentals of scanning electron microscopy (sem)," in *Scanning microscopy for nanotechnology*. Springer, 2006, pp. 1–40.

[69] J. I. Goldstein, D. E. Newbury, J. R. Michael, N. W. Ritchie, J. H. J. Scott, and D. C. Joy, *Scanning electron microscopy and X-ray microanalysis*. Springer, 2017.

[70] A. Nanakoudis, "Sem signal - electron imaging," Jan 2021. [Online]. Available: https://www.thermofisher.com/blog/microscopy/sem-signal-types-electrons-and-the-information-they-provide/

[71] [Online]. Available: https://sites.ualberta.ca/~ccwj/teaching/microscopy/

[72] M. Abd Mutalib, M. Rahman, M. Othman, A. Ismail, and J. Jaafar, "Chapter 9 - scanning electron microscopy (sem) and energy-dispersive x-ray (edx) spectroscopy," in *Membrane Characterization*, N. Hilal, A. F. Ismail, T. Matsuura, and D. Oatley-Radcliffe, Eds. Elsevier, 2017, pp. 161–179. [Online]. Available: https://www.sciencedirect.com/science/article/pii/B9780444637765000097

[73] A. A. Bunaciu, E. G. UdriŞTioiu, and H. Y. Aboul-Enein, "X-ray diffraction: instrumentation and applications," *Critical reviews in analytical chemistry*, vol. 45, no. 4, pp. 289–299, 2015.

[74] "Bragg's law of diffraction." [Online]. Available: https://www.microscopy.ethz.ch/bragg.htm

[75] X. Shi, L. Cai, M. Ma, X. Zheng, and J. H. Park, "General characterization methods for photoelectrochemical cells for solar water splitting," *ChemSusChem*, vol. 8, no. 19, pp. 3192–3203, 2015.

[76] A. R. Zanatta, "Revisiting the optical bandgap of semiconductors and the proposal of a unified methodology to its determination," *Scientific Reports*, vol. 9, no. 1, p. 11225, Aug 2019. [Online]. Available: https://doi.org/10.1038/s41598-019-47670-y

[77] T. Lopes, L. Andrade, F. Le Formal, M. Gratzel, K. Sivula, and A. Mendes, "Hematite photoelectrodes for water splitting: evaluation of the role of film thickness by impedance spectroscopy," *Phys. Chem. Chem. Phys.*, vol. 16, pp. 16 515–16 523, 2014. [Online]. Available: http://dx.doi.org/10.1039/C3CP55473B

[78] L. A. Marusak, R. Messier, and W. B. White, "Optical absorption spectrum of hematite, αfe2o3 near ir to uv," *Journal of Physics and Chemistry of Solids*, vol. 41, no. 9, pp. 981–984, 1980.

[79] N. T. Hahn and C. B. Mullins, "Photoelectrochemical performance of nanostructured ti- and sn-doped -fe2o3 photoanodes," *Chemistry of Materials*, vol. 22, no. 23, pp. 6474–6482, 2010. [Online]. Available: https://doi.org/10.1021/cm1026078

[80] H. Tang, W.-J. Yin, M. Matin, H. Wang, T. Deutsch, M. M. Al-Jassim, J. A. Turner, and Y. Yan, "Titanium and magnesium co-alloyed hematite thin films for photoelectrochemical water splitting," *Journal of Applied Physics*, vol. 111, no. 7, p. 073502, 2012.

[81] Y. Ling, G. Wang, D. A. Wheeler, J. Z. Zhang, and Y. Li, "Sn-doped hematite nanostructures for photoelectrochemical water splitting," *Nano Letters*, vol. 11, no. 5, pp. 2119–2125, 2011, pMID: 21476581. [Online]. Available: https://doi.org/10.1021/nl200708y

[82] P. S. Shinde, S. H. Choi, Y. Kim, J. Ryu, and J. S. Jang, "Onset potential behavior in α-fe 2 o 3 photoanodes: the influence of surface and diffusion sn doping on the surface states," *Physical Chemistry Chemical Physics*, vol. 18, no. 4, pp. 2495–2509, 2016.

[83] J. S. Jang, J. Lee, H. Ye, F.-R. F. Fan, and A. J. Bard, "Rapid screening of effective dopants for fe2o3 photocatalysts with scanning electrochemical microscopy and investigation of their photoelectrochemical properties," *The Journal of Physical Chemistry C*, vol. 113, no. 16, pp. 6719–6724, 2009.

[84] A. Annamalai, H. H. Lee, S. H. Choi, S. Y. Lee, E. Gracia-Espino, A. Subramanian, J. Park, K.-j. Kong, and J. S. Jang, "Sn/be sequentially co-doped hematite photoanodes for enhanced photoelectrochemical water oxidation: effect of be 2+ as co-dopant," *Scientific reports*, vol. 6, no. 1, pp. 1–11, 2016.

[85] R. Morrish, M. Rahman, J. MacElroy, and C. A. Wolden, "Activation of hematite nanorod arrays for photoelectrochemical water splitting," *ChemSusChem*, vol. 4, no. 4, pp. 474–479, 2011.

[86] X. Fu, Y. Liu, X. Cao, J. Jin, Q. Liu, and J. Zhang, "Feco–nx embedded graphene as high performance catalysts for oxygen reduction reaction," *Applied Catalysis B: Environmental*, vol. 130, pp. 143–151, 2013.

[87] Q. Wu, T. Li, W. Wang, and Y. Xiao, "High-throughput chainmail catalyst feco@ c nanoparticle for oxygen evolution reaction," *International Journal of Hydrogen Energy*, vol. 45, no. 51, pp. 26 574–26 582, 2020.

[88] C. Sun, H. Wang, S. Ji, X. Wang, V. Linkov, X. Tian, L. Yao, J. Zhao, and R. Wang, "Layer-structured feco bihydroxide as an ultra-stable bifunctional electrocatalyst for water splitting at high current densities," *Sustainable Energy & Fuels*, vol. 5, no. 10, pp. 2747–2752, 2021.

[89] J. Tauc, R. Grigorovici, and A. Vancu, "Optical properties and electronic structure of amorphous germanium," *physica status solidi (b)*, vol. 15, no. 2, pp. 627–637, 1966.